7-30-2017

Piezoelectric Structures with Circuitry Integration for Wave Guiding and Energy Manipulation

Jiawen Xu
University of Connecticut - Storrs, jia.xu@uconn.edu

Piezoelectric Structures with Circuitry Integration for Wave Guiding and Energy Manipulation

Jiawen Xu, Ph.D.

University of Connecticut, Storrs, CT

The objective of this dissertation research is on the designing and optimization of promising wave guiding and energy manipulation approach. Specifically address above-mentioned issues of modeling and application of piezoelectric metamaterials and energy harvesting. The first research task is to develop fundamental modeling and understanding of piezoelectric metamaterial integrated with LC shunts to create local resonances. We establish the lumped-parameter model. Taking advantage of the model, we identify the influence of a key parameter to the behavior of the metamaterial. The second research task is to explore the application of the piezoelectric metamaterials in acoustic wave guiding. This work is based on the significant acoustic wave velocity shifting in the vicinity of the bandgap. Such shifting leads to a beam steering effect in the host medium. The third research task is to apply the piezoelectric metamaterials into tailoring vibration modes. The combination of resonance and antiresonance can create unusual vibration mode in a finite metamaterial beam. The fourth research task is to enhance the energy harvesting efficiency. By reducing the equivalent stiffness of a piezoelectric transducer, we reduce the portion of elastic energy stored in the mechanical part of the system and therefore, enhance the power output efficiency. The fifth research task is to realize single cantilever based multi-directional energy harvesting. We replace the proof-mass used in simple cantilever by a pendulum. Take advantage of 1:2 internal resonance, the system is capable of transferring the input mechanical energy in different directions to the beam bending motion with high efficiency.

Piezoelectric Structures with Circuitry Integration for Wave Guiding and Energy Manipulation

Jiawen Xu

B.S., University of Science and Technology of China, 2009

M.S., University of Science and Technology of China, 2011

A Dissertation

Submitted in Partial Fulfilment of the

Requirements for the Degree of

Doctor of Philosophy

at the

University of Connecticut

2017

APPROVAL PAGE

Doctor of Philosophy Dissertation

Piezoelectric Structures with Circuitry Integration for Wave Guiding and Energy Manipulation

Presented by

Jiawen Xu

Major Advisor _____

Dr. Jiong Tang

Associate Advisor _____

Dr. Nejat Olgac

Associate Advisor _____

Dr. George Lykotrafitis

Associate Advisor _____

Dr. Xu Chen

Associate Advisor _____

Dr. Ying Li

University of Connecticut

2017

This work is dedicated to my beloved wife

and parents for the infinite love.

ACKNOWLEDGEMENT

First and foremost, I would like to express my sincere gratitude and respect to my major academic advisor Professor Jiong Tang. I appreciate his guidance, patience, encouragement, and support for my graduate career. Under the advisement of Professor Tang for almost 6 years, I have learned a lot of useful things that not only benefit my academic research, but also positively affect my attitude towards the challenges and barriers in real life. This is a most rewarding experience, which I will cherish and preserve in my mind.

I also would like to express my gratitude to my associated academic advisors, Professor Nejat Olgac, Professor George Lykotrafitis, Professor Xu Chen, Professor Ying Li, for their precious time serving on my committee. Their keen insight, helpful advice and critiques on my research project give a tremendous value to me throughout my entire graduate study.

I thank the following former and current labmates in the Structure and System Dynamic Research Laboratory, for their support during the time we were together – Kai Zhou, Ji Zhao, Arun Hedge, Jiawen Xu, Pei Cao, Shengli Zhang, David Yoo, Shilong Li, and Yuan Yuan. Also thanks to all my other friends in UConn. The friendship between us will be highly valued.

I would express my greatest gratitude to my parents for their unconditional love and constant support. Finally, I gratefully acknowledge the financial support provided by National Science Foundation.

Table of Contents

Chapter 1 Introduction and Research Overview

1.1 Background and State-of-the-Art review

1.1.1 Introduction to piezoelectric materials and applications

The piezoelectricity is a phenomenon of electric charge accumulation in certain type of non-conductive solid materials in case of mechanical stress/strain applied. The piezoelectric effect was firstly discovered by Jacques and Pierre in 1880. It was noticed that crystals (e.g., quartz, tourmaline, topaz, cane sugar, and Rochelle salt) would generate electric charges when force was applied in certain directions. In their following research, the two-way electro-mechanical coupling was confirmed in piezoelectric materials that applying electric field would also cause deformation of this type of material (Safari and Akdogan, 2008). The piezoelectric effect is induced by the occurrence of electric dipole moments in solids. When applying a mechanical stress, polarization would be changed. The caution of piezoelectric effects might be a re-configuration of the dipole-inducing surrounding or re-orientation of molecular dipole moments under the influence of external stress/strain, as shown in Figure 1-1.

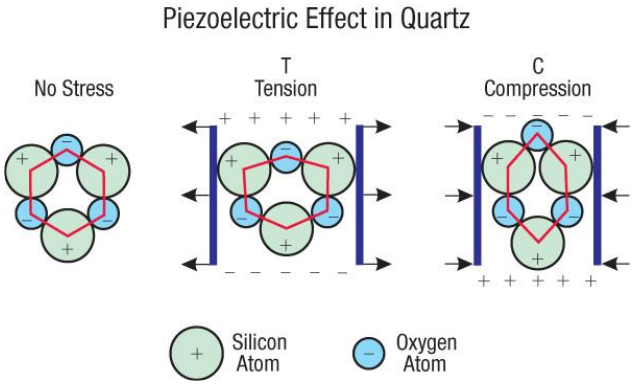

Figure 1-1. Demonstration of piezoelectric effect.

In the nature world, there are several minerals exhibit piezoelectric effects. For example, Quartz, Berlinite ($AlPO_4$), Lead titanate ($PbTiO_3$), Collagen (main structural protein), tendon (is type of tissue that usually connects muscle to bone), wood, DNA, enamel (type of tissue covers the tooth), dentin (Di Lullo, et al., 2002). On the other hand, many artificial crystals, ceramics, polymers are fabricated for

piezoelectric behavior. Examples include Gallium orthophosphate ($GaPO_4$) Langasite ($La_3Ga_5SiO1_4$) crystals, Barium Titanate ($BaTiO_3$), Lead Zirconate Titanate (Pb[ZrxTi1-x]O_3 $0 \leq x \leq 1$), Potassium Niobate ($KNbO_3$), Lithium Niobate ($LiNbO_3$), Lithium Tantalate ($LiTaO_3$), Sodium tungstate (Na_2WO_3), Zinc Oxide (ZnO) piezoelectric ceramics, polymers are polyvinylidene Fluoride (PVDF) and its copolymers such as, P(VDF- trifluoroethylene), P(VDF- tetrafluoroethylene), and terpolymers such as, P(VDF-TrFE- CTFE) and P(VDF-TrFE-CFE).

Note that piezoelectric materials are normally non-conducting. Additionally, charge displacement is induced due to stress/strain applied within the piezoelectric material. In applications, electrodes are covering the surfaces of the piezoelectric transducer. The variation of surface charge density in the electrodes indicates the change of electrical field within the piezoelectric materials. For instance, voltage about 6.25 kV can be produced when a force of 1 kN is applied to a 1 centimeter cube of quartz (Vedaraj et al., 2012). In recent decades, attentions are paid on piezoelectric devices in industrial and manufacturing since piezoelectric materials are excellent candidate for sensors or actuators due to their simple structure and high-power density. Among the various types of piezoelectric materials, piezoceramics is the largest material group for piezoelectric devices. In the meantime, piezopolymer demonstrates fastest growth due to its light weight and small size.

Piezoelectric materials have been applied in various situations. Electric cigarette lighter, for example, is one application of piezoelectric for high voltage generation. The piezo can also be found in sensors and actuators. Piezoelectric materials are adopted widely in sensors such as, generation and detection of acoustic wave, medical treatment and chemical and biological sensor with high sensitivity. Other applications as sensors include penetrometer instrument on Huygens probe, dynamic strain gauges, switches, speakers, contact microphones, etc.

Due to the two-way electro-mechanical coupling, i.e., transfer energy between mechanical and electrical domain, applications of piezoelectric materials can be found in actuator designing. Piezo are utilized as actuators due their deformation under electrical field. For example, piezoelectric stacks would

have longitude extension when voltage is applied; bending would be induced in a piezoelectric composite cantilever when driven by electrical energy. These characteristics enable the applications of piezo in aspects of loudspeakers, piezoelectric motors, atomic force microscopy (AFM), inject printers, X-ray shutters, and piezoelectric fuel injection in diesel engine.

1.1.2 Piezoelectric material based acoustic metamaterial

Metamaterial, defined as artificial structures that exhibit physical properties not available in natural material, has extraordinary capability in low-frequency sound/vibration attenuation, negative refraction, and super lenses (Liu et al, 2000; Landy et al, 2008; Pendry and Li, 2008; Yang et al, 2010; Bigoni et al, 2013; Baravelli and Ruzzene, 2013; Yoo et al, 2014; Zhu et al, 2016). Representative example of metamaterials can be found in Figure 1-2.

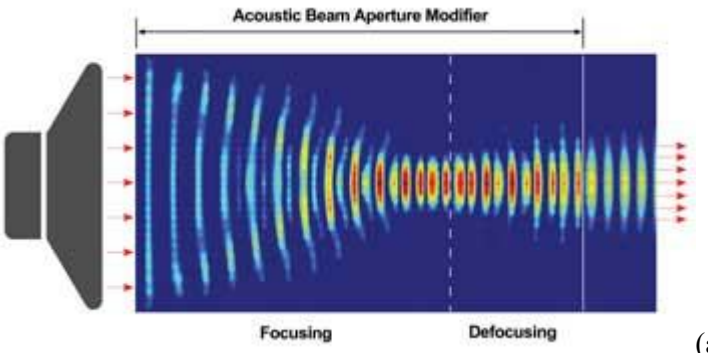

(a)

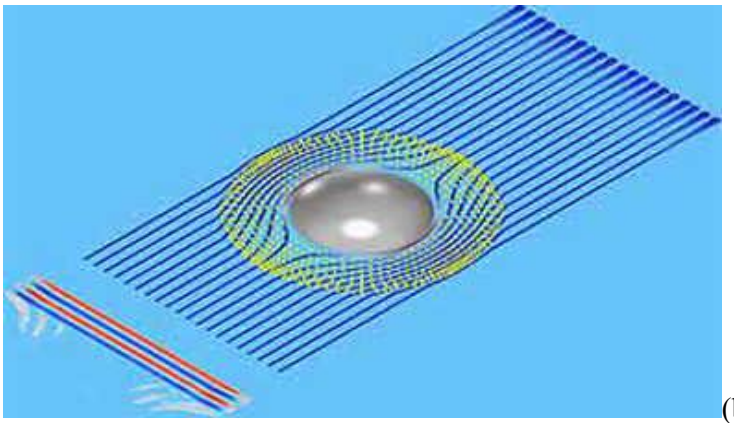
(b)

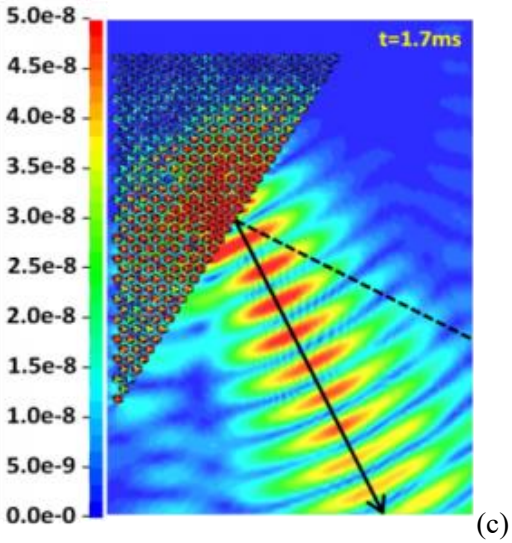

Figure 1-2. Example of acoustic metamaterials. (a) Acoustic wave focusing; (b) Cloaking; (c) Negative refraction.

The acoustic metamaterial, consisting of periodically arranged local microstructures or unit-cells integrated to a host medium, is capable of manipulating elastic wave propagation. Typical acoustic metamaterial utilizes Bragg scattering or local resonance (Li and Chan, 2004; Fang et al, 2005; Yang et al, 2008; Mei et al, 2012; Zhao et al, 2014; Che et al, 2017). Bragg bandgaps stand for the zones between incident and reflected waves, which are generated at wavelengths comparable to the spatial scale of a unit-cell within the periodic lattice (Monsoriu et al, 2006; Achaoui et al, 2011; Liu and Hussein, 2012). Different from the Bragg scattering mechanism, the local resonance mechanism utilizes the sub-wavelength local resonances induced within a unit-cell. The local resonance can alter the frequency-dependent effective mass densities and/or bulk moduli of the continuum media. In most cases, the internal resonators have highly contrasting elastic properties. Within the bandgap, the elastic wave cannot propagate, and wave energy is reflected back or temporarily stored in resonators (Liu et al, 2000; Huang and Sun, 2010; Tan et al, 2014).

Because of their two-way electro-mechanical coupling, piezoelectric transducers have been adopted

to enhance bandgap behavior in metamaterial (Thorp et al, 2005; Airoldi and Ruzzene, 2011; Zhou et al, 2015; Wang and Chen, 2016).

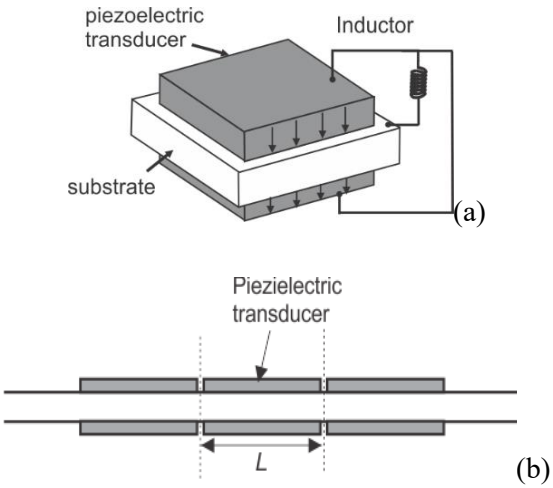

Figure 1-3. Piezoelectric metamaterials. (a) Unit-cell; (b) Piezoelectric metamaterial beam.

Many studies employ a negative capacitance element integrated to piezoelectric transducer to reduce the equivalent local stiffness of a unit-cell, thereby tuning the location of bandgap or influencing its bandwidth (Chen et al, 2014; Zhu et al, 2016). Alternatively, piezoelectric metamaterial with periodic resonant circuits can produce directly the local resonance bandgap. Typically, a piezoelectric metamaterial has periodically arranged piezoelectric transducers (in unimorph or bimorph manner). An inductive load is connected to piezoelectric transducers, and a local resonance is created by the LC (inductor-capacitor) circuit as the piezoelectric transducer acts electrically as a capacitor, as shown in Figure 1-3. The shunt circuits create bandgap in the vicinity of the LC resonance. For example, piezoelectric periodic arrays are integrated into rod for wave attenuation and localization (Thorp et al, 2005). For another example, multi-resonant shunts are adopted to generate multiple bandgaps in a piezoelectric metamaterial (Airoldi and Ruzzene, 2011). Theoretical and experimental investigations on photonic rods and beams (Wang et al, 2011) with shunt circuits have been performed. Notably, piezoelectric metamaterial has advantages over the more conventional mechanical metamaterial (which

utilizes only the mechanical displacement/deformation) in two aspects: relatively simple configuration, and adaptivity. Piezoelectric transducers are usually attached to the host structure directly, and even simple topology/geometry can yield complex dynamic phenomena locally at the unit-cell level and globally at the metamaterial level. Moreover, the shunted piezoelectric transducers allow the online tuning of bandgap towards a desired frequency range, as one can conveniently integrate tunable circuitry elements.

1.1.3 Piezoelectric structure based energy conversion

In recent years, prolonging the power supply of portable and wireless apparatuses by harvesting ambient energy has received significant attention (Paradiso and Starner, 2005; Roundy et al, 2005; Mitcheson et al, 2008). Since vibration energy is virtually ubiquitous, utilizing piezoelectric devices to convert the vibration energy into electrical energy has emerged as one of the primary methods (Anton and Sodano, 2007; Priya, 2007; Khaligh et al, 2010). Piezoelectric transducers, possessing two-way electro-mechanical coupling, feature advantages of being compact, having high bandwidth and maintaining good linearity within its functional range.

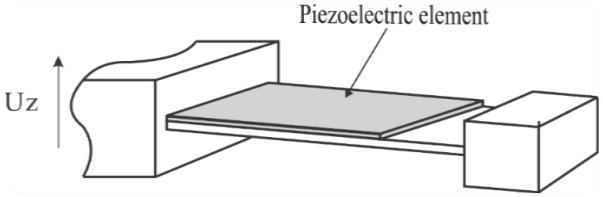

Figure 1-4. Piezoelectric cantilever for vibration energy harvesting.

A typical piezoelectric energy harvester consists of a cantilever beam with a piezoelectric transducer bonded near its root and a proof-mass attached to its tip (Anton and Sodano, 2007; Priya, 2007; Khaligh et al, 2010; Ji et al, 2010; Xu et al, 2012). The proof-mass is adopted to tune the natural frequency of the beam and to enhance the vibration energy absorbing.

Design and optimization of piezoelectric transducer-based energy harvesters have been addressed in several aspects (Liang and Liao, 2011): 1) absorbing mechanical energy from vibration source (Shenck and Paradiso, 2001; Shahruz, 2006; Ji et al, 2010); 2) converting mechanical energy into electrical energy (Baker et al, 2005; Xu et al, 2012); and 3) storing electrical energy (Guyomar et al, 2005). Amongst these aspects, the conversion of mechanical energy into electrical energy is generally characterized by the electro-mechanical coupling coefficient of the device, i.e., the ratio of the energy converted to that imposed (Tang and Wang, 2001; Shu and Lien, 2006; Tang and Yang, 2011).

The effect of electro-mechanical coupling on energy harvesting has been analyzed in a number of studies. Roundy et al (2005) suggested that the power generated by a piezoelectric harvester was in general proportional to the electro-mechanical coupling. Lefeuvre et al (2006) indicated that the power output at resonance was proportional to the coupling in low coupling condition. Shu and Lien (2006) modeled and analyzed the power output of a piezoelectric energy harvesting system, and concluded that better performance could be achieved with larger coupling and quality factor. Meanwhile, Kim et al (2012) derived an optimal value for maximum power when the coupling coefficient was greater than a certain threshold value. While saturation of power output may exist (Renno et al, 2009), the maximum power output envelop could be increased with the increase of electro-mechanical coupling (Guyomar et al, 2005; Shu and Lien, 2006). Tang and Yang (2011) further pointed out that a large coupling coefficient boosts power output of a system with standard circuit even more than that with synchronized charge extraction technique (SCE). The electro-mechanical coupling coefficient is directly related to the transducer material property, predominantly the piezoelectric coupling constant at the material-level. For example, one of the most commonly used piezoelectric transducers, PZT5H, has limited piezoelectric coupling constant of 0.44 in the 31 direction and 0.75 in the 33 direction, respectively (when attached to a beam, the 1 coordinate of the transducer is along the length direction, the 2 coordinate the width direction and the 3 coordinate the transversal direction) (IEEE Standard). Choosing transducers with larger piezoelectric coupling constant may certainly help. Rakbamrung et al (2010) compared the performance

of two energy harvesters with the same configuration but two different transducers, PMN-PT and PZT. The one with PMN-PT showed higher power output, but this type of material is more expensive.

At the device-level, a number of studies have defined an electro-mechanical coupling coefficient of an energy harvester, and indicated that this coefficient is related to not only the material property of the transducer, but also the specific design features of the harvester. For example, the harvester in general stores a significant portion of energy through its mechanical stiffness throughout the energy harvesting process, which reduces the energy conversion efficiency (Roundy, 2005; Kenji and Takaaki, 2010; Liang and Liao, 2011). It is worth emphasizing that the mechanical stiffness of the energy harvester includes contributions from both the host beam and the piezoelectric transducer. A significant portion of the mechanical stiffness in the harvester comes from the piezoelectric bending stiffness, which cannot be easily reduced. In the unimorph case, a host beam is required, which shifts the beam-shaped transducer's neutral line so the charges generated by the top and bottom halves of the transducer during bending vibration will not offset. The host beam thus has to possess certain thickness, yielding considerable mechanical stiffness. Many investigations have been carried out to explore manipulating the mechanical behavior as well as the circuitry dynamics of the harvester in order to enhance the electro-mechanical coupling. Chen and Wang (2005) investigated the increase of the electro-mechanical coupling of a piezoelectric cantilever by thickness ratio optimization, and identified a maximum coupling under a proper thickness ratio. Alberto and Paolo (2007) studied the optimal positioning of piezoelectric transducer. These investigations are in the category of mechanical tailoring, and therefore are subject to the limitation of the material-level coupling constant.

It is worth noting that there actually has been a stream of efforts to improve the electro-mechanical coupling coefficient and to tune the system dynamics in a device by resorting to external elements. For example, Tang and Wang (2001) indicated that adding an operational amplifier-based negative capacitance, which offsets the inherent capacitance of the piezoelectric transducer, could increase the electro-mechanical coupling. Since the negative capacitance element itself consumes power, such an

approach is more suitable for control/damping applications. For another example, it was found that compressive axial forces could reduce the mechanical bending stiffness of the cantilever (Lesieutre and Davis, 1997; Leland and Wright, 2006; Masana and Daqaq, 2011; Niri and Salamone, 2012). This type of methods is generally effective when the vibration amplitudes are small. To introduce favorable dynamic effects to energy harvesters, conservative forces due to permanent magnets, because of the non-contact nature, recently emerged as an attractive option. Challa et al (2008) attached magnetic blocks on the top and bottom of the cantilever, and created attractive and repulsive forces to adjust the harvester's resonant frequency to match the frequency of the ambient vibration to improve the bandwidth of energy harvesting. As the force by the magnetic blocks exhibits nonlinearity, the system is essentially nonlinear. Cottone et al (2009) placed magnets on the cantilever tip and in the vicinity to generate nonlinearity which was then used to improve the bandwidth of energy harvesting. One challenge in these nonlinear methods is that the system behavior is usually amplitude-dependent, which may limit the effectiveness of the respective methods to a certain operating range.

Additionally, the piezoelectric cantilever system behaves optimally when its natural frequency matches the frequency of the excitation and the response direction is aligned with that of the excitation. In reality, however, ambient excitations have components in multiple directions, and may feature broad frequency bandwidth. For example, a device carried by a pedestrian is subject to accelerations in all three directions exhibiting aperiodic dynamics (Xu and Tang, 2015a). The power output of the traditional harvesters decreases significantly, if the excitation comes from directions other than the response direction or is off-resonance (Cottone et al, 2009; Shahruz, 2006; Ando et al, 2013; Su and Zu, 2013; Xu and Tang, 2015a).

There has been a stream of efforts to address the bandwidth limitation of simple harvesters. Typically, multi-resonances by a single harvester and nonlinearity induced by permanent magnet or internal resonance are adopted (Cottone et al, 2009; Shahruz, 2006; Wu et al, 2006; Tadesse et al, 2009; Erturk et al, 2009a; Erturk et al, 2009b; Vinod et al, 2008; Stanton et al, 2009; Jung and Yun, 2010; Zhou

et al, 2013; Chen and Jiang, 2015). On the other hand, there are much less investigations that cope with multi-directional excitations. Bartsch et al (2009) connected a disk shape mass to concentric circular springs, where the device can harvest vibration energy through electromagnetic conversion by utilizing the multi-dimensional motion of the mass. Yang et al (2013) studied a 2-dimensional vibration energy harvester based on the magnetostrictive transactions in a circular cross-section rod which can bend in different directions to generate power. For piezoelectric energy harvesting, existing studies are oftentimes based on multiple cantilevers. Ando et al (2013) reported a 2-dimensional piezoelectric energy harvester, in which two separate piezoelectric cantilevers are placed in different directions and coupled with magnetic interaction. Su and Zu (2013) further explored a tri-directional energy harvesting scheme. A discrete spring-mass oscillator is added and couples the two beams under the magnetic effect. In a more recent study (Chen et al, 2015), a dandelion-like generator was designed with many cantilevers assembled in different directions, where the cantilevers are sensitive in many directions and therefore this device can achieve multi-directional energy harvesting. Yang et al (2015) proposed a frame configured energy harvester which has vertical and horizontal vibration modes around one frequency point and is feasible for two-dimensional vibration energy harvesting.

1.2 Problem Statement

1.2.1 Piezoelectric structure based acoustic metamaterial

So far, almost all the studies on shunted piezoelectric metamaterial are based on the transfer-matrix method or finite element analysis (Casadei et al, 2010; Wang and Chen, 2016). Previous investigations concerning piezoelectric shunt design and analysis in sensing/control applications, however, often resort to the lumped-parameter approach, which can particularly help revealing the underlying physics with the complicated parametric influences (Tang and Wang, 2003; Wang and Tang, 2008; Zhao et al, 2011). It is worth noting that the circuitry dynamics in electrical domain is described naturally by lumped-parameter model. The lumped-parameter approach is suitable to dealing with complex circuitry integration schemes

as well as systems with nonlinearity. Indeed, wave propagation in one-dimensional nonlinear periodic structure has been investigated by adopting lumped-parameter analysis, and amplitude-dependent behaviors with tunable dispersion curves and cutoff frequencies are analyzed (Narisetti et al, 2010). Similar analysis has also been conducted for metamaterial with complex circuits (Hu et al, 2016). It is worth noting that in these studies, while lumped-parameter analyses are performed, the lumped parameters are obtained in an ad hoc manner as they directly start from a discrete model of the mechanical structure. A more common approach is to conduct continuum mechanics based modeling of the host substrate followed by discretization with respect to wavenumber, where an equivalent frequency-dependent Young's modulus is used to reflect the piezoelectric shunt circuit effect (Casadei et al, 2010; Wang and Chen, 2016). In this type of approach, the shunt circuit effect is included as equivalent impedance added to the original mechanical impedance of the transducer. A limitation of this approach is that it may not be able to deal with complex circuitry especially those with multiple branches or nonlinear elements.

Additionally, the previously works on piezoelectric metamaterials are mostly focus on the bandgap behavior and acoustic wave attenuation. Fundamentally, the bandgaps are induced based upon the fact that no corresponding acoustic wave number existing in certain frequency range. Specifically, the local resonance of the LC shunt circuit reduces the wave velocity versus frequency to zero. It's should be emphasizing that the reduction of wave velocity is carried out gradually. Moreover, the reduction of the acoustic wave occurs in the vicinity of the bandgap dramatically, i.e., in a very small frequency range. While the bandgap behavior has received lots of attentions, little discussion was carried out in aspects of the acoustic velocity change of the piezoelectric metamaterial. In this regard, we proposed that the significant velocity change near the bandgap. This phenomenon can be adopted for acoustic wave guiding.

Thirdly, negative material properties and bandgap characteristics are intensively discussed on local resonance acoustic metamaterials. Negative Young's modulus is investigated in piezoelectric

metamaterial with local LC resonance. The negative effective mass/Young's modulus can generate a bandgap which yield acoustic wave attenuation. Note that ideal periodicity cannot be easily achieved in experiments, serially connected unit-cells are adopted to investigate the bandgap behavior. The bandgap/wave attenuation characteristics is accompanied due to the bandgap behavior at anti-resonance. Specifically, anti-resonance is a pronounced minimum in the amplitude of the host structure within the bandgap. On the other hand, resonances of the finite Phononic crystal are usually ignored since they yield large amplitude motion of the host structure. In other words, the resonances yield multiple peaks in the transmission diagram of the metamaterial system. We propose that, the resonance and anti-resonance behavior of a finite metamaterial beam can be adopted for vibration mode tailoring. Specifically, unusual vibration modes can be created with the capability "hit the enemy through another man in between".

1.2.2 Piezoelectric structure based energy conversion

To enhance the electromechanical coupling coefficient, one ideal solution would be to add a negative spring element to a harvester to reduce its bending stiffness while maintaining the linearity. As mentioned, reducing the mechanical stiffness can increase the electro-mechanical coupling at the system level, and maintaining linearity can ensure that the performance enhancement can be realized within the entire operating range. Such a negative spring element should be non-contact with no additional damping. Inspired by the recent explorations in incorporating magnets into energy harvester design (Challa et al, 2008; Cottone et al, 2009), in this research we develop a design scheme that enables the compensation of the effective stiffness of the energy harvester by utilizing magnetic effects. In particular, a linear magnetic field effect is synthesized by placing properly configured magnetic elements in the vicinity of the piezoelectric cantilever. The magnetic field produced by these elements yields a linear force with respect to the cantilever displacement that is equivalent to the negative spring element effect, thereby reducing the portion of energy stored in transducer and host structure and improving the electro-mechanical coupling of the system. As the additional force induced is linear, the electro-mechanical

coupling improvement is effective throughout the entire operating range of the harvester, and is not amplitude-dependent. Another potential advantage of this design scheme is that adding the aforementioned magnetic elements does not exclude the usage of other design optimization methods proposed previously (Shenck and Paradiso 2001; Baker et al, 2005; Guyomar et al, 2005; Shahruz, 2006; Challa et al, 2008; Cottone et al, 2009; Xu et al, 2012).

Secondly, traditional vibration energy harvesters are sensitive in only one direction. In reality, ambient excitations have components in multiple directions, and may feature broad frequency bandwidth. For example, a device carried by a pedestrian is subject to accelerations in all three directions exhibiting aperiodic dynamics (Xu and Tang, 2015). The power output of the traditional harvesters decreases significantly, if the excitation comes from directions other than the response direction or is off-resonance (Cottone et al, 2009; Shahruz, 2006; Ando et al, 2013; Su and Zu, 2013; Xu and Tang, 2015a). Ideally, a multi-directional energy harvester with a single piezoelectric cantilever may have advantages of being compact and low-cost. The challenges for achieving such a design are presented as follows. One challenge is to induce beam bending motion based on excitations from all three directions. The most commonly used mode of the cantilever, the first bending mode, is sensitive to excitation along the bending direction only. Another challenge is to induce a primary resonance of beam bending motion under multi-directional excitations. As the device is designed for vibration energy harvesting, primary resonance of beam bending motion is needed to boost the efficiency. The power output is limited when the harvester is working off-resonance or at sub-resonance.

1.2.3 Research Objective and Approach overview

The objective of this dissertation research is on the designing and optimization of promising wave guiding and energy manipulation approach. Specifically address above-mentioned issues of modeling and application of piezoelectric metamaterials and energy harvesting. To fulfill the objective, this research is separated into four major sections.

The first research task is to develop fundamental modeling and understanding of piezoelectric metamaterial integrated with LC shunts to create local resonances. We establish the lumped-parameter model of the piezoelectric metamaterial, which is built upon the continuum mechanics characterization of the host substrate and piezoelectric transducer at the unit-cell level. Transverse wave is considered throughout the modeling and analysis, and the lumped parameters are derived based on the wavenumber involved. Taking advantage of the model, we identify the influence of a key parameter, the system-level electro-mechanical coupling coefficient of the piezoelectric transducer in a unit-cell, to the behavior of the metamaterial. It is found that the bandwidth of the bandgap increases with the electro-mechanical coupling coefficient. We further compare and analyze the characteristics of the unit-cell integrated with piezoelectric transducers connected in parallel and in series, respectively, aiming at assessing circuitry configuration effect.

The second research task is to explore the application of the piezoelectric metamaterials in acoustic wave guiding. This work is based on the significant acoustic wave velocity shifting in the vicinity of the bandgap. Indeed, there have been recent studies utilizing piezoelectric metamaterial integrated with shunt circuits for wave attenuation and localization. It is well-known in optics that natural light can be dispersed through a prism as wave components with different speeds (under different frequencies) in the light yield different refraction angles when passing through the prism. This gives rise to our fundamental idea of tunable beam steering, i.e., to utilize the acoustic wave velocity shifting in the vicinity of local resonant frequency of the LC shunt in piezoelectric metamaterial, where the tunability is realized by inductance tuning. Our hypothesis is that such shifting of the velocity of acoustic wave, combined with the prism-like triangle-arrangement of unit-cells, will lead to a beam steering effect in the host medium. This metamaterial synthesis is achieved by attaching/bonding arrayed piezoelectric transducers, which are connected with tunable inductors individually, to a structural medium whereas the structure remains unchanged.

The third research task is to apply the piezoelectric metamaterials into tailoring vibration modes of

finite metamaterial beam. In the local resonance based metamaterial, the bandgap behavior is directly associating with the antiresonance of the local resonator. In the physics of coupled oscillators, antiresonance, by analogy with resonance, is a pronounced minimum in the amplitude of one oscillator at a particular frequency, accompanied by a large shift in its oscillation phase. In the local resonance metamaterial, antiresonance indicates the minimum in the amplitude of the host structure. This phenomenon then yields the reduction of the amplitude of the acoustic wave in the host structure, i.e., wave attenuation. On the other hand, antiresonance is always be coupled with resonance. The resonance behavior indicates maximum amplitude of the oscillating. Here we propose that the combination of resonance and antiresonance can create unusual vibration mode in a finite metamaterial beam.

The fourth research task is to enhance the energy harvesting efficiency. Specifically, most of the mechanical energy is stored in the elastic part of the cantilever. The elastic strain energy is stored in both piezoelectric transducer and the host structure. Our intention here is that by reducing the equivalent stiffness of a piezoelectric transducer, we may reduce the portion of elastic energy stored in the mechanical part of the system and therefore, enhance the power output efficiency.

The fifth research task is to realize single cantilever based multi-directional energy harvesting. The challenges for achieving such a design are presented as follows. One challenge is to induce beam bending motion based on excitations from all three directions. The most commonly used mode of the cantilever, the first bending mode, is sensitive to excitation along the bending direction only. Note that a single mass can have motion in 3-dimensional space and act as a dynamic amplifier (Aldraihem and Baz, 2011; Zhou et al, 2012; Tang and Yang, 2012). In this paper, we propose to replace the proof-mass used in simple cantilever by a pendulum. Our intention is to take advantage of the nonlinear coupling between the pendulum motion in multiple directions and the beam bending vibration (Xu and Tang, 2015b). Another challenge is to induce a primary resonance of beam bending motion under multi-directional excitations. As the device is designed for vibration energy harvesting, primary resonance of beam bending motion is needed to boost the efficiency. The power output is limited when the harvester is working off-resonance

or at sub-resonance. Our hypothesis here is that, by choosing proper parametric combination in the aforementioned piezoelectric cantilever-pendulum, we can induce internal resonance. Such internal resonance facilitates energy interchange between the primary resonance of beam vibration and the pendulum motion. In other words, the system is capable of transferring the input mechanical energy in different directions to the beam bending motion with high efficiency.

Chapter 2 Analysis of Piezoelectric Metamaterial with Circuitry Integration

2.1 Introduction

Metamaterial, defined as artificial structures that exhibit physical properties not available in natural material, has extraordinary capability in low-frequency sound/vibration attenuation, negative refraction, and super lenses (Liu et al, 2000; Landy et al, 2008; Pendry and Li, 2008; Yang et al, 2010; Bigoni et al, 2013; Baravelli and Ruzzene, 2013; Yoo et al, 2014; Zhu et al, 2016). The acoustic metamaterial, consisting of periodically arranged local microstructures or unit-cells integrated to a host medium, is capable of manipulating elastic wave propagation. Typical acoustic metamaterial utilizes Bragg scattering or local resonance (Li and Chan, 2004; Fang et al, 2005; Yang et al, 2008; Mei et al, 2012; An et al, 2015; Che et al, 2017). Bragg bandgaps stand for the zones between incident and reflected waves, which are generated at wavelengths comparable to the spatial scale of a unit-cell within the periodic lattice (Monsoriu et al, 2006; Achaoui et al, 2011; Liu and Hussein, 2012). Different from the Bragg scattering mechanism, the local resonance mechanism utilizes the sub-wavelength local resonances induced within a unit-cell. The local resonance can alter the frequency-dependent effective mass densities and/or bulk moduli of the continuum media. In most cases, the internal resonators have highly contrasting elastic properties (Wang et al, 2006). Within the bandgap, the elastic wave cannot propagate, and wave energy is reflected back or temporarily stored in resonators (Liu et al, 2000; Huang and Sun, 2010; Tan et al, 2014).

Because of their two-way electro-mechanical coupling, piezoelectric transducers have been adopted to enhance bandgap behavior in metamaterials (Thorp et al, 2005; Airoldi and Ruzzene, 2011; Wang and Chen, 2016). Many studies employ a negative capacitance element integrated to piezoelectric transducer to reduce the equivalent local stiffness of a unit-cell, thereby tuning the location of bandgap or influencing its bandwidth (Chen et al, 2014; Zhu et al, 2016). Alternatively, piezoelectric metamaterial with periodic resonant circuits can produce directly the local resonance bandgap. Typically, a

piezoelectric metamaterial is a metamaterial or metaplate with periodically arranged piezoelectric transducers (in unimorph or bimorph manner). An inductive load is connected to piezoelectric transducers, and a local resonance is created by the LC (inductor-capacitor) circuit as the piezoelectric transducer acts electrically as a capacitor. The shunt circuits create bandgap in the vicinity of the LC resonance. For example, piezoelectric periodic arrays are integrated into rod for wave attenuation and localization (Thorp et al, 2005). For another example, multi-resonant shunts are adopted to generate multiple bandgaps in a piezoelectric metamaterial (Airoldi and Ruzzene, 2011). Theoretical and experimental investigations on photonic rods and beams (Wang et al, 2011) with shunt circuits have been performed. Notably, piezoelectric metamaterial has advantages over the more conventional mechanical metamaterial (which utilizes only the mechanical displacement/deformation) in two aspects: relatively simple configuration, and adaptivity. Piezoelectric transducers are usually attached to the host structure directly, and even simple topology/geometry can yield complex dynamic phenomena locally at the unit-cell level and globally at the metamaterial level. Moreover, the shunted piezoelectric transducers allow the online tuning of bandgap towards a desired frequency range, as one can conveniently integrate tunable circuitry elements.

So far, almost all the studies on shunted piezoelectric metamaterial are based on the transfer-matrix method or finite element analysis (Casadei et al, 2010; Wang and Chen, 2016). Previous investigations concerning piezoelectric shunt design and analysis in sensing/control applications, however, often resort to the lumped-parameter approach, which can particularly help revealing the underlying physics with the complicated parametric influences (Tang and Wang, 2003; Wang and Tang, 2008; Zhao et al, 2011). It is worth noting that the circuitry dynamics in electrical domain is described naturally by lumped-parameter model. The lumped-parameter approach is suitable to dealing with complex circuitry integration schemes as well as systems with nonlinearity. Indeed, wave propagation in one-dimensional nonlinear periodic structure has been investigated by adopting lumped-parameter analysis, and amplitude-dependent behaviors with tunable dispersion curves and cutoff frequencies are analyzed (Narisetti et al, 2010).

Similar analysis has also been conducted for metamaterial with complex circuits (Hu et al, 2016). It is worth noting that in these studies, while lumped-parameter analyses are performed, the lumped parameters are obtained in an ad hoc manner as they directly start from a discrete model of the mechanical structure. A more common approach is to conduct continuum mechanics based modeling of the host substrate followed by discretization with respect to wavenumber, where an equivalent frequency-dependent Young's modulus is used to reflect the piezoelectric shunt circuit effect (Casadei et al, 2010; Wang and Chen, 2016). In this type of approach, the shunt circuit effect is included as equivalent impedance added to the original mechanical impedance of the transducer. A limitation of this approach is that it may not be able to deal with complex circuitry especially those with multiple branches or nonlinear elements.

The goal of this research is to develop fundamental modeling and understanding of piezoelectric metamaterial integrated with LC shunts to create local resonances. We establish the lumped-parameter model of the piezoelectric metamaterial, which is built upon the continuum mechanics characterization of the host substrate and piezoelectric transducer at the unit-cell level. Transverse wave is considered throughout the modeling and analysis, and the lumped parameters are derived based on the wavenumber involved. Taking advantage of the model, we identify the influence of a key parameter, the system-level electro-mechanical coupling coefficient of the piezoelectric transducer in a unit-cell, to the behavior of the metamaterial. It is found that the bandwidth of the bandgap increases with the electro-mechanical coupling coefficient. We further compare and analyze the characteristics of the unit-cell integrated with piezoelectric transducers connected in parallel and in series, respectively, aiming at assessing circuitry configuration effect.

2.2 Lumped-Parameter Modeling of Piezoelectric Metamaterial

In this section, we formulate a semi-analytical investigation of one-dimensional piezoelectric metamaterial integrated with LC shunt circuits. We first describe the configuration of the unit-cell,

followed by analysis of the potential energy and kinetic energy involved in the system based on continuum mechanics characterization of both the substrate and the transducers. A lumped-parameter model of the piezoelectric metamaterial is formulated by incorporating the periodic boundary condition of unit-cell, where representative circuitry configurations, i.e., serial- and parallel-connections of the piezoelectric transducers, are considered. We then establish the dispersion relations of the piezoelectric metamaterial corresponding to these two connections.

2.2.1 Configuration of piezoelectric metamaterial

The configuration of the piezoelectric metamaterial and the unit-cell is shown in Figure 2-1. The unit-cell consists of an aluminum substrate and two piezoelectric transducers bonded onto the top and bottom surfaces of the substrate. Inductance element is connected to the top and bottom surfaces of the piezoelectric transducer as the shunt circuit. Note that a piezoelectric transducer acts electrically as a capacitor. The combination of the piezoelectric capacitance and the inductive shunt creates an LC resonant unit. Moreover, since the piezoelectric transducer possesses two-way electro-mechanical coupling, the local resonance in electrical domain can affect the system dynamics in mechanical domain. As such, the LC resonance of shunt circuit creates bandgap for the integrated system.

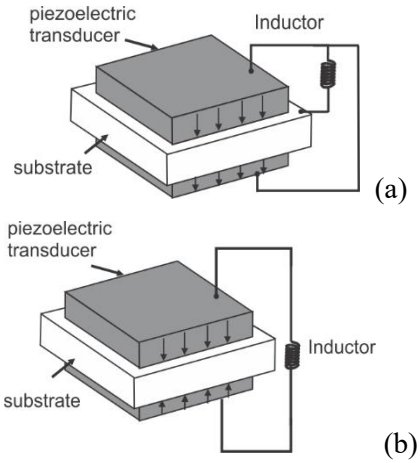

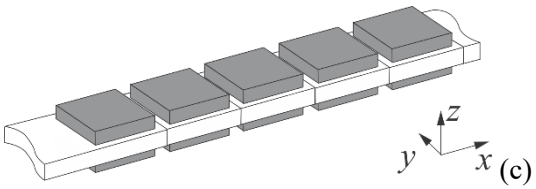

Figure 2-1. (a) Unit-cell with piezoelectric transducers in parallel-connection configuration; (b) Unit-cell with piezoelectric transducers in serial-connection configuration; (c) Configuration of the piezoelectric metamaterial and the coordinate system.

It is known through the research in control and energy harvesting applications that the piezoelectric transducers in a symmetric bimorph can be arranged in series or in parallel. This is certainly applicable to piezoelectric metamaterial synthesis and will be analyzed subsequently. The serial and parallel bimorph configurations are sketched in Figures 2-1(a) and 2-1(b), respectively. Note that, under transverse wave, the instantaneous bending strains in the two piezoelectric transducers have the opposite signs, i.e., one in tension whereas the other in compression. The piezoelectric transducers of the bimorph shown in Figure 2-1(a) are poled in the same direction. This configuration represents the parallel connection of the piezoelectric transducers. Figure 2-1(b) shows the serial connection of the piezoelectric transducers as they are poled in the opposite direction. The unit-cells are then arranged to form a one-dimensional piezoelectric metamaterial, as shown in Figure 2-1(c).

2.2.2 Semi-analytical model of unit-cell

In this research, we use Euler-Bernoulli beam theory as the basis to analyze the integrated system. The behavior of the metamaterial can be assessed through analyzing the dynamics of a unit-cell. For each unit-cell, we assume perfect bonding condition between the piezoelectric transducers and the substrate. The bimorph configurations shown in Figures 2-1(a) and 2-1(b) have the same geometry and material properties. As will be shown later, the governing equations are different for unit-cell with serial- and parallel-connections of piezoelectric transducers. Let l, b, h, and ρ denote, respectively, the length, width, thickness and mass density. Throughout this research, subscripts ‘b’ and ‘p’ are employed to

indicate variables related to the host beam substrate and the piezoelectric transducer, respectively. We begin the modeling by utilizing the extended Hamilton's principle,

$$\int_{t_1}^{t_2} \left(\delta T - \delta U + \delta W \right) dt = 0 \tag{2-1}$$

where T is the kinetic energy, U is the potential energy, and W is the virtual work. For the unit-cell, the kinetic energy is

$$T = \frac{1}{2} \rho_b h_b \int_{-l_b/2}^{l_b/2} \int_{-b_b/2}^{b_b/2} \left(\dot{w}(x,t) \right)^2 dxdy + \rho_p h_p \int_{-l_p/2}^{l_p/2} \int_{b_b/2}^{(b_p+b_b)/2} \left(\dot{w}(x,t) \right)^2 dxdy \tag{2-2}$$

where $w(x,t)$ is the displacement of the transverse wave. The directions of the coordinate system are shown in Figure 2-1(c), and the origin is located at the center of the unit-cell being analyzed. The variation of the kinetic energy takes the form

$$\delta T = \rho_b A_b \int_{-l_b/2}^{l_b/2} \ddot{w}(x,t) \delta w dx + 2 \rho_p A_p \int_{-l_p/2}^{l_p/2} \ddot{w}(x,t) \delta w dx \tag{2-3}$$

where A_b and A_p are, respectively, the cross sectional area of the host beam substrate and that of one piezoelectric transducer. The linear constitutive relation of the piezoelectric transducer is (IEEE, 1987)

$$\tau_p = E_p \varepsilon_p - h_{31} D \tag{2-4a}$$

$$E = -h_{31} \varepsilon_p + \beta_{33} D \tag{2-4b}$$

where τ_p, ε_p, D and E represent, respectively, the stress, stain, electrical displacement (charge/area) and electrical field (voltage/length) of the piezoelectric transducer, and E_p, h_{31} and β_{33} are the Young's modulus at constant electrical displacement, the piezoelectric constant and the dielectric constant of the transducer at constant strain. We let E_b denote the Young's modulus of the host beam substrate. The elastic energy of the unit-cell comes from the host substrate and the two transducers, and the electrical energy comes from the two transducers. The variation of the elastic and electrical energies can be derived

as

$$\delta U = \int_{-l_b/2}^{l_b/2} E_b I_b w'' \delta w'' dx + \int_{-l_p/2}^{l_p/2} E_p I_p w'' \delta w'' dx - 2\int_{-l_p/2}^{l_p/2} F_p h_{31} D \delta w'' dx$$
$$-2\int_{-l_p/2}^{l_p/2} F_p h_{31} w'' \delta D dx + 2\int_{-l_p/2}^{l_p/2} \beta_{33} A_p D \delta D dx \tag{2-5}$$

where I_b and I_p represent, respectively, the second moment of inertia of the substrate and that of one piezoelectric transducer, and F_p represents the first moment of area of each transducer.

Using the variation principle and setting the initial conditions as $\delta w(t_1) = \delta w(t_2) = 0$, we can derive

$$\int_{t_1}^{t_2} \delta T dt = \int_{t_1}^{t_2} \left[\int_{-l_b/2}^{l_b/2} \rho_b A_b \ddot{w}(x,t) \delta w dx + 2\int_{-l_b/2}^{l_b/2} \rho_p A_p \ddot{w}(x,t) \left[H(x+\frac{l_p}{2}) - H(x-\frac{l_p}{2}) \right] \delta w dx \right] dt \tag{2-6}$$

$$\int_{t_1}^{t_2} \delta U dt = \int_{t_1}^{t_2} \begin{bmatrix} (E_b I_b + E_p I_p) w'' \delta w' \big|_{-l_b/2}^{l_b/2} - (E_b I_b + E_p I_p) w''' \delta w \big|_{-l_b/2}^{l_b/2} + \int_{-l_b/2}^{l_b/2} (E_b I_b + E_p I_p) w^{iv} \delta w dx \\ -2\int_{-l_b/2}^{l_b/2} F_p h_{31} D'' \delta w \left[H(x+\frac{l_p}{2}) - H(x-\frac{l_p}{2}) \right] dx - 2F_p h_{31} (D' \delta w' \big|_{-l_p/2}^{l_p/2} - D'' \delta w \big|_{-l_p/2}^{l_p/2}) \\ -2\int_{-l_b/2}^{l_b/2} F_p h_{31} w'' \delta D \left[H(x+\frac{l_p}{2}) - H(x-\frac{l_p}{2}) \right] dx \\ +2\int_{-l_b/2}^{l_b/2} \beta_{33} A_p D \delta D \left[H(x+\frac{l_p}{2}) - H(x-\frac{l_p}{2}) \right] dx \end{bmatrix} dt \tag{2-7}$$

where $H(x)$ is the Heaviside function. As the length and width of the piezoelectric transducer may be smaller than those of the host beam substrate, terms associated with the piezoelectric transducer are multiplied by $\left[H(x+l_p/2) - H(x-l_p/2) \right]$ hereafter. The variation of the virtual work done by forces from adjacent unit-cells (applied at the boundaries) can be expressed as (Huang et al, 2016)

$$\delta W = (E_b I_b + E_p I_p) w'' \delta w' \big|_{-l_b/2}^{l_b/2} - (E_b I_b + E_p I_p) w''' \big|_{-l_b/2}^{l_b/2} - 2F_p h_{31} (D' \delta w' \big|_{-l_p/2}^{l_p/2} - D'' \delta w \big|_{-l_p/2}^{l_p/2}) \tag{2-8}$$

Substituting Equations (2-6--2-8) into Equation (2-1), we obtain the partial differential equations that govern the motion of the unit-cell coupled with the piezoelectric transducers,

$$\left(\rho_b A_b + 2\rho_p A_p\left[H(x+\frac{l_p}{2}) - H(x-\frac{l_p}{2})\right]\right)\ddot{w}(x,t)$$
$$+(E_b I_b + E_p I_p)w^{iv} - 2F_p h_{31} D''\left[H(x+\frac{l_p}{2}) - H(x-\frac{l_p}{2})\right] = W_c(x,t) \quad (2\text{-}9a)$$

$$\left(F_p h_{31} w'' + \beta_{33} A_p D\right)\left[H(x+\frac{l_p}{2}) - H(x-\frac{l_p}{2})\right] = W_s(x,t) \quad (2\text{-}9b)$$

where $W_c(x,t)$ is the virtual work per unit length of the substrate/transducer due to the mechanical damping. In Equation (2-9b), the effect of the shunt circuit, i.e., the inductive load, is included as virtual work done to the unit-cell. Let $W_s(x,t)$ represent such virtual work per unit length of the transducer. The actual virtual work done by the shunt circuit thus is $\int_{-l_b/2}^{l_b/2} W_s(x,t)dx$.

To analyze the dynamic behavior of the piezoelectric metamaterial, we consider one unit-cell and employ the Bloch-Floquet theory, i.e., assuming that the mechanical displacement and the electrical displacement both have the following representations (Collet et al, 2012; Pai et al, 2014),

$$w(x,t) = \bar{q}e^{i(k_x x - \omega t)}, \qquad D(x,t) = \bar{D}e^{i(k_x x - \omega t)} \quad (2\text{-}10a, b)$$

where k_x is the wavenumber of the transverse wave involved, ω is its frequency, and $\bar{q}$ and $\bar{D}$ are, respectively, the amplitudes of mechanical and electrical displacements. We further let $\bar{D}_1$ and $\bar{D}_2$ denote respectively the electrical displacements of the top and bottom transducers. Essentially, these displacement representations reflect that wave propagates in the spatially periodic piezoelectric metamaterial that is spatially periodic. Our goal here is to develop a lumped-parameter model of the unit-cell that can be used to elucidate the underlying physics of the piezoelectric metamaterial. Consider an arbitrary wavenumber k_x. We substitute Equations (2-10a, b) into Equations (2-9a, b), and integrate the equations obtained over the cell length l_b.

Equations (2-10a) and (2-10b) can be re-written as

$$w(x,t)=e^{ik_x x}\cdot\bar{q}e^{-i\omega t},\qquad D(x,t)=e^{ik_x x}\cdot\bar{D}e^{-i\omega t} \tag{2-11}$$

The lumped mechanical and electrical displacements of the unit-cell can be expressed as, respectively

$$q(t)=\bar{q}e^{-i\omega t},\qquad D(t)=\bar{D}e^{-i\omega t} \tag{2-12}$$

Recall Equations (2-9a) and (2-9b). Correspondingly, the partial differential equations that govern the unit-cell dynamics can now be written as

$$\begin{aligned}&\left(\rho_b A_b+2\rho_p A_p\left[H(x+\frac{l_p}{2})-H(x-\frac{l_p}{2})\right]\right)e^{ik_x x}\cdot\ddot{q}(t)\\&+(E_b I_b+E_p I_p)\frac{d^4e^{ik_x x}}{dx^4}\cdot q(t)-2F_p h_{31}\frac{d^2e^{ik_x x}}{dx^2}\left[H(x+\frac{l_p}{2})-H(x-\frac{l_p}{2})\right]\cdot D(t)=W_c(x,t)\end{aligned} \tag{2-13a}$$

$$F_p h_{31}\left[H(x+\frac{l_p}{2})-H(x-\frac{l_p}{2})\right]\frac{d^2e^{ik_x x}}{dx^2}\cdot q(t)+\beta_{33}A_p e^{ik_x x}\cdot D(t)=W_s(x,t) \tag{2-13b}$$

The above two equations can be written in the forms of Equations (2-11a)-(2-11c). Here we have two piezoelectric transducers in one unit-cell, and thus have two transducer equations. Indeed, the coefficients in the lumped-parameter model are given as

$$m=\int_{-l_b/2}^{l_b/2}\left(\rho_b A_b+2\rho_p A_p\left[H(x+\frac{l_p}{2})-H(x-\frac{l_p}{2})\right]\right)e^{ik_x x}dx \tag{2-14a}$$

$$k=\int_{-l_b/2}^{l_b/2}\left(E_b I_b+E_p I_p\right)\frac{d^4e^{ik_x x}}{dx^4}dx \tag{2-14b}$$

$$k_1=\int_{-l_b/2}^{l_b/2}\left(-2F_p h_{31}D''\left[H(x+\frac{l_p}{2})-H(x-\frac{l_p}{2})\right]\right)\frac{d^2e^{ik_x x}}{dx^2}dx \tag{2-14c}$$

$$C=\frac{b_p l_p}{\beta_{33}h_p} \tag{2-14d}$$

After integration, we can obtain the governing equations of the unit-cell

$$m\ddot{q}+c\dot{q}+kq+k_1(Q_1+Q_2)=0 \tag{2-15a}$$

$$1/C\cdot Q_1+k_1 q=V_1 \tag{2-15b}$$

$$1/C\cdot Q_2+k_1 q=V_2 \tag{2-15c}$$

where m is the mass, k is the stiffness, c is the damping coefficient, q is the mechanical displacement, i.e., $q=\bar{q}e^{-i\omega t}$, Q_1 and Q_2 are the charges on the transducers on the top and bottom of the substrate respectively, i.e., $Q_1=(b_p l_p)\bar{D}_1 e^{-i\omega t}$ and $Q_2=(b_p l_p)\bar{D}_2 e^{-i\omega t}$, C is the capacitance of one piezoelectric transducer, k_1 is the electro-mechanical parameter between a transducer and the host beam substrate. Specifically, we have

$$m=\frac{2\sin(\frac{k_x l_b}{2})}{k_x l_b}\rho_b h_b b_b l_b+\frac{2\sin(\frac{k_x l_b}{2}\frac{l_p}{l_b})}{k_x l_b}2\rho_p h_p b_p l_b$$

$$k=2E_b I_b {k_x}^3\sin(\frac{k_x l_b}{2})+4E_p I_p {k_x}^3\sin(\frac{k_x l_b}{2}\frac{l_p}{l_b}) \tag{2-16a-d}$$

$$k_1=-2\frac{F_p h_{31} k_x}{b_p l_p}\sin(\frac{k_x l_b}{2}\frac{l_p}{l_b}),\qquad C=\frac{b_p l_p}{\beta_{33} h_p}$$

It is worth noting that, in the unit-cell, two piezoelectric transducers are employed as a bimorph. The top and bottom piezoelectric transducers are identical and thus have the same capacitance value. The charges, Q_1 and Q_2, and the voltages across the transducers, V_1 and V_2, are related to the specific connection configurations and will be explained subsequently. More importantly, the equivalent mass, stiffness, and electro-mechanical constant are expressed as explicit functions of wavenumber and geometry/material properties. Indeed, in piezoelectric metamaterial, wave propagates along the continuous beam substrate. The wavenumber indicates the number of waveform cycles per unit length, which decides the corresponding local beam deformation and strain/stress distributions within the unit-cell. Therefore, the equivalent mass, stiffness, and electro-mechanical constant are all wavenumber-dependent.

2.2.3 Piezoelectric metamaterial with piezoelectric transducers in parallel-connection configuration

We now investigate the effect of the circuitry dynamics to unit-cell behavior. We first analyze the piezoelectric unit-cell where the transducers are connected to the inductive shunt in the parallel manner, as shown in Figure 2-1(a). In order to derive the governing equations of the integrated system, we first examine the electrical dynamics of the unit-cell. Figure 2-2(a) illustrates the equivalent circuit model. The electrodes bracketing the piezoelectric transducers cover fully the top and the bottom surfaces of each transducer. The electrode layers are connected to an inductive circuit/load. Here we equate the piezoelectric transducer to a voltage source in the equivalent circuit model (Wang and Tang, 2008). A piezoelectric transducer generates electrical displacement due to the mechanical strain, thereby acting as a voltage source. The only cause of mechanical strain is assumed to be the axial strain due to bending wave. Since the charge generations of the parallel- and serial-connection configurations are different, the piezoelectric coupling effect in the mechanical equation is expected to be different. Thus, in what follows, the mechanical response expressions of the parallel- and serial-connection configurations are denoted by $q_\alpha(t)$ and $q_\beta(t)$, respectively. Hereafter subscripts α and β are used to indicate parameters related to the parallel- and serial-connection configurations, respectively.

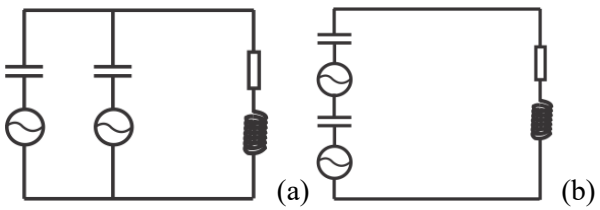

Figure 2-2. Equivalent circuit models for unit-cell with piezoelectric transducers: (a) parallel-connection configuration; (b) serial-connection configuration

The governing equations of a unit-cell integrated with transducers connected with the inductive shunt

in the parallel manner can be written as

$$m\ddot{q}_\alpha + c\dot{q}_\alpha + kq_\alpha + k_1(Q_1 + Q_2) = 0 \tag{2-17a}$$

$$L_\alpha(\ddot{Q}_1 + \ddot{Q}_2) + R(\dot{Q}_1 + \dot{Q}_2) + 1/C \cdot Q_1 + k_1 q_\alpha = 0 \tag{2-17b}$$

where L_α is the inductance value adopted under the parallel-connection configuration, and R is the inherent resistance in the circuitry elements. In this parallel-connection, as the piezoelectric transducers attached onto the top and bottom surfaces of the host substrate are identical, the instantaneous charges on the two transducers are equal to each other, i.e., $Q_1(t) = Q_2(t)$. To evaluate the unit-cell dynamic characteristics, we assume harmonic responses with frequency ω, i.e., $q_\alpha(t) = q_{\alpha 0} e^{i(-\omega t + \phi_1)}$, $Q_1(t) = Q_0 e^{i(-\omega t + \phi_2)}$, and $Q_2(t) = Q_0 e^{i(-\omega t + \phi_3)}$, where ϕ_1, ϕ_2 and ϕ_3 are the phases. For a two-DOF (degree-of-freedom) unit-cell governed by Equations (2-17a, b), the dispersion equation under the undamped condition can be derived as

$$\left(-\omega^2 m + k\right)\left(-2\omega^2 L_\alpha + 1/C\right) - 2k_1^2 = 0 \tag{2-18}$$

We introduce the notations of the resonant frequency of the original unit-cell (before the circuitry is integrated) and that of the LC shunt with parallel connected transducers as, respectively,

$$\omega_0^2 = k/m, \qquad \omega_\alpha^2 = 1/(2L_\alpha C) \tag{2-19a, b}$$

Meanwhile, based on the equations of motion (Equations (13a, b)), we can define an important parameter, the non-dimensional system-level electro-mechanical coupling coefficient (Wang and Tang, 2008), as

$$k_e^2 = \frac{k_1^2 C}{k} = \frac{\left(-2\frac{F_p h_{31} k_x}{b_p l_p}\sin(\frac{k_x l_b}{2}\frac{l_p}{l_b})\right)^2}{\left(2E_b I_b {k_x}^3 \sin(\frac{k_x l_b}{2}) + 4E_p I_p {k_x}^3 \sin(\frac{k_x l_b}{2}\frac{l_p}{l_b})\right)\frac{\beta_{33} h_p}{b_p l_p}} \tag{2-20}$$

As indicated by a number of previous studies concerning piezoelectric transducer-based sensing and

control, this system-level electro-mechanical coupling coefficient reflects quantitatively the two-way energy conversion between the mechanical and electrical domains (Zhao et al, 2011; Xu and Tang, 2015). Larger k_e indicates stronger electro-mechanical coupling and therefore more effective energy conversion between the mechanical and the electrical domains through the transducers. The role of electro-mechanical coupling coefficient warrants further discussion here. Apparently, according to Equation (16), this non-dimensional coupling coefficient is predominantly related to the transducer material property, h_{31}, i.e., the piezoelectric coupling constant at the material-level. It is also related to the piezoelectric capacitance, the Young's moduli, the geometry of the substrate and the transducers, and the wavenumber involved. It can be increased with the integration of negative capacitance element or negative stiffness effect (Wang and Tang, 2008; Chen et al, 2014; Xu and Tang, 2015). Figure 2-4 shows a representative relation between the system level electro-mechanical coupling coefficient and normalized wavenumber (to be further analyzed in detail in Section 3), which indicates that the wavenumber plays an important role. The reason is that under different wavenumbers the local deformations of the substrate are different, yielding different system-level electro-mechanical coupling effects. Therefore, there is great potential of performing optimal design of circuit as well as unit-cell material/geometry for specific applications to increase the system-level electro-mechanical coupling.

Since in this configuration two piezoelectric transducers are connected in parallel, the overall piezoelectric capacitance is $2C$. The resonant frequency of the unit-cell is wavenumber-dependent because both m and k are wavenumber-dependent, while the resonant frequency of the shunt circuit is determined by the inductance selected. The dispersion equation can be re-written as

$$\left(-\frac{\omega^2}{\omega_0^2}+1\right)\left(-\frac{\omega^2}{\omega_\alpha^2}+1\right)-2k_e^2=0 \tag{2-21}$$

Recall that the local LC resonant frequency (ω_α^2) is usually much smaller than the Bragg scattering frequencies (ω_0^2). From Equation (2-21) we can observe that, fundamentally, the dispersion relation is

decided by both the circuit resonant frequency and the system level electro-mechanical coupling coefficient. The solutions to the dispersion equation under the parallel-connection configuration can be easily obtained as

$$\omega_{L\alpha} = \frac{\sqrt{2}}{2}\sqrt{\omega_0^2 + \omega_\alpha^2 - \sqrt{(\omega_0^2 - \omega_\alpha^2)^2 + 8k_e^2\omega_0^2\omega_\alpha^2}}\ , \qquad \omega_{H\alpha} = \frac{\sqrt{2}}{2}\sqrt{\omega_0^2 + \omega_\alpha^2 + \sqrt{(\omega_0^2 - \omega_\alpha^2)^2 + 8k_e^2\omega_0^2\omega_\alpha^2}}$$

(2-22a, b)

The results under a representative parametric combination are plotted in Figure 4(a) as functions of wavenumbers. Indeed, from Figure 2-5, we can observe the bandgap obtained in this piezoelectric metamaterial. From Equations (2-22a) and (2-22b) and Figure 2-4, we can conclude that the LC resonant frequency determines the bandgap location while the system-level electro-mechanical coupling coefficient determines the bandgap width. Quantitative assessment of the bandgap will be systematically analyzed in next Section.

2.2.4 Piezoelectric metamaterial with piezoelectric transducers in serial-connection configuration

We then consider the serial-connection configuration as shown in Figures 2-1(b), and the equivalent circuit model is shown in Figure 2-2(b). It is worth noting that in this serial-connection, the top and bottom piezoelectric transducers have opposite poling and thus the respective h_{31} terms have opposite signs. The governing equations of a unit-cell integrated with transducers connected with the inductive shunt in serial manner can be written as

$$m\ddot{q}_\beta + c\dot{q}_\beta + kq_\beta + 2k_1Q_1 = 0 \tag{2-23a}$$

$$L_\beta\ddot{Q}_1 + R\dot{Q}_1 + 2/C \cdot Q_1 + 2k_1q_\beta = 0 \tag{2-23b}$$

where L_β is the inductance value adopted under the serial-connection configuration. Here the instantaneous charges on the two transducers are opposite to each other due to the opposite poling, i.e.,

$Q_1(t) = -Q_2(t)$. Again, we assume harmonic responses of unit-cell displacement and charges on the transducers. The dispersion equation under the undamped condition can be obtained as

$$\left(-\omega^2 m + k\right)\left(-\omega^2 L_\beta + 2/C\right) - 4k_1^2 = 0 \tag{2-24}$$

Let the resonant frequency of the LC shunt with serially connected transducers be denoted as,

$$\omega_\beta^2 = 1/(L_\beta \cdot C/2) \tag{2-25}$$

Here the overall piezoelectric capacitance is $C/2$ since two piezoelectric transducers are connected in series. Recall that the resonant frequency of the original unit-cell (before the circuitry is integrated) is denoted as $\omega_0^2 = k/m$. Similar to that under the parallel-connection configuration, the resonant frequency of the unit-cell is wavenumber-dependent, while the resonant frequency of the shunt circuit is determined by the inductance selected. The dispersion equation under the serial-connection configuration can be re-written as

$$\left(-\frac{\omega^2}{\omega_0^2} + 1\right)\left(-\frac{\omega^2}{\omega_\beta^2} + 1\right) - 2k_e^2 = 0 \tag{2-26}$$

The solutions to the dispersion equation can be obtained as

$$\omega_{L\beta} = \frac{\sqrt{2}}{2}\sqrt{\omega_0^2 + \omega_\beta^2 - \sqrt{(\omega_0^2 - \omega_\beta^2)^2 + 8k_e^2\omega_0^2\omega_\beta^2}}, \qquad \omega_{H\beta} = \frac{\sqrt{2}}{2}\sqrt{\omega_0^2 + \omega_\beta^2 + \sqrt{(\omega_0^2 - \omega_\beta^2)^2 + 8k_e^2\omega_0^2\omega_\beta^2}}$$

(2-27a, b)

The results are generally similar to those under the parallel-connection configuration. The parallel- and the serial-connections have the same dispersion relation features. Meanwhile, if we want to create the same bandgap, the two types of unit-cells need to have different inductive loads. Specifically, the inductive loads in the parallel-connection and that in the serial-connection should satisfy $L_\beta = 4L_\alpha$.

2.3 Case Analyses and Discussions

In this section, we present systematic parametric analyses of the piezoelectric metamaterial, using the semi-analytical results derived. All propagating wave modes in lattice/periodic structures can be captured by restricting the dimensionless wavenumber to the first Brillouin zone due to the periodicity. Thus, we plot the dispersion curves based on wavenumbers within this zone. In the following discussion, unless otherwise noted, the parameters employed are listed in Table 1. For comparison purpose, a finite element model based on previous literature (Casadei et al, 2010; Wang and Chen, 2016) is formulated and analyzed.

Table 1. Parameters employed in case analyses.

l_b (m)	0.02538	b_b (m)	0.02538	h_b (m)	0.00313
l_p (m)	0.021	b_p (m)	0.021	h_p (m)	0.00055
E_b (GPa)	69	E_p (GPa)	65	ρ_b (kg/m^3)	2,700
ρ_p (kg/m^3)	7,700	h_{31} (N/C)	-8.76×10^8	β_{33} (Wm/C)	5.345×10^7

2.3.1 Formulation of Finite Element Analysis

A two-dimensional finite element analysis based on plate model is performed for validation and comparison. In finite element formulation, we extend the constitutive relation shown in Equations (2-4a) and (2-4b) into the three dimensional form, and adopt 20-node plate element for discretization. Similar to that presented by Casadei et al (2010), we can obtain the mass and stiffness matrices as well as the electro-mechanical coupling vector, denoted as M, K, and $\mathbf{k}_1$, respectively. We let C represent the piezoelectric capacitance.

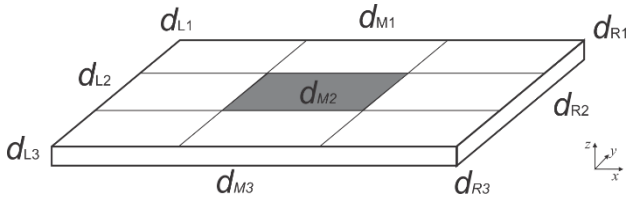

Figure 2-3. Schematic of boundary displacement vector composition of a unit-cell.

The unit-cell with finite element mesh is schematically shown in Figure 2-3. The shaded area indicates the piezoelectric transducer location. Care should be taken on the finite element displacement vector d. We partition d as

$$\mathbf{d} = [d_{L1}\ d_{L2}\ d_{L3}\ d_{M1}\ d_{M2}\ d_{M3}\ d_{R1}\ d_{R2}\ d_{R3}]^T \tag{2-28}$$

where the vector components are shown in Figure 10. According to the Bloch theorem for periodically arranged unit-cells, the relation of the displacements within a unit-cell can be specified as

$$d_{L1} = e^{ik_y l_b} d_{L3}, \qquad d_{M1} = e^{ik_y l_b} d_{M3}, \qquad d_{R2} = e^{ik_x l_b} d_{L2},$$

$$d_{R3} = e^{ik_x l_b} d_{L3}, \qquad d_{R1} = e^{i(k_x + k_y) l_b} d_{R3} \tag{2-29a-e}$$

where k_x and k_y are the wavenumbers in the *x*- and *y*-direction, respectively. Note that the transverse wave is predominantly propagating in the *x*-direction. The wavenumber in the *y*-direction k_y is set as zero in the finite element simulation. We apply the abovementioned periodic boundary conditions and assume harmonic responses. The dispersion relation can be obtained by solving the following eigenvalue problem,

$$\begin{bmatrix} -\omega^2 \mathbf{M} + \mathbf{K} & 2\mathbf{k}_1 \\ 1/2\mathbf{k}_1^T & -\omega^2 L + 1/(2C) \end{bmatrix} \begin{bmatrix} \mathbf{d} \\ Q \end{bmatrix} = 0 \tag{2-30}$$

where *L* is inductance in the shunt circuit. Here for illustration we only show the equation corresponding to the parallel-connection configuration. *Q* is the total charge on the electrode of one piezoelectric transducer. The parameters used in finite element simulation are provided in Table 1.

2.3.2 Bandgap behavior under parallel-connection configuration

We consider the unit-cell with the parallel-connection configuration (Figure 2-1(a) and Figure 2-2(a)). The dispersion curve of the unit-cell is calculated in the first Brillouin zone, which is applied on a single unit-cell in the reciprocal lattice space. The characteristics of wave propagation in this region will yield the bandgap structure for the whole metabeam.

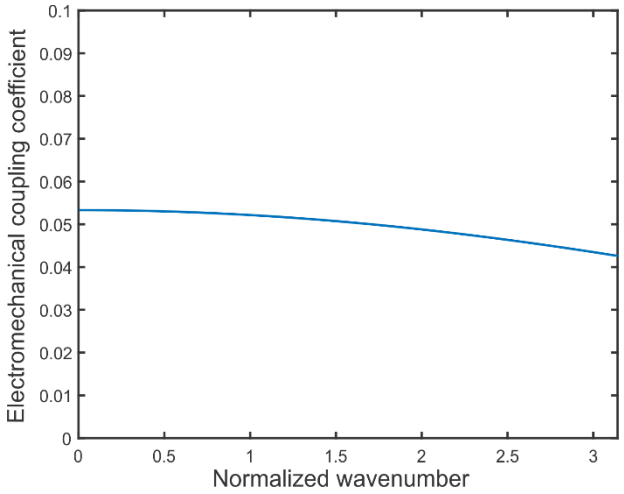

Figure 2-4. System level electro-mechanical coupling coefficient versus wavenumber.

As identified in Section 2.2.3, a key parameter for this piezoelectric metamaterial is the system-level electro-mechanical coupling coefficient k_e. Figure 2-4 shows the relation of the system-level electro-mechanical coupling coefficient versus normalized wavenumber $k_x l_b$. In the first Brillouin zone, the normalized wavenumber ranges from 0 to π. It can be observed that the electro-mechanical coupling coefficient has a value in the range of 0.053 to 0.043. The electro-mechanical coupling coefficient decreases with the increase of wavenumber. When the wavenumber is larger, the distribution of local deformation becomes more uneven, yielding lower electro-mechanical coupling.

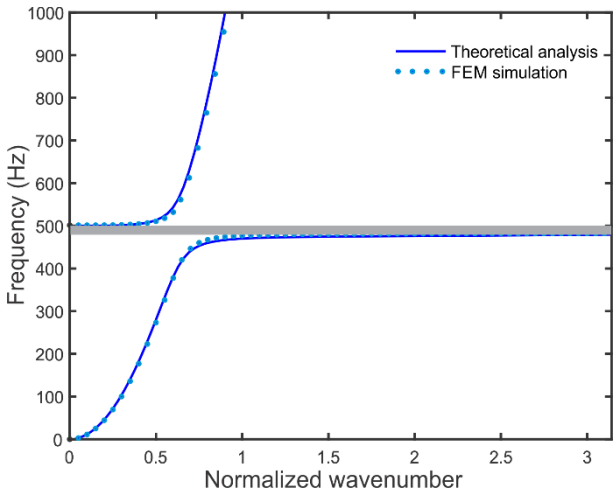

Figure 2-5. Dispersion curve of the unit-cell with parallel-connection configuration.

Without loss of generality, we select the resonant frequency of the LC shunt circuit as 500 Hz. It is worth mentioning that due to the adaptiveness of the LC shunt circuit, the LC resonance can be set at other frequencies. Figure 2-5 shows the corresponding dispersion curve (Equation (14)) of the unit-cell with piezoelectric transducers in parallel-connection configuration. The integration of the piezoelectric circuitry creates a bandgap with a range between 479.4 Hz and 500 Hz. The bandgap width is 20.6 Hz. In comparison, Figure 2-5 also gives the finite element simulation result based on the same parametric combination. In finite element analysis, under a given wavenumber, we enforce the Floquet periodic boundary condition onto the unit-cell. Solving the subsequent eigenvalue problems under varying wavenumbers then yields the dispersion relation. The finite element results match with the semi-analytical results well. The bandgap width is 19.8 Hz under the finite element analysis.

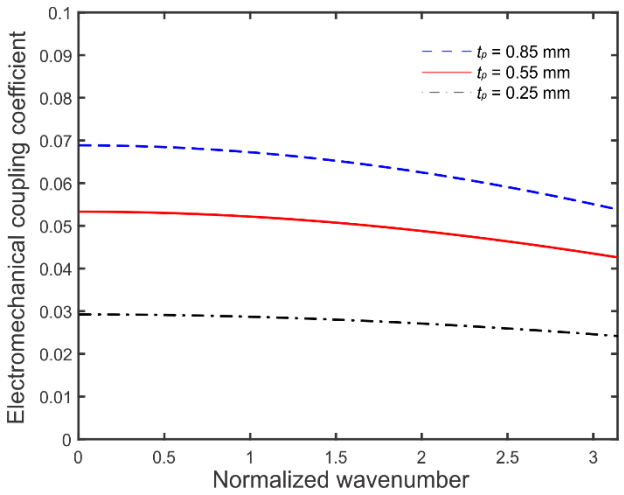

Figure 2-6. System level electro-mechanical coupling coefficients versus wavenumber under different transducer thicknesses, parallel-connection.

A number of factors affect the system-level electro-mechanical coupling coefficient. As aforementioned, the coupling coefficient is related to the transducer material property, the capacitance, the Young's moduli, the geometry of the substrate and the transducers, and the wavenumber involved. Here we specifically analyze the effect of the thickness of the piezoelectric transducers, and keep all other parameters unchanged. Figure 2-6 plots the system-level electro-mechanical coupling coefficient versus wavenumber under three different thickness values, 0.25 mm, 0.55 mm and 0.85 mm. In all three cases, the coupling coefficients decrease as the wavenumber increases. The unit-cell with 0.25 mm thickness piezoelectric transducers has coupling coefficient ranging from 0.024 to 0.029. Increasing the thickness of the piezoelectric transducer increases the coupling coefficient. A unit-cell with 0.85 mm thickness piezoelectric transducers has coupling coefficient ranging from 0.054 to 0.069.

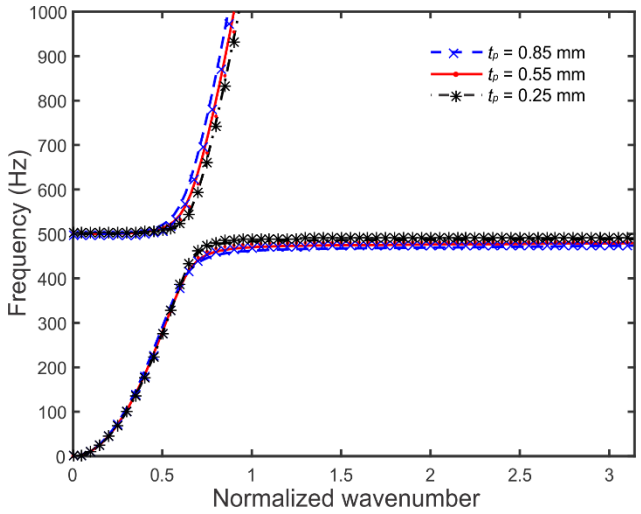

Figure 2-7. Dispersion curves of the unit-cell with parallel-connection configuration under different transducer thicknesses. (dash lines: lumped-parameter model; star points: FEM simulation)

Plotted in Figure 2-7 are three dispersion curves corresponding to the aforementioned three thickness values of the piezoelectric transducers. It can be readily observed that increasing the thickness of the piezoelectric transducer can effectively increase the bandgap width. The unit-cell with 0.25 mm thickness transducers has a bandgap width of 11.6 Hz. The unit-cell with 0.85 mm thickness transducers has a bandgap width of 26.2 Hz. Fundamentally, as wave propagates through the piezoelectric metamaterial, each unit-cell experiences local deformation which then yields energy conversion from the mechanical domain to the electrical domain through the direct piezoelectric effect. The charge flow in the LC shunt, meanwhile, induces the reverse piezoelectric effect which converts electrical energy back to the mechanical energy, i.e., creating a reactive force to the unit-cell to affect the wave propagation characteristics. The two-way energy conversion efficiency is determined by the system-level electro-mechanical coefficient which is exactly analogous to the mass ratio (Huang and Sun, 2010) in conventional metamaterial employing local mechanical resonator in the unit-cell. In all these cases, the results obtained based on the semi-analytical analysis match with the finite element results well.

2.3.3 Bandgap behavior under serial-connection configuration

We then consider the unit-cell with the serial-connection configuration (Figure 2-1(b) and Figure 2-2(b)). Similarly, we select the resonant frequency of the LC shunt circuit as 500 Hz. Figure 2-8 plots the system-level electro-mechanical coupling coefficients under three different piezoelectric transducer thickness values, 0.25 mm, 0.55 mm, and 0.85 mm. The results are essentially the same as those under parallel-connection (Figure 2-6). This is because that the electro-mechanical coupling fundamentally is determined by the local host substrate deformation and piezoelectric capacitance, and is independent of the inductive load. The corresponding dispersion curves are plotted in Figure 8, which again are the same as those shown in Figure 2-7. We can conclude that, when inductive load is integrated, as long as the LC shunt resonant frequency and the electro-mechanical coupling coefficient are the same, the parallel- and serial-connection will yield the same dispersion curves and the same bandgap behavior.

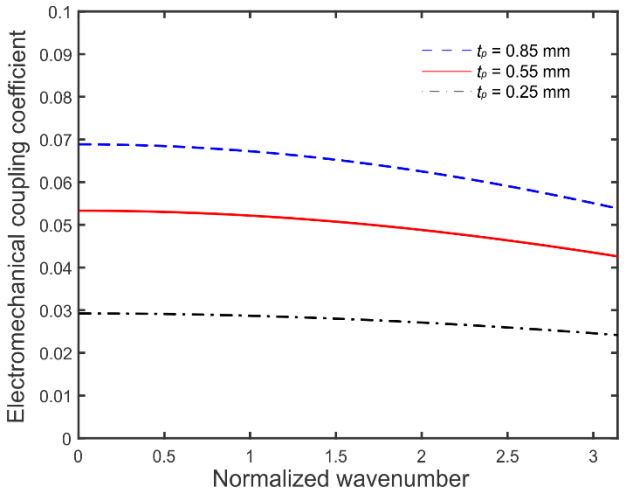

Figure 2-8. System level electro-mechanical coupling coefficients versus wavenumber under different transducer thicknesses, serial-connection.

It is, however, worth mentioning that, in order for the parallel- and serial-connection configurations to have the same shunt circuit resonant frequency, the inductance under the serial-connection will be four times of that under the parallel-connection, i.e., $L_\beta = 4L_\alpha$. The parallel-connection has an advantage in

terms of inductor size if passive inductors are used, because large inductance is more difficult to achieve passively. On the other hand, the unit-cell with serially connected piezoelectric transducers has twice higher voltage output than that with parallel-connection configuration. The serial-connection may have advantage where diodes might be integrated, i.e., the voltages must overcome the Schottky barrier of diodes (Lallart et al, 2015).

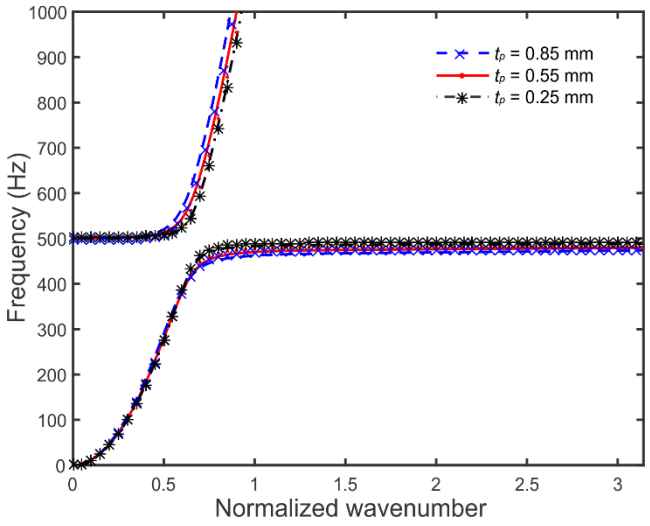

Figure 2-9. Dispersion curves of the unit-cell with serial-connection configuration under different transducer thicknesses. (dash lines: lumped-parameter model; star points: FEM simulation)

2.3.4 Adaptiveness due to circuitry tuning

An important advantage of piezoelectric metamaterial is that the bandgap behavior could be adjusted online by tuning circuitry elements. For example, tunable negative capacitance elements have been employed in piezoelectric metamaterial synthesis (Wang and Tang, 2008; Chen et al, 2014). The negative capacitance is realized through a negative impedance converter (NIC) (Tang and Wang, 2001). Recall Equation (16). What a negative capacitance element does is essentially cancelling out the inherence impedance of the piezoelectric transducer. Equivalently speaking, a negative capacitance element can reduce the system-level stiffness of the unit-cell. This integration can certainly be incorporated into the

configurations studied in this research, i.e., connecting a negative capacitance element in series with the piezoelectric transducers. In the past, tunable inductances based on op-amp circuit design have also been employed in vibration control and sensor development (Wang and Tang, 2008) as well as in metamaterial synthesis (Wang et al, 2010). Such synthetic inductance has another advantage of being compact in size. Integrating tunable inductance with the piezoelectric metamaterial studied in this paper will yield significant adaptiveness. Without loss of generality, here we present dispersion curves of the unit-cell with piezoelectric transducers in parallel-connection configuration under different inductance tuning.

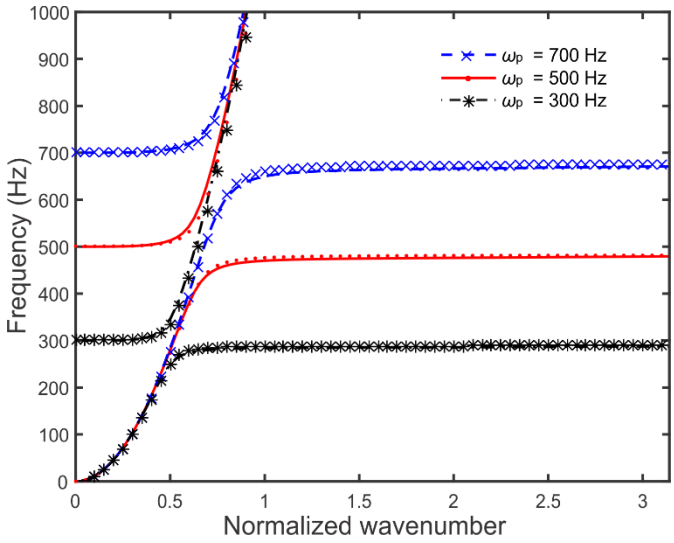

Figure 2-10. Adaptiveness of the piezoelectric metamaterial. (dash lines: lumped-parameter model; star points: FEM simulation)

We tune the inductances to realize three different LC shunt resonant frequencies, 300 Hz, 500 Hz, and 700 Hz. Bandgaps can be generated in the vicinities of these local resonant frequencies. Obviously, here we are able to adjust the frequency range of the bandgaps without making any change to the mechanical and electrical configurations. Moreover, it can be observed that the width of the bandgap increases with the increase of the LC resonant frequency. The unit-cell with LC resonant frequency $\omega_\alpha = 300$ Hz has a bandgap width of 12.4 Hz. When the LC resonant frequency increases to $\omega_\alpha = 700$ Hz, the bandgap width increases to 29.1 Hz. This result can be explained by observing Equation (18). As the electro-

mechanical coupling coefficient remains unchanged here, the ratio of the bandgap width with respected to the local resonant frequency $\omega^2 / \omega_\alpha^2$ will remain unchanged. Consequently, when ω_α increases, the frequencies that define the bandgap boundaries increase as well.

2.4 Conclusion

In this section, we study piezoelectric metamaterial based on piezoelectric transducers and inductive loads. A lumped-parameter, semi-analytical model of piezoelectric metamaterial is formulated based on continuum mechanics characterization. The equivalent unit-cell mass, stiffness, and electro-mechanical coupling parameter are derived and identified as wavenumber-dependent. Dispersion curves corresponding to piezoelectric circuitry with bimorph transducers under parallel-connection and serial-connection are obtained. The role of the system-level electro-mechanical coupling is identified and analyzed in detail. While the frequency range of the bandgap is determined by the LC circuit resonant frequency, the bandwidth of the bandgap is primarily determined by the electro-mechanical coupling. The parametric analyses are validated by finite element simulations. The adaptiveness of this piezoelectric metamaterial, which can be realized through online tuning of the inductance, is also discussed. The formulation and results obtained can be used to guide the circuitry synthesis and design optimization of the piezoelectric metamaterial.

Chapter 3 Piezoelectric Metamaterial based Wave Guiding

3.1 Introduction

Metamaterial, defined as artificial structures that exhibit physical properties not available in natural material, has extraordinary capability in low-frequency sound/vibration attenuation, negative refraction, and super lenses (Landy et al, 2008; Pendry and Li, 2008; Yang et al, 2010; Baravelli and Ruzzene, 2013; Yoo et al, 2014). The acoustic metamaterial, consisting of periodically arranged local microstructures or unit-cells integrated to a host medium, can manipulate elastic wave propagation. The local resonance mechanism utilizes the sub-wavelength local resonances induced within a unit-cell. The local resonance can alter the frequency-dependent effective mass densities and/or bulk moduli of the continuum media. In most cases, the internal resonators have highly contrasting elastic properties (Wang et al, 2006). Within the bandgap, the elastic wave cannot propagate, and wave energy is reflected or temporarily stored in resonators and can be adopted for energy harvesting (Huang and Sun, 2010; Tan et al, 2014; Hu et al, 2017a; Hu et al, 2017b).

Recently, metamaterial-based acoustic wave-guiding has received significant attention. Various types of unit-cell microstructures are adopted. For example, a two-dimensional GRIN lens, comprised of cylinders with different diameters or unit-cells with cross-shaped apertures, is proposed (Climente et al, 2010). Wave-guiding systems have seen applications in fault detection and energy harvesting. By utilizing local resonance, a two-dimensional planar array can focus acoustic waves for enhanced fault detection sensitivity (Yan et al, 2013). Notably, piezoelectric metamaterial has recently emerged as a new option in acoustic wave guiding. For instance, piezoelectric transducers are assembled in rectangular array to generate strong, frequency-dependent directional beaming (Senesi et al, 2010). A spiral-shaped transducer is proposed for frequency-based beam steering and applied to enhanced directional sensing (Baravelli et al, 2013). By taking advantage of multiple embedded acoustic metamaterial lenses, directional acoustic wave guiding is also achieved at corresponding frequencies (Zhu and Semperlotti, 2014). Although promising, these systems share one common limitation that they cannot arbitrarily

manipulate acoustic wave under a given frequency as the layout/geometry to facilitate wave-guiding is fixed.

Because of their two-way electro-mechanical coupling, piezoelectric transducers have been adopted to enhance bandgap behavior in metamaterials (Thorp et al, 2005; Wang and Chen, 2016). An inductive load is connected to piezoelectric transducers, and a local resonance is created by the LC (inductor-capacitor) circuit as the piezoelectric transducer acts electrically as a capacitor. The shunt circuits create bandgap in the vicinity of the LC resonance. For example, piezoelectric periodic arrays are integrated into rod for wave attenuation and localization (Thorp et al, 2005). For another example, multi-resonant shunts are adopted to generate multiple bandgaps in a piezoelectric metamaterial (Airoldi and Ruzzene, 2011). Note that the typical acoustic GRIN lens has as the layout/geometry to facilitate wave-guiding is fixed. On the other hand, the piezoelectric metamaterial process the advantages of adaptiveness. Recently, the piezoelectric transducers are integrated into the acoustic GRIN lens. On the other hand, the negative capacitance circuit is easily to lost stability since it has a positive feedback loop, which is similar to Wen's Oscillating Bridge for sinusoidal signal generation.

3.2 Piezoelectric Acoustic Prism for Wave Guiding

3.2.1 Design of acoustic prism

Piezoelectric transducers possess two-way electro-mechanical coupling, and circuitry elements in the electrical domain can realize online tunability easily (e.g., a tunable synthetic inductor shown in Figure 1(a)). In this research, we demonstrate that piezoelectric metamaterial can be designed to have features of adaptive wave guiding at a single frequency. A unit-cell of the piezoelectric metamaterial is shown in Figure 3-1(a). It consists of two piezoelectric discs bonded onto a host medium. An inductor is connected to the two transducers in parallel. The inductor can be realized by utilizing op-amp circuit (Wang and Tang, 2008). This type of synthetic inductor is adaptive and tunable online. Note that the piezoelectric transducer acts electrically as a capacitor. The combination of the piezoelectric capacitance

and the inductive shunt circuit creates a local LC resonant unit.

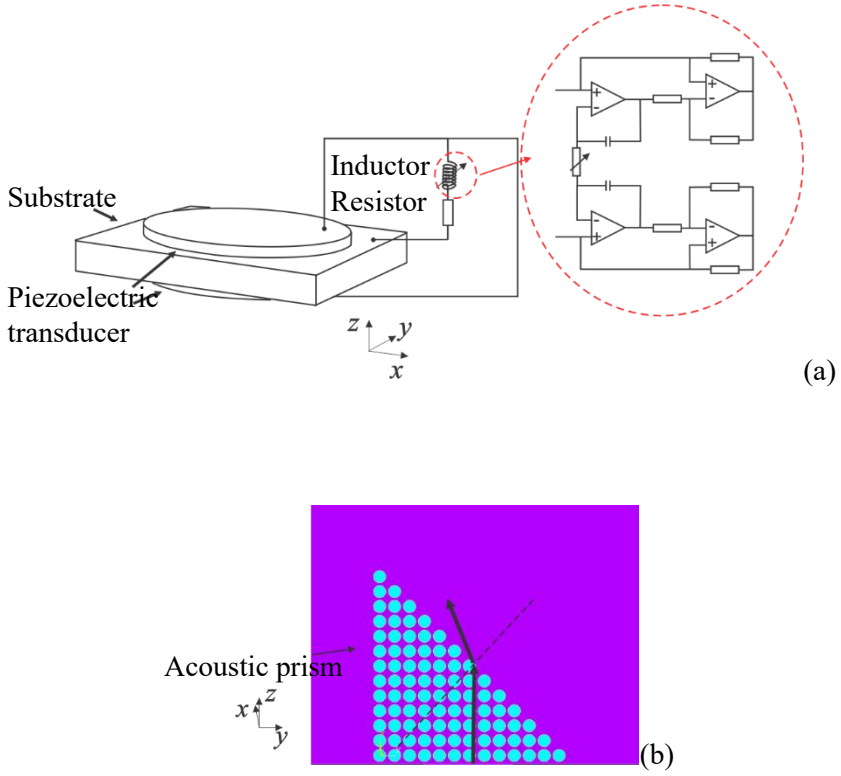

Figure 3-1. (a) Configuration of a unit-cell with piezoelectric inductive shunt; (b) Configuration of the acoustic prism.

Indeed, there have been recent studies utilizing piezoelectric metamaterial integrated with shunt circuits for wave attenuation and localization (Airoldi and Ruzzene, 2011; Wang et al, 2011; Chen et al, 2012; Casadei et al, 2012; Zhou et al, 2015; Xu et al, 2016). It is well-known in optics that natural light can be dispersed through a prism as wave components with different speeds (under different frequencies) in the light yield different refraction angles when passing through the prism. This gives rise to our fundamental idea of tunable beam steering, i.e., to utilize the acoustic wave velocity shifting in the vicinity of local resonant frequency of the LC shunt in piezoelectric metamaterial, where the tunability is realized by inductance tuning. Our hypothesis is that such shifting of the velocity of acoustic wave, combined with the prism-like triangle-arrangement of unit-cells, will lead to a beam steering effect in the host medium. This metamaterial synthesis is achieved by attaching/bonding arrayed piezoelectric

transducers, which are connected with tunable inductors individually, to a structural medium whereas the structure remains unchanged. For illustration simplicity and without loss of generality, here we adopt an isosceles right-triangle shaped piezoelectric metamaterial prim integrated to a homogenous aluminum plate (Figure 3-1(b)).

3.2.2 Modeling of unit-cell and fundamental dynamic characteristics

Towards the acoustic wave, we focus on harmonic transverse wave. In other words, the bending wave travelling in the plate. Consider a transverse wave propagating in the ΓX direction through the area integrated with the prism. Here, the ΓX direction indicates the x-direction shown in Figure 3-1(b). The refraction angles of the acoustic wave are then analyzed. According to the well-known Snell's law, the ratio of refraction angle and incidence angle is proportional to the ration of phase velocities. As the wave propagates predominantly along the ΓX direction, the phase velocity of harmonic transverse wave can be approximated by the phase velocity along this direction. The unit-cell displacement of the nth transverse wave along the ΓX direction is

$$w(x,t) = x_0 e^{i(nk_{\Gamma X}x-\omega t)} \tag{3-1}$$

where $k_{\Gamma X}$ is the wavenumber in the ΓX direction and x_0 is the amplitude of the acoustic wave. To elucidate the key characteristic of wave propagation in the vicinity of the bandgap, the governing equations of the piezoelectric unit-cell are derived. Extended Hamilton's principle is adopted, and the Bloch-Floquet periodic boundary conditions are considered. The piezoelectric transducers generate electric displacement due to mechanical strain, and are considered as voltage sources in electrical domain. The details of derivation of the parameters and equations can be found in Section 2. For the unit-cell shown in Figure 3-1(a), we have the following lumped-parameter model,

$$M\frac{d^2x}{dt^2}x + c\frac{dx}{dt} + Kx + k_1(Q_1 + Q_2) = 0 \tag{3-2a}$$

$$L\left(\frac{d^2Q_1}{dt^2}+\frac{d^2Q_2}{dt^2}\right)+R\left(\frac{dQ_1}{dt}+\frac{dQ_2}{dt}\right)+\frac{1}{C}Q_1+k_1x=0 \tag{3-2b}$$

where Q_1, Q_2 and x are charge on the top transducer, charge on the bottom transducer, and lumped displacement of the unit-cell; M, K, c, R, k_1, C and L represent, respectively, the mass, stiffness, mechanical damping coefficient, resistance in the shunt circuit, the electro-mechanical constant of piezoelectric transducer, the capacitance of piezoelectric transducer, and the tunable inductance. The piezoelectric transducers on the top and bottom of the host medium are identical. The instantaneous charges on the two transducers are thus equal to each other, i.e., $Q_1(t)=Q_2(t)$. The mass, stiffness, and electro-mechanical coupling constant are wavenumber-dependent,

$$M=\frac{2\sin\left(\frac{nk_{\Gamma X}l_b}{2}\right)}{nk_{\Gamma X}l_b}\rho_b t_b w_b l_b+16\rho_p t_p\frac{\pi r^2\cos(nk_{\Gamma X}r)}{\pi^2-4n^2k_{\Gamma X}^2r^2},$$

$$K=E_b w_b\frac{t_b^3}{6}n^3k_{\Gamma X}^3\sin\left(\frac{nk_{\Gamma X}l_b}{2}\right)+16E_p\left(\frac{t_b^2t_p}{4}+\frac{t_bt_p^2}{2}+\frac{t_p^3}{3}\right)\frac{n^4k_{\Gamma X}^4\pi r^2\cos(nk_{\Gamma X}r)}{\pi^2-4n^2k_{\Gamma X}^2r^2} \tag{3-3a-c}$$

$$k_1=-4h_{31}t_p(t_b+t_p)\frac{n^2k_{\Gamma X}^2\cos(nk_{\Gamma X}r)}{\pi^2-4n^2k_{\Gamma X}^2r^2}$$

where r, l_b, w_b, t_p, t_b, h_{31}, ρ_p and ρ_b represent, respectively, the radius of the piezoelectric transducer, the length of the unit-cell substrate, the width of the substrate, the thickness of the piezoelectric transducer, the thickness of the substrate, the piezoelectric constant of the transducer, and the mass density of the transducer and that of the substrate. The capacitance of one piezoelectric transducer is

$$C=\frac{\pi r^2}{\beta_{33}t_p} \tag{3-4}$$

where β_{33} is the dielectric constant. Equations (3-2a) and (3-2b) illustrate the dynamic interaction between the mechanical and electrical domains. The LC resonance (Equation (3-2b)) affects the substrate dynamics (Equation (3-2a)) owing to the electro-mechanical coupling, thereby influencing the wave

propagation characteristics through changing the wave velocity and creating a bandgap.

We aim at taking advantages of the wave velocity shifting in the vicinity of the local resonance. The phase velocity of an acoustic wave is proportional to its frequency and inversely proportional to its wavenumber. Assume harmonic responses of unit-cell mechanical displacement and charges (on the transducers). The wavenumber with respect to the wave frequency can be solved from the dispersion equation. The dispersion equation of the unit-cell (under un-damped condition) can be obtained from Equations (3-2a) and (3-2b) as

$$\left(-\omega^2 M + K\right)\left(-2\omega^2 L + 1/C\right) - 2k_1^2 = 0 \tag{3-5}$$

It is important to note that, as shown in Equations (2a-c), M, K, and k_1 are all wavenumber-dependent. The wavenumber can thus be directly solved from Equation (3-5). As L is included in this fourth-order equation, the wavenumber $k_{\Gamma X}$ is an explicit function of the external inductance L. The inductance can be tuned online. Therefore, the bandgap features here have the advantage of being tunable and adaptive. Our basic idea here is that acoustic wave at one frequency can be steered by adjusting the inductance in the piezoelectric circuit. We rewrite the phase velocity v_p as a function of inductance L,

$$v_p(L) = \frac{\omega}{k_{\Gamma X}(L)} \tag{3-6}$$

Indeed, the relation of the incidence angle and the refraction angle follows the Snell's Law,

$$\theta_2 = \arcsin\left(\frac{v_p(L)}{v_0}\sin\theta_1\right) \tag{3-7}$$

where v_0 is the reference phase velocity of the harmonic transverse wave in the homogenous aluminum medium, and θ_1 and θ_2 are the angles of incidence and refraction, respectively. In our analysis, the phase velocity v_0 in the plate and the incidence angle θ_1 are given constants. On the other hand, the phase velocity in the prism, v_p, can be adjusted owing to the adaptiveness of local resonance. In such a case,

the acoustic wave travelling through the prism will have difference refraction angles by inductance tuning (Equation 3-6). Recall Equation (3-6). As the inductance in the shunt circuit is continuously adjusted, the phase velocity of the acoustic wave can be continuously tuned. This yields continuous beam steering, since the local resonance of the LC shunt circuit depends on the inductance value. One can easily change the frequency of the LC resonance without altering the mechanical part of the prism.

3.2.3 Case study and discussion

For the case study, we consider a unit-cell consisting of an aluminum substrate (unit-cell size 25.38×25.38×3.13 mm^3) and two piezoelectric discs (radius 10.5 mm and thickness 1 mm) bonded onto the top and bottom surfaces of the substrate. The acoustic prism consists of 13×13 unit-cells that are arranged as isosceles right triangle (total 91 unit-cells) where 6 to 10 layers of unit-cells are effectively involved in beam steering, as shown in Figure 3-1.

We first demonstrate the inductance-dependent features of the dispersion curve as well as the phase velocity of the acoustic wave. In the following analytical and numerical analyses, the material parameters are chosen as: piezoelectric mass density $\rho_p = 7500$ kg/m^3, piezoelectric Young's modulus $E_p = 106$ GPa, piezoelectric constant $h_{31} = -1.37\times10^9$ N/C, dielectric constant $\beta_{33} = 2.92\times10^8$ Vm/C, host medium mass density $\rho_b = 2700$ kg/m^3, and host medium Young's modulus $E_b = 62$ GPa. The piezoelectric material constants are from PZT-5H transducer. Without loss of generality, we choose inductance value L_0 to create a local resonance at 19.46 kHz. The corresponding inductance value is $L_0 = 18.3$ mH. Figures 3-2(a) and 3-2(b) show the dispersion curves and phase velocity curves, respectively. In Figure 3-2(a), $k = k_{\Gamma X} l_b / \pi$ is the normalized wavenumber.

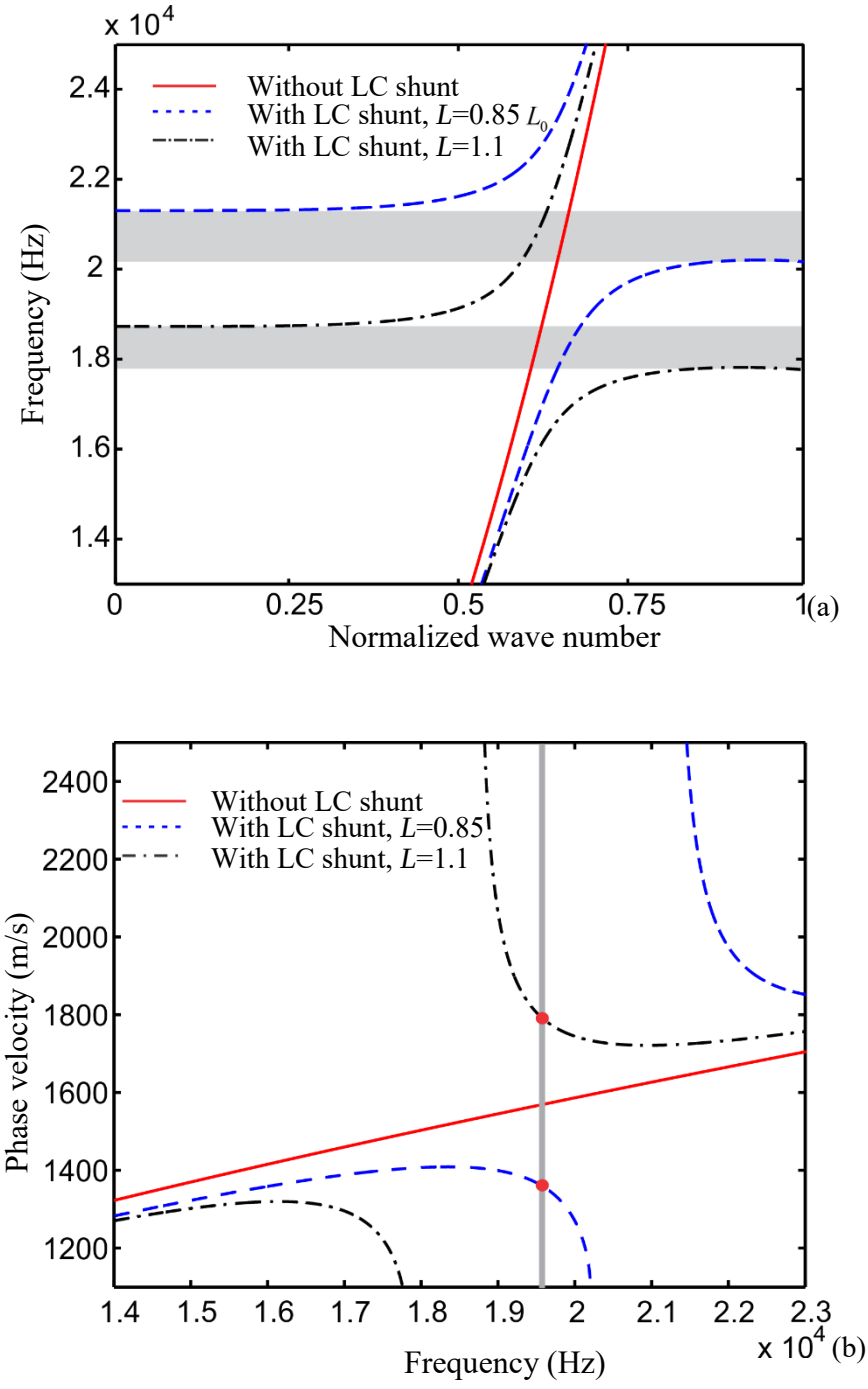

Figure 3-2. (a) Dispersion curve of a unit-cell; (b) Phase velocity of acoustic wave.

It can be observed in Figure 3-2(a) that the LC circuit induces a bandgap around the LC resonant frequency. The frequency of the bandgap decreases with the increase of L. As shown in Figure 3-2(b), the phase velocity of the acoustic wave shifts significantly at a single frequency as bandgaps are adjusted

through tuning L. For example, the phase velocity of the acoustic wave at 19.46 kHz is increased by increasing L. Note that a different phase velocity of the acoustic wave yields different refraction index. The shifting of phase velocity results in a change of the refraction angle, i.e., yielding the beam steering effect.

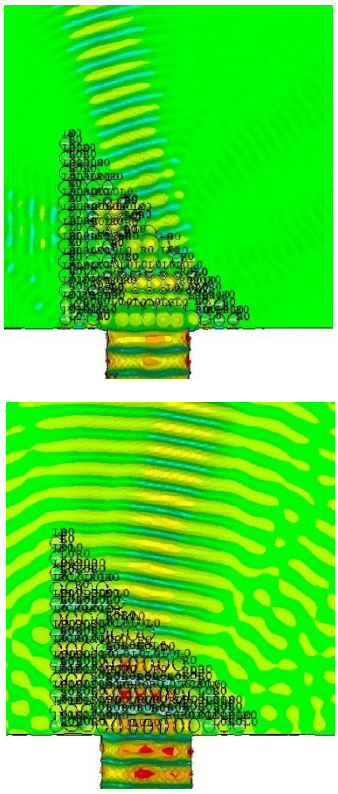

Figure 3-3. Illustration of beam steering effect at 19.64 kHz. (a) $L = 0.9L_0$; (b) $L = 1.06L_0$.

We then demonstrate the continuous wave steering through simulations. Finite element method is employed, as it can match well with respect to experimental studies in piezoelectric metamaterial investigations. We apply ANSYS 14.5 to simulate the beam steering effects under harmonic analysis using the sparse solver. Solid95 element is used to model the substrate, and Solid226 element is used to model the piezoelectric transducers. Displacement contours with different inductance values are shown in Figures 3-3(a) and 3-3(b). Without loss of generality, we choose the frequency of the acoustic wave as 19.46 kHz to illustrate the effectiveness of the prism. In such a case the acoustic wave in the unit-cell has

a fundamental wavelength of 74.4 mm and fundamental wavenumber of 0.0134 mm^{-1} at 19.46 kHz.

In Figures 3-3(a) and 3-3(b), the incident waves propagate from the bottom of the prism, and the results clearly illustrate the wave steering effect at the selected frequency. A nearly planar wave is formed as the forward propagation waves travel through the prism region. It can be observed that when the inductance is decreased to $0.9L_0$, the harmonic acoustic wave propagates to the left-hand side. As the inductance is increased to $1.06L_0$, the harmonic acoustic wave propagates toward the right-hand side. This indicates that the phase velocity of the acoustic wave is shifted dramatically. Continuously tunable beam steering can be achieved at the selected frequency by simply adjusting the shunt circuit inductance. It is worth emphasizing that the system parameters, e.g., the dimension of the unit-cell and the frequency of the acoustic wave, generally remain unchanged. This is the distinctive feature as compared with previous beam steering investigations.

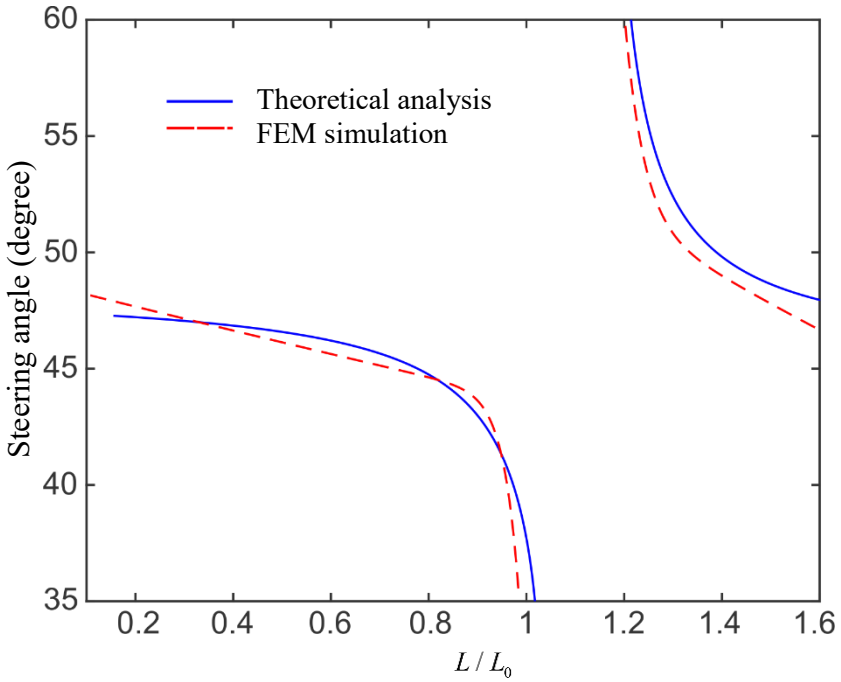

Figure 3-4. Steering angle versus inductance.

The relation of external inductive load and the steering angle is plotted in Figure 3-4. The results are

obtained under the steady-state condition. The incidence angle is 45 degrees. The inductance is tuned from $0.1L_0$ to $1.6L_0$ with step increment of $0.0075L_0$. The refraction angles θ_2 are calculated and presented in Figure 4. The theoretical result predicted by Equation (3-7) is also plotted in Figure 3-4 which shows good agreement with the finite element result. It can be observed that the refraction angle decreases as we increase L. The minimum refraction angle here is 35 degrees. As the inductance approaches L_0, a conventional bandgap of piezoelectric metamaterial is induced. Within the bandgap, the harmonic acoustic wave cannot propagate through the prism area. The bandgap is unavoidable, because only negative equivalent mass can be achieved here. Further increasing the inductance yields another branch of beam steering effect. That is, increasing the inductance can decrease the refraction angle from 65 to 47 degrees. The reason is that the phase velocity of the harmonic wave, as shown in Figure 3-2(b), is decreased to the minimum and then jumps to the maximum value as the inductance is increased in the vicinity of the bandgap. It is worth mentioning that due to the adaptiveness of the LC shunt circuit, the beam steering effect is applicable for acoustic wave at other frequencies.

3.3 Piezoelectric Acoustic GRIN Lens for Wave Focusing

3.3.1 Concept of piezoelectric GRIN lens

Note that the piezoelectric metamaterial with LC shunt circuit has the capacity of wave guiding. In this research, we demonstrate that piezoelectric metamaterial can be designed to have features of adaptive wave focusing. A unit-cell of the piezoelectric metamaterial is shown in Figure 3-5(a).

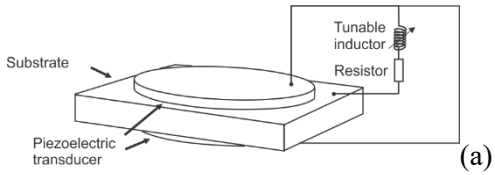

(a)

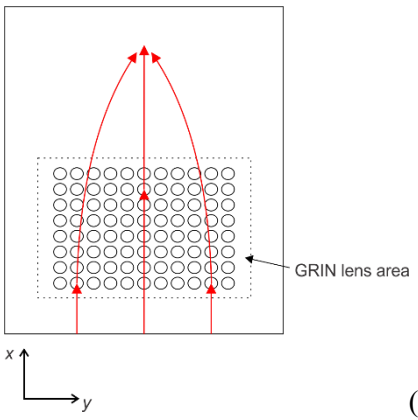

(b)

Figure 3-5. Illustration of GRIN lens. (a) configuration of a unit-cell; (b) prototype of the GRIN lens.

The unitcell consists of two piezoelectric discs bonded onto a host medium. An inductor is connected to the two transducers in parallel. The inductor can be realized by utilizing op-amp circuit (Wang and Tang, 2008). This type of synthetic inductor is adaptive and tunable online. Note that the piezoelectric transducer acts electrically as a capacitor. The combination of the piezoelectric capacitance and the inductive shunt circuit creates a local LC resonant unit. It's demonstrated previously that the piezoelectric metamaterial with LC shunt circuit experience significantly wave velocity shifting in the vicinity of the bandgap (Xu and Tang, 2016). Our hypothesis here is that such a velocity shifting facilities the modification of refraction index of the piezoelectric metamaterial. In this regard, the piezoelectric metamaterial with LC shunt circuit is capable to be arranged into a GRIN lens for adaptive acoustic wave focusing.

The configuration of the piezoelectric GRIN lens is shown in Figure 3-5(b). It is formed by piezoelectric transducer array with individual LC shunt circuit. Specifically, the unitcells of the piezoelectric metamaterial are arranged in rectangular array. Our hypothesis here is that the equivalent refraction index of the GRIN lens following a specific relation that facilities acoustic wave focusing. For a regular gradient index (GRIN) lens, the refraction index of GRIN medium along y-direction has the following relation (Eturk 2016)

$$n(y) = n_0 \operatorname{sech}(\alpha y) \tag{3-8}$$

where α is the coefficient of gradient. The coefficient α determines the location of focusing point of the acoustic wave. Note that all unit-cells of the piezoelectric metamaterial are geometrically identical, i.e., the gradient index of the refraction are achieved by adjusting the distribution of the LC shunt circuit of each unitcell. Therefore, the key challenge here is to obtain the coefficient of the LC shunt circuit of each unitcell. It's worth mentioning that the piezoelectric metamaterial with LC shunt circuit has significantly wave velocity shifting in the vicinity of the bandgap. Moreover, the refraction index is proportional to the wave velocity. Here the refraction index distribution following Equation (3-8) can be achieved by proper design through the calculation of the wave velocity near the bandgap. Additionally, the piezoelectric metamaterial has unique feature of adaptiveness. A local resonance typed bandgap could be realized at an arbitrary frequency point. In other words, the wave velocity shifting can be obtained at a selected frequency point. In this regard, gradient index of the metamaterial is achievable at any frequency by using the piezoelectric metamaterial.

3.3.2 Modeling of unit-cell

In this section, we build a mathematical of a unit-cell of the piezoelectric metamaterial. The dispersion relation can be solved and the relation of the refraction index and wavenumber can be obtained. Consider that the refraction would be adjusted by the modification of the inductance in the shunt circuit. The relation of the refraction index and the inductance is then obtained.

We focus on harmonic transverse wave. Consider a transverse wave propagating in the ΓX direction through the area integrated with the prism. The acoustic wave is predominately propagating in *x*-direction. Therefore, it's reasonable to simplify the unit-cell into two-dimensional metamaterial and use the velocity in *x*-direction to representing the associated relations. A two-dimensional model of the piezoelectric metamaterial can be found in the reference (Xu and Tang, 2016). The following

mathematical modeling utilize the extended Hamilton's principle and the linear constitutive relation of the piezoelectric transducer. Additionally, we consider one unit-cell and employ the Bloch-Floquet theory, i.e., assuming that the mechanical displacement and the electrical displacement both have the following representations (Collet et al, 2012; Pai et al, 2014),

$$w(x,t)=\bar{q}e^{i(k_{\Gamma X}x-\omega t)}, \qquad D(x,t)=\bar{D}e^{i(k_{\Gamma X}x-\omega t)} \tag{3-9a, b}$$

where $k_{\Gamma X}$ is the wave number in the ΓX direction, ω is its frequency, and $\bar{q}$ and $\bar{D}$ are, respectively, the amplitudes of mechanical and electrical displacements. We further let $\bar{D}_1$ and $\bar{D}_2$ denote respectively the electrical displacements of the top and bottom transducers. Essentially, these displacement representations reflect that wave propagates in the spatially periodic piezoelectric metamaterial that is spatially periodic. We now investigate the effect of the circuitry dynamics to unit-cell behavior. Without loss of generality, we analyze the piezoelectric unit-cell where the transducers are connected to the inductive shunt in the parallel manner, as shown in Figure 3-5(a). In order to derive the governing equations of the integrated system, we first examine the electrical dynamics of the unit-cell. The electrodes bracketing the piezoelectric transducers cover fully the top and the bottom surfaces of each transducer. The electrode layers are connected to an inductive circuit/load. The only cause of mechanical strain is assumed to be the axial strain due to bending wave. We can obtain the governing equations of the unit-cell as

$$m\ddot{q}+c\dot{q}+kq+k_1(Q_1+Q_2)=0 \tag{3-10a}$$

$$L(\ddot{Q}_1+\ddot{Q}_2)+R(\dot{Q}_1+\dot{Q}_2)+1/C\cdot Q_1+k_1 q=0 \tag{3-10b}$$

where m is the mass, k is the stiffness, c is the damping coefficient, R is the resistance load in the shunt circuit, q is the mechanical displacement, i.e., $q=\bar{q}e^{-i\omega t}$, Q_1 and Q_2 are the charges on the transducers on the top and bottom of the substrate respectively, i.e., $Q_1=(b_p l_p)\bar{D}_1 e^{-i\omega t}$ and $Q_2=(b_p l_p)\bar{D}_2 e^{-i\omega t}$, L is the inductance value adopted under the parallel-connection configuration, C is the capacitance of one

piezoelectric transducer, k_1 is the electro-mechanical parameter between a transducer and the host beam substrate. Specifically, we have (Xu and Tang, 2016)

$$m = \frac{2\sin(\frac{nk_{\Gamma X}l_b}{2})}{nk_{\Gamma X}l_b}\rho_b t_b w_b l_b + 16\rho_p t_p \frac{\pi r^2 \cos(nk_{\Gamma X}r)}{\pi^2 - 4n^2k_{\Gamma X}^2 r^2},$$

$$k = E_b w_b \frac{t_b^3}{6} n^3 k_{\Gamma X}^3 \sin(\frac{nk_{\Gamma X}l_b}{2}) + 16E_p\left(\frac{t_b^2 t_p}{4} + \frac{t_b t_p^2}{2} + \frac{t_p^3}{3}\right)\frac{n^4 k_{\Gamma X}^4 \pi r^2 \cos(nk_{\Gamma X}r)}{\pi^2 - 4n^2k_{\Gamma X}^2 r^2} \qquad \text{(3-11a-d)}$$

$$k_1 = -4h_{31}t_p(t_b + t_p)\frac{n^2k_{\Gamma X}^2\cos(nk_{\Gamma X}r)}{\pi^2 - 4n^2k_{\Gamma X}^2 r^2}, \quad C = \frac{\pi r^2}{\beta_{33}t_p}.$$

where r, l_b, w_b, t_p, t_b, ρ_p and ρ_b represent, respectively, the radius of the piezoelectric transducer the length of the unit-cell substrate, the width of the substrate, the thickness of the piezoelectric transducer, the thickness of the substrate, and the mass density of the transducer and that of the substrate, respectively. Equations (3−10a) and (3−10b) illustrate the dynamic interaction between the mechanical and electrical domains. The LC resonance (Equation (3−10b)) affects the substrate dynamics (Equation (3-10a)) owing to the electro-mechanical coupling, thereby influencing the wave propagation characteristics through changing the wave velocity and creating a bandgap. Here the equivalent mass, stiffness, and electro-mechanical constant are expressed as explicit functions of wavenumber and geometry/material properties. Indeed, in piezoelectric metamaterial, wave propagates along the continuous beam substrate. The wavenumber indicates the number of waveform cycles per unit length, which decides the corresponding local beam deformation and strain/stress distributions within the unit-cell. Therefore, the equivalent mass, stiffness, and electro-mechanical constant are all wavenumber-dependent.

3.3.3 Gradient refraction index analysis

In this parallel-connection, as the piezoelectric transducers attached onto the top and bottom surfaces

of the host substrate are identical, the instantaneous charges on the two transducers are equal to each other, i.e., $Q_1(t) = Q_2(t)$. To evaluate the unit-cell dynamic characteristics, we assume harmonic responses with frequency ω, i.e.,

$$q_\alpha(t) = q_{\alpha 0} e^{i(-\omega t + \phi_1)}, \quad Q_1(t) = Q_0 e^{i(-\omega t + \phi_2)}, \quad Q_2(t) = Q_0 e^{i(-\omega t + \phi_3)} \tag{3-12}$$

where ϕ_1, ϕ_2 and ϕ_3 are the phases. Substitute Equation (3-12) into Equation (3-10). For a two-DOF (degree-of-freedom) unit-cell governed by Equations (3-10a) and (3-10b), the dispersion equation under the undamped condition can be derived as

$$\left(-\omega^2 m + k\right)\left(-2\omega^2 L + 1/C\right) - 2k_1^2 = 0 \tag{3-13}$$

The solutions to the dispersion equation can be easily obtained as

$$\omega_L = \frac{\sqrt{2}}{2}\sqrt{\frac{E_b w_b \frac{t_b^3}{6} n^3 k_{\Gamma X}^3 \sin(\frac{n k_{\Gamma X} l_b}{2}) + 16 E_p \left(\frac{t_b^2 t_p}{4} + \frac{t_b t_p^2}{2} + \frac{t_p^3}{3}\right) \frac{n^4 k_{\Gamma X}^4 \pi r^2 \cos(n k_{\Gamma X} r)}{\pi^2 - 4n^2 k_{\Gamma X}^2 r^2}}{\frac{2\sin(\frac{n k_{\Gamma X} l_b}{2})}{n k_{\Gamma X} l_b} \rho_b t_b w_b l_b + 16 \rho_p t_p \frac{\pi r^2 \cos(n k_{\Gamma X} r)}{\pi^2 - 4n^2 k_{\Gamma X}^2 r^2}} + \frac{1}{LC}} - \sqrt{\left(\frac{E_b w_b \frac{t_b^3}{6} n^3 k_{\Gamma X}^3 \sin(\frac{n k_{\Gamma X} l_b}{2}) + 16 E_p \left(\frac{t_b^2 t_p}{4} + \frac{t_b t_p^2}{2} + \frac{t_p^3}{3}\right) \frac{n^4 k_{\Gamma X}^4 \pi r^2 \cos(n k_{\Gamma X} r)}{\pi^2 - 4n^2 k_{\Gamma X}^2 r^2}}{\frac{2\sin(\frac{n k_{\Gamma X} l_b}{2})}{n k_{\Gamma X} l_b} \rho_b t_b w_b l_b + 16 \rho_p t_p \frac{\pi r^2 \cos(n k_{\Gamma X} r)}{\pi^2 - 4n^2 k_{\Gamma X}^2 r^2}} - \frac{1}{LC}\right)^2 + 8 \frac{(-4h_{31} t_p (t_b + t_p) \frac{n^2 k_{\Gamma X}^2 \cos(n k_{\Gamma X} r)}{\pi^2 - 4n^2 k_{\Gamma X}^2 r^2})^2}{\frac{2\sin(\frac{n k_{\Gamma X} l_b}{2})}{n k_{\Gamma X} l_b} \rho_b t_b w_b l_b + 16 \rho_p t_p \frac{\pi r^2 \cos(n k_{\Gamma X} r)}{\pi^2 - 4n^2 k_{\Gamma X}^2 r^2}} \frac{1}{L}} \tag{3-14a}$$

$$\omega_H = \frac{\sqrt{2}}{2}\sqrt{\frac{E_b w_b \frac{t_b^3}{6} n^3 k_{\Gamma X}^3 \sin(\frac{nk_{\Gamma X} l_b}{2}) + 16E_p\left(\frac{t_b^2 t_p}{4} + \frac{t_b t_p^2}{2} + \frac{t_p^3}{3}\right)\frac{n^4 k_{\Gamma X}^4 \pi r^2 \cos(nk_{\Gamma X} r)}{\pi^2 - 4n^2 k_{\Gamma X}^2 r^2}}{\frac{2\sin(\frac{nk_{\Gamma X} l_b}{2})}{nk_{\Gamma X} l_b}\rho_b t_b w_b l_b + 16\rho_p t_p \frac{\pi r^2 \cos(nk_{\Gamma X} r)}{\pi^2 - 4n^2 k_{\Gamma X}^2 r^2}} + \frac{1}{LC}} + \sqrt{(\frac{E_b w_b \frac{t_b^3}{6} n^3 k_{\Gamma X}^3 \sin(\frac{nk_{\Gamma X} l_b}{2}) + 16E_p\left(\frac{t_b^2 t_p}{4} + \frac{t_b t_p^2}{2} + \frac{t_p^3}{3}\right)\frac{n^4 k_{\Gamma X}^4 \pi r^2 \cos(nk_{\Gamma X} r)}{\pi^2 - 4n^2 k_{\Gamma X}^2 r^2}}{\frac{2\sin(\frac{nk_{\Gamma X} l_b}{2})}{nk_{\Gamma X} l_b}\rho_b t_b w_b l_b + 16\rho_p t_p \frac{\pi r^2 \cos(nk_{\Gamma X} r)}{\pi^2 - 4n^2 k_{\Gamma X}^2 r^2}} - \frac{1}{LC})^2 + 8\frac{(-4h_{31} t_p (t_b + t_p)\frac{n^2 k_{\Gamma X}^2 \cos(nk_{\Gamma X} r)}{\pi^2 - 4n^2 k_{\Gamma X}^2 r^2})^2}{\frac{2\sin(\frac{nk_{\Gamma X} l_b}{2})}{nk_{\Gamma X} l_b}\rho_b t_b w_b l_b + 16\rho_p t_p \frac{\pi r^2 \cos(nk_{\Gamma X} r)}{\pi^2 - 4n^2 k_{\Gamma X}^2 r^2}}\frac{1}{L}} \quad (3\text{-}14b)$$

where n indicates the nth transverse wave travelling in the metamaterial. The ω_L and ω_H shows the explicit relation of the wavenumber and the frequency of the acoustic wave. It's worth mentioning that the frequency and wavenumber have one to one correspondence. Additionally, there is a region where ω_L or ω_H has no solutions with corresponding wavenumber $k_{\Gamma X}$, which indicates the bandgap of the piezoelectric metamaterial. The velocity of the acoustic wave can then be solved from Equations (3-14a) and (3-14b) by utilizing the following relation

$$v_{\Gamma X} = d\omega / dk_{\Gamma X} \quad (3\text{-}15)$$

As L is included in this fourth-order equation, the wavenumber $k_{\Gamma X}$ is an explicit function of the external inductance L. The inductance is tuned online. Therefore, the velocity of the acoustic wave here has the advantage of being tunable and adaptive. Our basic idea here is that the velocity of the acoustic wave at one frequency can be modified by adjusting the inductance in the piezoelectric circuit. The relation of the refraction index and the wave velocity is then given

$$n = \frac{v_0}{v_{\Gamma X}} = \frac{v_0}{d\omega / dk_{\Gamma X}} \quad (3\text{-}16)$$

where v_0 is the reference velocity in the infinite host plate, ω is the frequency of the acoustic wave,.

Substitute Equation (3-16) into Equation (3-8), the wavenumber $k_{\Gamma X}$ along *y*-direction following the relation

$$d\omega / dk_{\Gamma X}(y) = \frac{v_0}{n_0 \operatorname{sech}(\alpha y)} \tag{3-17}$$

Consider that the wavenumber $k_{\Gamma X}$ is an explicit function of the external inductance *L*, the distribution of the inductance *L* in *y*-direction can be solve from the Equations (3-14) and (3-17).

3.3.4 FEM simulation and discussion

Finite element method (FEM) simulations are carried out to verify the proposed concepts. Finite element method is employed, as it can match well with respect to experimental studies in piezoelectric metamaterial investigations (Thorp et al, 2001; Airoldi and Ruzzene, 2011; Wang et al, 2010; Chen et al, 2012). The unit cell consists of aluminum substrate (size 25.38×25.38×3.13 mm^3) and a piezoelectric transducer (radius 10.5 mm and thickness 1 mm) bonded on its surface. An inductor is connected to the top and bottom surfaces of the piezoelectric transducer as the shunt circuit. The parameters for the materials are: $\rho_p = 7500\ \text{kg/m}^3$, $\rho_b = 2700\ \text{kg/m}^3$, E_b = 62 GPa, and E_p = 106 GPa. The material constants of the piezoelectric transducer, PZT-5H, are $d_{31} = -320\text{pC/N}$ $h_{31} = 5.9\times10^8$ N/C and $\beta_{33} = 2.92\times10^8$ Vm/C. We apply ANSYS 14.5 Academic to simulate the beam steering effects with various inductive loads. We select the frequency of the acoustic wave to be 19.6 kHz. It's worth emphasizing that, the frequency of the acoustic wave can be arbitrary chosen due to the adaptiveness of the piezoelectric metamaterial. Note that the acoustic wave has dramatically velocity shifting in the vicinity of the bandgap, here proper value of the inductance in the shunt circuit is selected that a bandgap is created in the vicinity of the frequency of the acoustic wave. We firstly illustrate the bandgap and velocity behavior of the metamaterial. For one unit-cell of the piezoelectric metamaterial, the dispersion curves and the velocity curves is given

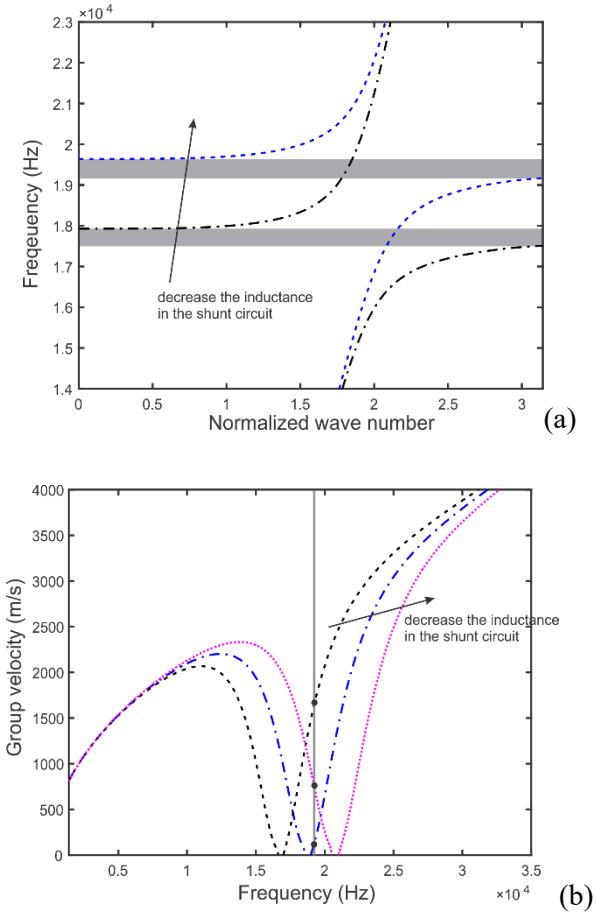

Figure 3-6. Working principle of the piezoelectric GRIN lens. (a) adaptiveness of the bandgap; (b) shifting of the velocity of the acoustic wave at a single frequency.

Figures 3-6(a) and 3-6(b) show the dispersion curves and velocity curves, respectively. It can be observed in Figure 3-6(a) that the LC circuit induces a bandgap around the LC resonant frequency. The frequency of the bandgap decreases with the increase of L. As shown in Figure 3-6(b), the phase velocity of the acoustic wave shifts significantly at a single frequency as bandgaps are adjusted through tuning L. For example, the velocity of the acoustic wave at 19.73 kHz is increased by increasing L. As the inductance in the shunt circuit is continuously adjusted, the velocity of the acoustic wave can be continuously tuned. The key consideration in this research is to obtain the distribution of the inductance in the shunt circuits to achieve the given refraction relation given in Equation (3-8). Here we chosen the

coefficient of gradient to be 6 mm^{-1}. The distribution of the refraction index is then plot in Figure 3-7(a). Correspondingly, the acoustic wave velocity within the GRIN lens has a distribution as shown in Figure 3-7(b).

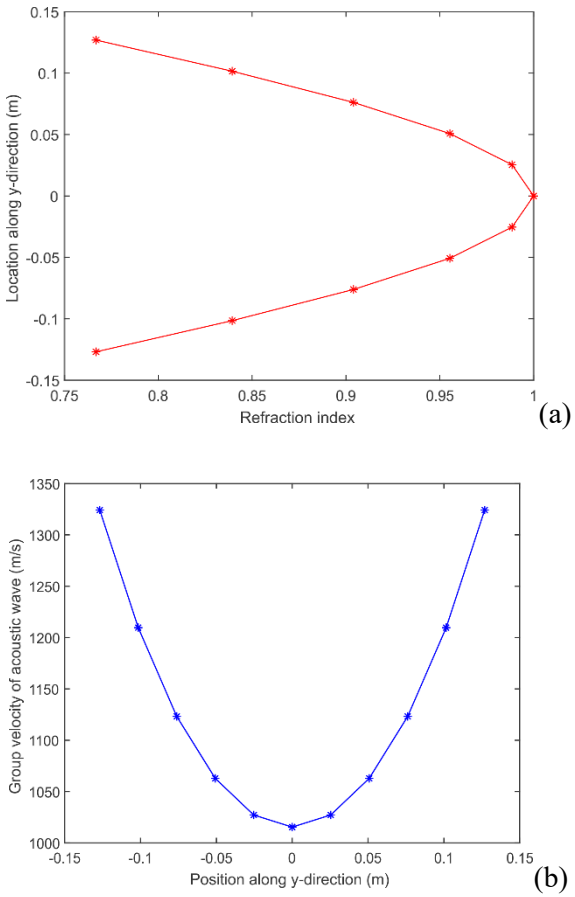

Figure 3-7. (a)relation of the refraction index and the location in y-direction; (b) relation of the wave velocity and the location in y-direction.

It can be observed from Figure 3-7(b) that the velocity of the acoustic wave is increasing with the bias from y-axial. It indicates that the acoustic wave at the upper and lower boundaries travels faster than that in the y-axial. In this regard, the acoustic wave is focusing to one point after pass the GRIN lens area. In this research, the refraction index is modified though shifting the inductance in the shunt circuit. By utilizing the theoretical modeling of the unit-cell, we can easily solve the distribution of the value of

inductance in the shunt circuit, as shown in Figure 3-7.

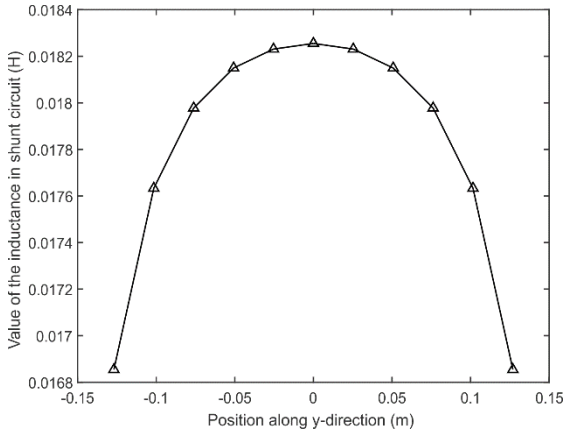

Figure 3-8. The distribution of the inductance load in the shunt circuit.

Figure 3-8 illustrate the relation of the inductance load in the shunt circuit with respect to the location in *y*-direction. The unit-cell in each x-direction line has the same value of individually connected inductor. It can be observed that, the inductor has a gradient change with respected to the shifting of the y-direction location. The change of value of the inductance in the shunt circuit yields the shifting of the bandgap behavior and ultimately modifies the acoustic wave velocity in the unit-cell of the piezoelectric metamaterial, as illustrated in Figure 3-6. The modification of the acoustic wave velocity in y-direction following the relation in Equation (3-8) then facilities the acoustic wave focusing effect. The corresponding simulation result is shown in Figure 3-9.

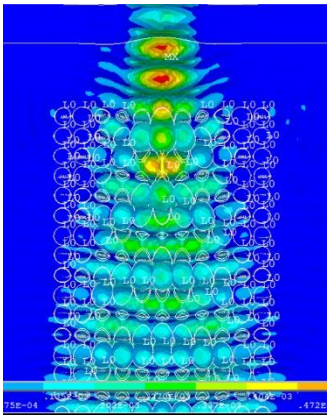

Figure 3-9. The focusing effect of the GRIN lens.

In Figure 3-9, the incident waves propagate from the bottom of the GRIN lens, and the results clearly illustrate the wave focusing effect at the selected frequency. The acoustic wave is focusing on a point in the vicinity of the GRIN lens region. Due to the adaptiveness of the piezoelectric metamaterial, the value of the inductance in the shunt circuit can be modified easily. Consider that the velocity of the acoustic wave and refraction index of the GRIN lens region is hinged upon the value of the inductance. Modification of the inductance can effectively adjust the focusing point of the GRIN lens. It is worth emphasizing that, in such as case, the system parameters, e.g., the dimension of the unit-cell and the frequency of the acoustic wave, generally remain unchanged. This is the new feature as compared with previous beam steering investigations.

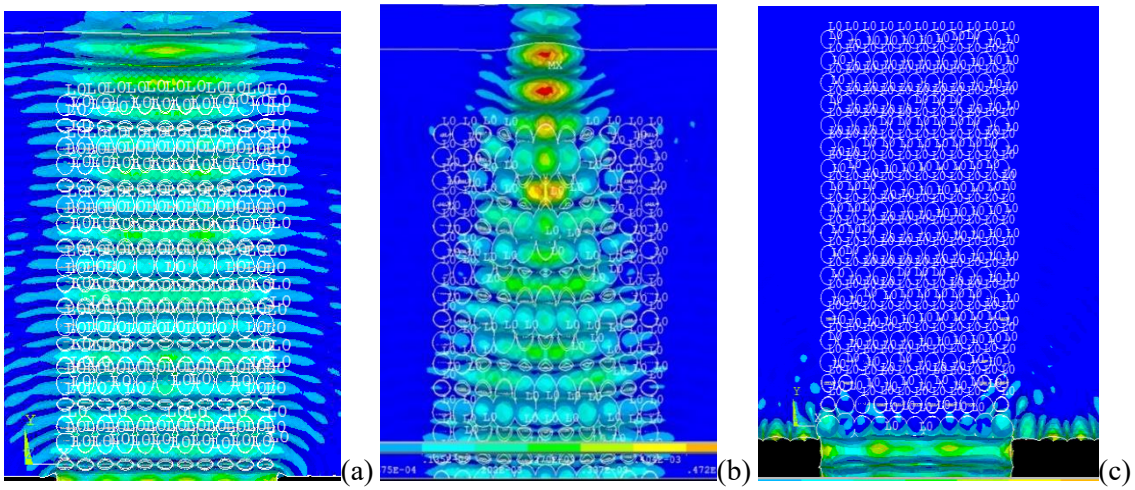

Figure 3-10. The focusing effect of the GRIN lens at different frequencies. (a)19 kHz; (b)19.6 kHz; (c)19.7 kHz

Figure 3-10 illustrates the performance of the GRIN lens under the parameters combination shown in Figure 3-10(a-c), respectively, under 19 kHz, 19.6 kHz and 19.7 kHz. It can be observed that the acoustic wave would not be focused when the frequency of the wave is far from the local resonant frequency of

the LC shunt circuit. While acoustic wave focusing can be achieved in the vicinity of the bandgaps (Figure 6(b)), the bandgaps of the piezoelectric metamaterial is not avoidable. As shown in Figure 3-10(c), a bandgap exists at 19.7 kHz and the acoustic wave cannot propagate through the GRIN lens area.

3.4 Conclusion

In summary, in this section we firstly find that the proposed metamaterial-based prism offers the capability of steering the acoustic wave due to the local resonance from the LC shunt circuit. We analyze and demonstrate the tunable acoustic beam steering by choosing the at a single frequency point of 19.46 kHz. The angle of the wave can be tuned between 30 to 60 degrees by adjusting the inductance. The resonant frequency of the shunt circuit can be modified by changing the inductance. Moreover, the full integration of the adaptive piezoelectric metamaterial, tunable inductors, computing resources, and power systems can form a hybrid metamaterial system where acoustic wave guiding can be remotely controlled. The concept proposed here can be applied to the adaptive GRIN lens for a variety of applications.

Secondly, our research finds that the proposed metamaterial-based GRIN lens offers the capability of focusing the acoustic wave due to the local resonance from the LC shunt circuit. We analyze and demonstrate the acoustic beam focusing by choosing the at a single frequency point of 19.6 kHz. The incident acoustic wave can be clearly focused at a point in the vicinity of the GRIN lens. The resonant frequency of the shunt circuit can be modified by changing the inductance. Moreover, the full integration of the adaptive piezoelectric metamaterial, tunable inductors, computing resources, and power systems can form a hybrid metamaterial system where acoustic wave guiding can be remotely controlled.

Chapter 4 Tailoring Vibration Mode by Finite Phononic Crystal

4.1 Introduction

Metamaterial, defined as artificial structures that exhibit physical properties not available in natural material, has extraordinary capability in low-frequency sound/vibration attenuation, negative refraction, and super lenses (Landy et al, 2008; Pendry and Li, 2008; Yang et al, 2010; Baravelli and Ruzzene, 2013; Yoo et al, 2014). The acoustic metamaterial, consisting of periodically arranged local microstructures or unit-cells integrated to a host medium, can manipulate elastic wave propagation. The local resonance mechanism utilizes the sub-wavelength local resonances induced within a unit-cell. The local resonance can alter the frequency-dependent effective mass densities and/or bulk moduli of the continuum media. In most cases, the internal resonators have highly contrasting elastic properties (Wang et al, 2006). Within the bandgap, the elastic wave cannot propagate, and wave energy is reflected or temporarily stored in resonators and can be adopted for energy harvesting (Huang and Sun, 2010; Tan et al, 2014; Hu et al, 2017a; Hu et al, 2017b).

Recently, metamaterial-based acoustic wave-guiding has received significant attention. Various types of unit-cell microstructures are adopted. For example, a two-dimensional GRIN lens, comprised of cylinders with different diameters or unit-cells with cross-shaped apertures, is proposed (Climente et al, 2010). Wave-guiding systems have seen applications in fault detection and energy harvesting. By utilizing local resonance, a two-dimensional planar array can focus acoustic waves for enhanced fault detection sensitivity (Yan et al, 2013). Notably, piezoelectric metamaterial has recently emerged as a new option in acoustic wave guiding. For instance, piezoelectric transducers are assembled in rectangular array to generate strong, frequency-dependent directional beaming (Senesi et al, 2010). A spiral-shaped transducer is proposed for frequency-based beam steering and applied to enhanced directional sensing (Baravelli et al, 2013). By taking advantage of multiple embedded acoustic metamaterial lenses, directional acoustic wave guiding is also achieved at corresponding frequencies (Zhu and Semperlotti, 2014). Although promising, these systems share one common limitation that they cannot arbitrarily

manipulate acoustic wave under a given frequency as the layout/geometry to facilitate wave-guiding is fixed.

Previously, negative material properties and bandgap characteristics are intensively discussed on local resonance acoustic metamaterials. For example, negative mass is found in mass-in-mass type acoustic metamaterial. Negative Young's modulus is investigated in piezoelectric metamaterial with local LC resonance. The negative effective mass/Young's modulus can generate a bandgap which yield acoustic wave attenuation. Note that ideal periodicity cannot be easily achieved in experiments, serially connected unit-cells are adopted to investigate the bandgap behavior. The bandgap/wave attenuation characteristics is accompanied due to the bandgap behavior at anti-resonance. Specifically, anti-resonance is a pronounced minimum in the amplitude of the host structure within the bandgap. On the other hand, resonances of the finite phononic crystal are usually ignored since they yield large amplitude motion of the host structure. In other words, the resonances yield multiple peaks in the transmission diagram of the metamaterial system.

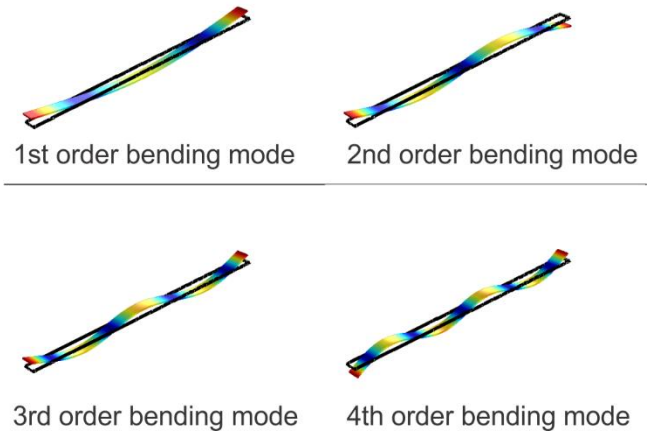

Figure 4-1. The first four bending mode of a uniform beam.

Here we focus on the resonance behavior of a finite metamaterial beam, i.e., the vibration modes. Structure resonances are widely adopted in designing and performance enhancement of actuators, sensors

and energy harvesters. The performance of a resonator is hinged upon its vibration modes. The first four mode shape of a uniform beam with free-free boundary condition is illustrated in Figure 4.1. It can be observed that the mode shapes of a uniform beam show symmetry or anti-symmetry due to the geometry.

Vibration mode tailoring is performed since special vibration pattern is required in applications. In the past, vibration mode modification is usually achieved by geometry tailoring. For example, change the shape of a piezoelectric cantilever into triangle can effectively achieve a vibration mode with uniform strain distribution for enhance energy harvesting. For another example, piezoelectric transducer is etching into the shape of teeth for actuating. Consequent to the geometry tailoring, the strength of the structure might be weakened. Moreover, vibration modes customization in some situations can become tedious or impossible.

4.2 Design Concept and System Analysis

4.2.1 Schematic of design

In this research, we propose that mode shape customization can be realized by combination of resonance and bandgap characteristics of finite photonic crystal. The underlying physics of the concept is shown in Figure 4-2(a). A geometrical uniform metamaterial beam, consisting of two regions with free-free boundary condition, is considered. This metamaterial beam is working at a chosen frequency that region 1 works within the bandgap while region 2 works at resonance. At this frequency, the structure vibration in region 1 is suppressed due to the acoustic wave attenuation effect. At the same time, region 2 works at resonance with proper parameters combination. Here we propose that by the proper arrangement of resonance and anti-resonance regions, unusual vibration mode shape can be created.

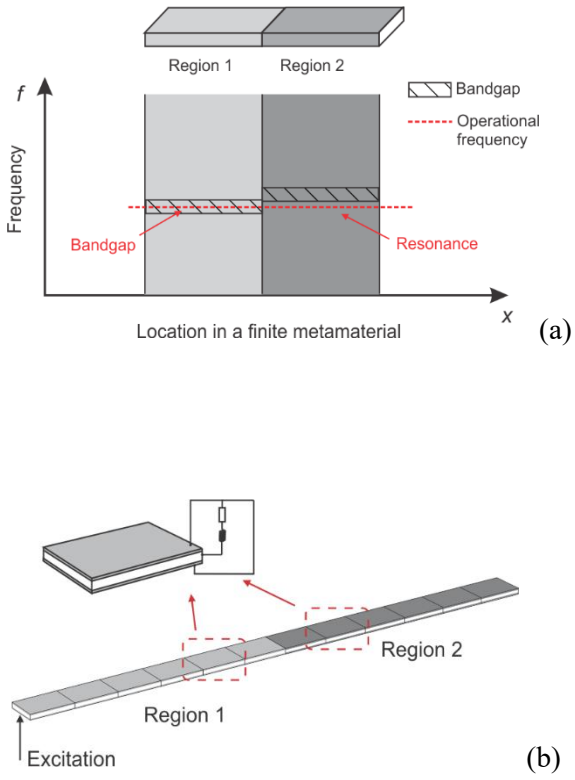

Figure 4-2. Illustration and underlying physics

The prototype is illustrated in Figure 4-2(b). This metamaterial beam consists of geometrical identical piezoelectric unit-cells with LC shunt circuits. Each of the region contains 6 unit-cells. It's worth noticing that, identical piezoelectric unit-cells are adopted for region 1 and 2 to exclude the geometrical influence on vibration modes. The working principle applies to mass-in-mass type and Bragg scattering type metamaterial beam. In the metamaterial beam, a unit-cell consists of piezoelectric transducers bonded on the top and bottom of the host structure. Inductance loads are connected to the piezoelectric transducers in the unit-cell individually. The inductance load is L_1 for unit-cells in region 1 and L_2 for unit-cells in region 2, respectively. A bandgap is created in region 1 by local resonance of the LC shunt circuit. The LC resonance affects the substrate dynamics owing to the electro-mechanical coupling, thereby influencing the wave propagation characteristics through changing the wave velocity

and creating a bandgap. Region 2 of the metamaterial beam is supposed to work at resonance. Note that resonance can be created in a free-free cantilever beam when the length of the beam is integer multiple half wavelength of a stationary acoustic wave. Our hypothesis here is that structure resonance of region 2 can be created by adjusting the wavelength to meet specified conditions. The adjustment can be realized by tuning the inductance load L_2 in the shunt circuit. In this regard, a metamode of the uniform beam can be achieved.

4.2.2 Unit-cell analysis

We focusing on the bending mode of the metamaterial beam. The unit-cell consists of an aluminum substrate (unit-cell size 25×20×2 mm^3) and two piezoelectric transducers (25×20×0.5 mm^3) bonded onto the top and bottom surfaces of the substrate. The material parameters are chosen as: piezoelectric mass density $\rho_p = 7700$ kg/m^3, piezoelectric Young's modulus $E_p = 106$ GPa, piezoelectric constant $d_{31} = -320$ pC/N, dielectric constant $\beta_{33} = 2.92\times10^8$ Vm/C, host medium mass density $\rho_b = 2730$ kg/m^3, and host medium Young's modulus $E_b = 62$ GPa. To elucidate the key characteristic of wave propagation, bandgap behaviors are firstly analyzed with $L_1 = 0.13$ H.

To elucidate the key characteristic of wave propagation, governing equations of the piezoelectric unit-cell are derived. Extended Hamilton's principle is adopted, and the Bloch-Floquet periodic boundary conditions are considered. The piezoelectric transducers generate electric displacement due to mechanical strain, and are considered as voltage sources in electrical domain. For the unit-cell shown in Figure 4-2(b), we have the following lumped-parameter model,

$$\begin{aligned} M\ddot{x} + c\dot{x} + Kx + k_1(Q_1 + Q_2) &= 0 \\ L(\ddot{Q}_1 + \ddot{Q}_2) + R(\dot{Q}_1 + \dot{Q}_2) + (1/C)\cdot Q_1 + k_1 x &= 0 \end{aligned} \tag{4-1a, b}$$

where Q_1, Q_2 and x are charge on the top transducer, charge on the bottom transducer, and lumped displacement of the unit-cell; M, K, c, R, k_1, C and L represent, respectively, the mass, stiffness, mechanical damping coefficient, resistance in the shunt circuit, the electro-mechanical constant of piezoelectric transducer, the capacitance of piezoelectric transducer, and the tunable inductance. The piezoelectric transducers on the top and bottom of the host medium are identical. The instantaneous charges on the two transducers are thus equal, i.e., $Q_1(t) = Q_2(t)$. As shown by Xu et al (2016), the mass, stiffness, and electro-mechanical coupling constant are wavenumber-dependent,

$$m = \frac{2\sin(\frac{k_x l_b}{2})}{k_x l_b}\rho_b h_b b_b l_b + \frac{2\sin(\frac{k_x l_b}{2}\frac{l_p}{l_b})}{k_x l_b} 2\rho_p h_p b_p l_b$$

$$k = 2E_b I_b k_x{}^3 \sin(\frac{k_x l_b}{2}) + 4E_p I_p k_x{}^3 \sin(\frac{k_x l_b}{2}\frac{l_p}{l_b}) \qquad \text{(4-2a-c)}$$

$$k_1 = -2\frac{F_p h_{31} k_x}{b_p l_p}\sin(\frac{k_x l_b}{2}\frac{l_p}{l_b})$$

where r, l_b, w_b, t_p, t_b, ρ_p and ρ_b represent, respectively, the radius of the piezoelectric transducer，the length of the unit-cell substrate, the width of the substrate, the thickness of the piezoelectric transducer, the thickness of the substrate, and the mass density of the transducer and that of the substrate. The capacitance of one piezoelectric transducer is $C = l_b w_b / \beta_{33} t_p$. Equations (4-1a) and (4-1b) illustrate the dynamic interaction between the mechanical and electrical domains. The LC resonance (Equation (4-1b)) affects the substrate dynamics (Equation (4-1a)) owing to the electro-mechanical coupling, thereby influencing the wave propagation characteristics through changing the wave velocity and creating a bandgap.

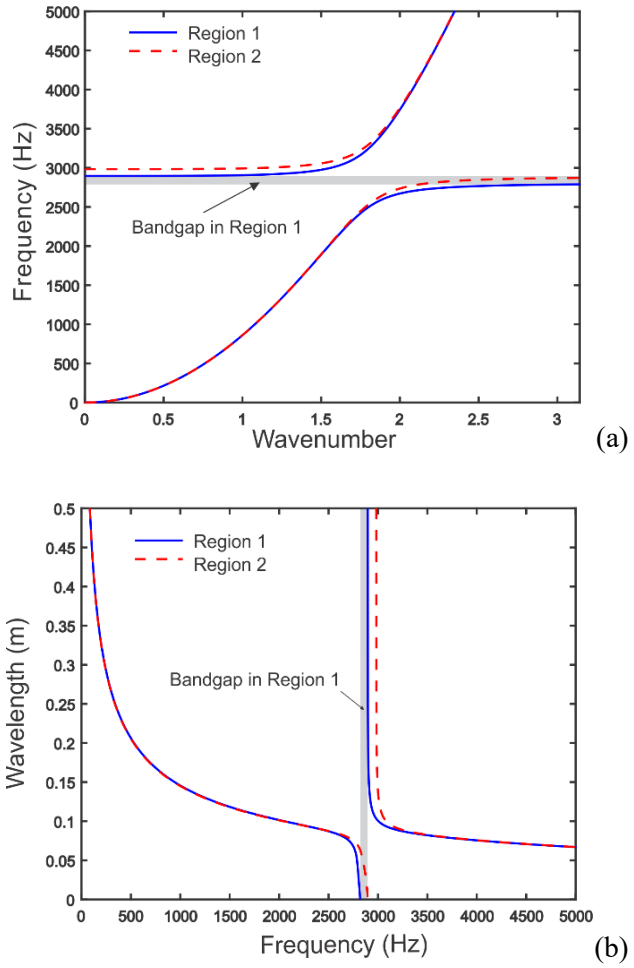

Figure 4-3. Dispersion curves of unit-cells in region 1 and 2.

The dispersion curves of the unit-cells are presented in Figure 4-3(a). It can be observed that, unit-cells in region 1 generates a bandgap at 2986 Hz due to the LC resonance of the shunt circuits. Besides, the dispersion curves in region 2 is shifted with respected to that in region 1. The shifting of dispersion curve enables existence of stationary wave in region 2 while the acoustic wave in region 1 is suspended. In other words, region 2 is potential to have dramatically vibration while the region 1 is kept in stationary state. Figure 4-3(b) shows the wavelength distribution in region 1 and 2 with respected to frequency. One may obtain that the wavelength of stationary wave changes dramatically in the vicinity of the bandgap. As shown in Figure 4-3(b), a bandgap is created in region 1 while associating wavenumber can

be found in the bandgap in region 2. It's also worth mentioning that, the curve of wavelength in region 2 can be adjusted through tuning L_2, e.g., move leftwards or rightwards.

4.2.3 Mode shape analysis

Consider that the boundary condition at the conjunction of region 1 and 2 is complicated. Euler beam theory is adopted to solve the mode shape of the finite metamaterial beam. The governing equation of the metamaterial beam is given

$$\frac{\partial}{\partial x^2}\left[EI(x)\frac{\partial^2 w(x,t)}{\partial x^2}\right]+\frac{\partial}{\partial t}\left[\rho A(x)\frac{\partial w(x,t)}{\partial t}\right]=0 \tag{4-3}$$

where $EI(x)$ is the moment of inertial at location x and $\rho A(x)$ is the density of the beam per unit length. The density of the beam per keeps the same for the section in region 1 and 2. Note that inductive load is connected to the unit-cell, the equivalent Young's Modulus of the piezoelectric metamaterial is given

$$E_i = E_p\left(1-\frac{k_{31}^2}{1+i\omega C_p(R+i\omega L_i)}\right) \tag{4-4}$$

where k_{31} is the coupling coefficient of the piezoelectric material, E_p is the Young's Modulus of the piezoelectric material, C_p is the value of the capacitance of the piezoelectric transducer and i indicates the ith section of the beam. Assume mode method is adopted, the displacement of the metamaterial beam can be rewritten in

$$w_i(x,t)=\phi_i(x)q(t) \tag{4-5}$$

where $\phi_i(x)$ is the assumed mode shape of the metamaterial beam in region 1 and 2, respectively, as

$$\phi_1(x)=A_1\cos\lambda_1 x+B_1\sin\lambda_1 x+C_1\cosh\lambda_1 x+D_1\sinh\lambda_1 x, 0\le x<l_1 \tag{4-6a}$$

$$\phi_2(x)=A_2\cos\lambda_2(x-l_1)+B_2\sin\lambda_2(x-l_1)+C_2\cosh\lambda_2(x-l_1)+D_i\sinh\lambda_2(x-l_1), l_1\le x<l_1+l_2 \tag{4-6b}$$

where A_i, B_i, C_i, D_i are the coefficients of the mode functions and λ_i is the eigenvalue of *i*th section. Boundary conditions are applied at the two free ends and in the conjunction of region 1 and 2. The free boundary conditions at the two free ends are

$$\frac{d^2\phi_1(0)}{dx^2} = 0\,, \qquad \frac{d^3\phi_1(0)}{dx^3} = 0\,,$$

$$\frac{d^2\phi_2(l_2)}{dx^2} = 0\,, \qquad \frac{d^3\phi_2(l_2)}{dx^3} = 0\,. \tag{4-7a-d}$$

Solving the boundary conditions, we obtain:

$$\begin{aligned}\frac{d^2\phi_1(0)}{dx^2} &= -A_1\lambda_1^2\cos 0 - B_1\lambda_1^2\sin 0 + C_1\lambda_1^2\cosh 0 + D_1\lambda_1^2\sinh 0 \\ &= -A_1\lambda_1^2 + C_1\lambda_1^2 = 0\end{aligned} \tag{4-8a}$$

$$\begin{aligned}\frac{d^3\phi_1(x)}{dx^3} &= A_1\lambda_1^3\sin 0 - B_1\lambda_1^3\cos 0 + C_1\lambda_1^3\sinh 0 + D_1\lambda_1^3\cosh 0 \\ &= -B_1\lambda_1^3 + D_1\lambda_1^3 = 0\end{aligned} \tag{4-8b}$$

$$\frac{d^2\phi_2(l_2)}{dx^2} = -A_2\lambda_2^2\cos\lambda_2 l_2 - B_2\lambda_2^2\sin\lambda_2 l_2 + C_2\lambda_2^2\cosh\lambda_2 l_2 + D_2\lambda_2^2\sinh\lambda_2 l_2 = 0 \tag{4-8c}$$

$$\frac{d^3\phi_2(l_2)}{dx^3} = A_2\lambda_2^3\sin\lambda_2 l_2 - B_2\lambda_2^3\cos\lambda_2 l_2 + C_2\lambda_2^3\sinh\lambda_2 l_2 + D_2\lambda_2^3\cosh\lambda_2 l_2 = 0 \tag{4-8d}$$

Besides, the boundary conditions at the conjunction of region 1 and 2 ($x = l_1$) are,

$$
\begin{aligned}
&\phi_1(l_1) = \phi_2(0), \\
&\left.\frac{d\phi_1(x)}{dx}\right|_{x=l_1} = \left.\frac{d\phi_2(x)}{dx}\right|_{x=l_1}, \\
&EI_1 \left.\frac{d^2\phi_1(x)}{dx^2}\right|_{x=l_1} = EI_2 \left.\frac{d^2\phi_2(x)}{dx^2}\right|_{x=l_1}, \\
&EI_1 \left.\frac{d^3\phi_1(x)}{dx^3}\right|_{x=l_1} = EI_2 \left.\frac{d^3\phi_2(x)}{dx^3}\right|_{x=l_1}.
\end{aligned}
\tag{4-9a-d}
$$

The boundary conditions yields,

$$A_1 \cos\lambda_1 l_1 + B_1 \sin\lambda_1 l_1 + C_1 \cosh\lambda_1 l_1 + D_1 \sinh\lambda_1 l_1 = A_2 + C_2 \tag{4-10a}$$

$$-A_1\lambda_1 \sin\lambda_1 l_1 + B_1\lambda_1 \cos\lambda_1 l_1 + C_1\lambda_1 \sinh\lambda_1 l_1 + D_1\lambda_1 \cosh\lambda_1 l_1 = B_2\lambda_2 + D_2\lambda_2 \tag{4-10b}$$

$$EI_1\left(-A_1\lambda_1^2 \cos\lambda_1 l_1 - B_1\lambda_1^2 \sin\lambda_1 l_1 + C_1\lambda_1^2 \cosh\lambda_1 l_1 + D_1\lambda_1^2 \sinh\lambda_1 l_1\right) = EI_2\left(-A_2\lambda_2^2 + C_2\lambda_2^2\right) \tag{4-10c}$$

$$EI_1\left(A_1\lambda_1^3 \sin\lambda_1 l_1 - B_1\lambda_1^3 \cos\lambda_1 l_1 + C_1\lambda_1^3 \sinh\lambda_1 l_1 + D_1\lambda_1^3 \cosh\lambda_1 l_1\right) = EI_2\left(-B_2\lambda_2^3 + D_2\lambda_2^3\right) \tag{4-10d}$$

We can then obtain the eigenvalue problem regarding the coefficients $\mathbf{d} = [A_1 \quad B_1 \quad C_1 \quad D_1 \quad A_2 \quad B_2 \quad C_2 \quad D_2]^{\mathrm{T}}$,

$$K(\lambda_1, \lambda_2)\mathbf{d} = 0 \tag{4-11}$$

where

$$
K(\lambda_1, \lambda_2) = \begin{bmatrix}
1 & 0 & -1 & 0 & 0 & 0 & 0 & 0 \\
0 & 1 & 0 & -1 & 0 & 0 & 0 & 0 \\
\cos\lambda_1 l_1 & \sin\lambda_1 l_1 & \cosh\lambda_1 l_1 & \sinh\lambda_1 l_1 & -1 & 0 & -1 & 0 \\
-\lambda_1 \sin\lambda_1 l_1 & \lambda_1 \cos\lambda_1 l_1 & \lambda_1 \sinh\lambda_1 l_1 & \lambda_1 \cosh\lambda_1 l_1 & 0 & -\lambda_2 & 0 & -\lambda_2 \\
-EI_1\lambda_1^2 \cos\lambda_1 l_1 & -EI_1\lambda_1^2 \sin\lambda_1 l_1 & EI_1\lambda_1^2 \cosh\lambda_1 l_1 & EI_1\lambda_1^2 \sinh\lambda_1 l_1 & EI_2\lambda_2^2 & 0 & -EI_2\lambda_2^2 & 0 \\
EI_1\lambda_1^3 \sin\lambda_1 l_1 & -EI_1\lambda_1^3 \cos\lambda_1 l_1 & EI_1\lambda_1^3 \sinh\lambda_1 l_1 & EI_1\lambda_1^3 \cosh\lambda_1 l_1 & 0 & EI_2\lambda_2^3 & 0 & -EI_2\lambda_2^3 \\
0 & 0 & 0 & 0 & -\lambda_2^2 \cos\lambda_2 l_2 & -\lambda_2^2 \sin\lambda_2 l_2 & \lambda_2^2 \cosh\lambda_2 l_2 & \lambda_2^2 \sinh\lambda_2 l_2 \\
0 & 0 & 0 & 0 & \lambda_2^3 \sin\lambda_2 l_2 & -\lambda_2^3 \cos\lambda_2 l_2 & \lambda_2^3 \sinh\lambda_2 l_2 & \lambda_2^3 \cosh\lambda_2 l_2
\end{bmatrix}
\tag{4-12}
$$

By solving the determinant of K equal to zero, i.e., $|K(\lambda_1, \lambda_2)| = 0$, the eigenvalues of λ_1 and λ_1 for all modes can be obtained. Correspondingly, the mode shapes for the metamaterial beam can be plotted after we obtain the eigenvector $\mathbf{d}$.

4.3 FEM Simulation and Discussion

To illustrate the metamode, case study is carried out by theoretical analysis and Finite element method analysis. An operating frequency is chosen within the bandgap of region 1 as 2885 Hz. As aforementioned, wavelength of the stationary wave in region 2 can be adjusted through tuning L_2. Here we firstly illustrate the vibration modes by theoretical analysis.

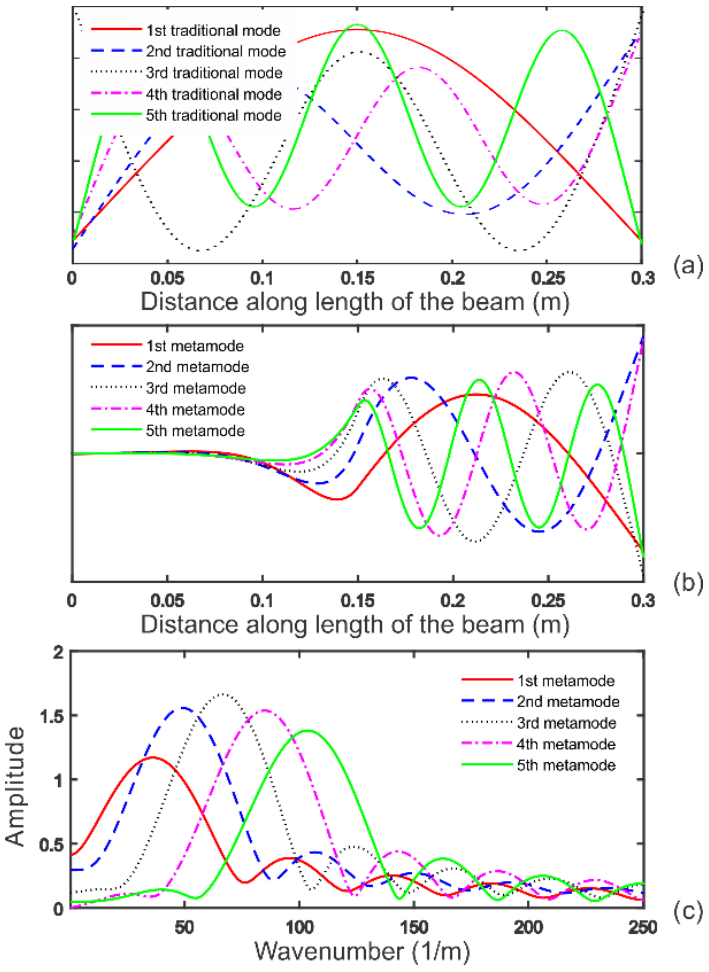

Figure 4-4. Vibration modes of the uniform beam. (a) Traditional vibration modes; (b) Metamodes with various inductive loads in region 2 at 2885 Hz; (c) Wavenumber in region 2.

Figure 4-4 shows the traditional and the metamodes of the uniform beam by theoretical analysis. The vibration modes are obtained by solving the eigenvector problem in undamped condition. The traditional symmetrical vibration modes can be found at resonant frequencies of 842.67, 2322.84, 4553.71 and 7527.51 Hz, respectively. The metamodes are created at the chosen frequency by adjusting the value of L_2, i.e., 2885 Hz. It can be observed that, though the beam is geometrical uniform, un-symmetrical vibration mode can be obtained that region 1 is in stationary state. While the traditional vibration modes are symmetrical, the metamodes enable the finite metamaterial beam has structural vibration concentration in region 2. Here we present the first four metamodes of the metamaterial beam. Wavenumbers of region 2 are calculated for each of the modes, respectively, as shown in Fig. 3(c). In these vibration modes, stationary acoustic waves in region 2 have wavenumber of 36.19, 49.01, 66.61 and 84.72 1/m, respectively, i.e., the adjacent vibration modes have difference approximating half wavelength. It's worth emphasizing that, the vibration modes are steady-state responses with wave attenuation in region 1 and amplification in region 2. In contrast to transit response, the mechanical energy of the stationary wave is accumulated in region 2 due to the resonating effect.

With special interest is the selection of the operating frequency. One key consideration is that the frequency should be chosen within the bandgap of the unit-cell in region 1. Note that the bandgap of the unit-cell in region 1 stays for a frequency range, case studies are presented

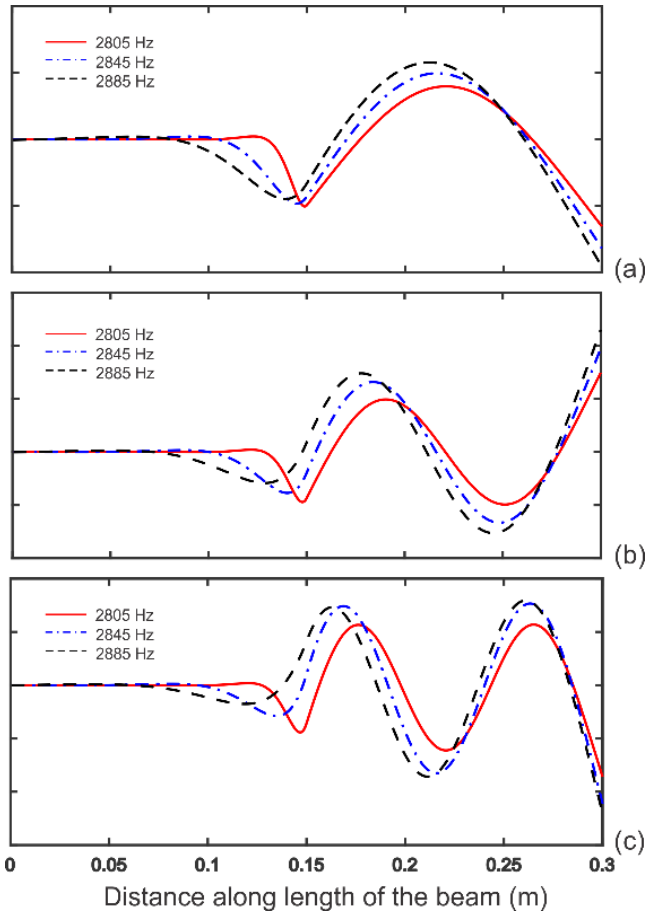

Figure 4-5. Comparison of metamodes at different operating frequencies. (a) 1st mode; (2) 2nd mode; (3) 3rd mode.

In Figure 4-5, the influence of frequency selection is illustrated. Multiple operating frequencies are chosen in the bandgap of unit-cells in region 1 as 2805, 2845 and 2885 Hz. For simplicity and without loss of generality, the first three order vibration modes are calculated and compared. It can be clearly observed that, metamode is effectively created for the three chosen frequencies. Moreover, the location of operating frequency affects the shape of the metamode. For example, the mode at 2805 Hz has a much flatter region 1 than the one at 2885 Hz. This phenomenon can be attributed to the fact that unit-cells in region 1 may have better wave attenuation effect in the middle of the bandgap. Note that the bandgap of a piezoelectric metamaterial features adaptiveness by adjusting the inductive load in the shunt circuit, the

chosen of operating frequency is quite flexible. It's worth emphasizing that the creation and adjustment of the metamode do not require mechanical tailoring of the beam. In other words, we can create these vibration modes without reduce the strength or durability of the mechanical component.

It's also noticeable that the vibration modes, unlike transit response under propagating wave, are independent of the location of excitations. In other words, z-direction excitations applied at an arbitrary location would induce the same vibration pattern. Here we consider an extreme case that exciting force is applied at the left end of the metamaterial beam. The forced response of the metamaterial beam is simulated versus the inductive load L_2. As the FEM analysis can match well with respect to experimental studies in piezoelectric metamaterial investigations, we apply COMSOL 5.2 to simulate the vibration mode and force response of the metamaterial beam with various inductive loads L_2 in region 2.

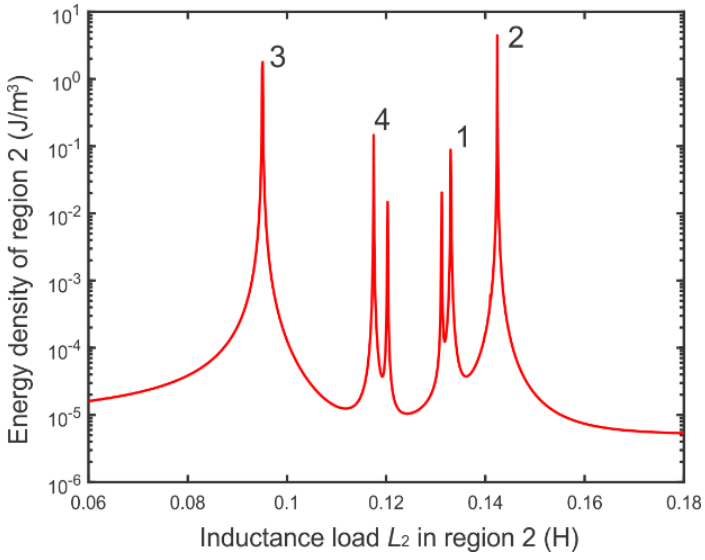

(a)

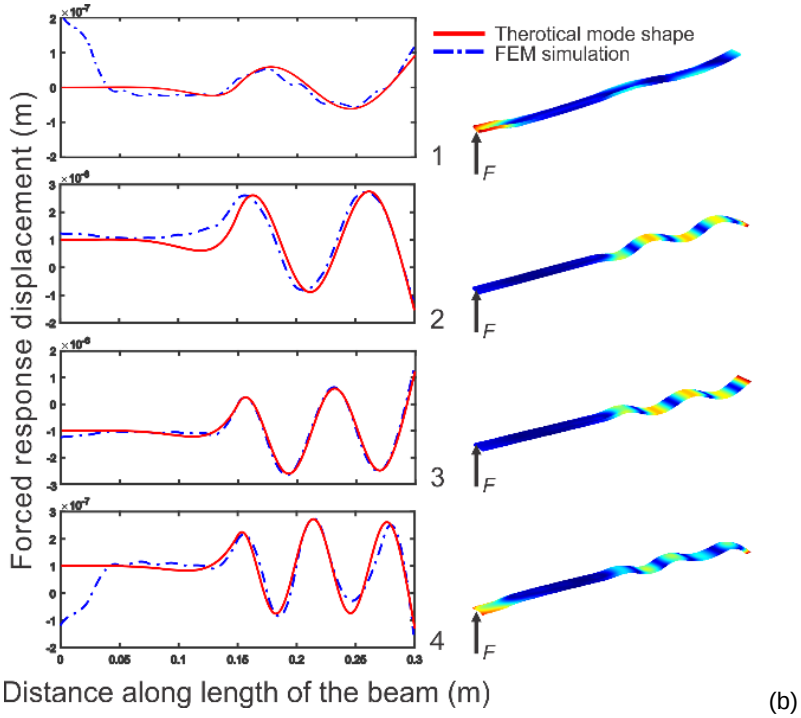

Figure 4-6. Forced responses. (a) Response by sweeping inductor L_2 at 2885 Hz; (b) Displacement responses at the marked peaks.

Figure 4-6 presents the mechanical energy density stored in region 2 versus the inductive load. The results are obtained at 2885 Hz with excitation applied at the left end of the metamaterial beam. For a typical piezoelectric metamaterial, mechanical energy stored in region 2 should have minimum value due to the existence of bandgap in region 1. However, multiple peaks can be observed due to the structure resonances. The peaks are induced by resonance motions associating the 2nd, 3rd, 4th and 5th metamodes. Specifically, the resonant motion accumulates and amplify the mechanical energy travelling through region 1. These vibration modes that region 1 works in stationary state while region 2 has significantly displacement. The phenomenon confirm that the uniform beam can be effective excited while the region with force applied is in steady-state. It's worth emphasizing that the metamaterial beam is flexible that one can also adjusting the vibration modes, e.g., the vibration pattern and strain distribution. Results from FEM simulation agree well with theoretical analysis. Here the metamaterial

beam with two regions is adopted for illustration. This concept can be extended in to metamaterial beam with multiple regions and resonances assignment. For example, a beam with three regions and resonance region assigned in the middle.

4.4 Concluding Remarks

In this research, we present a method for creation and adjustment of meta vibration mode in finite acoustic phononic crystal. It's proposed that distinct vibration modes can be created by combing the resonance and bandgap characteristics of finite photonic crystal. This concept is applied to a finite piezoelectric metamaterial beam. In the piezoelectric unitcell, inductance load is connected to the piezoelectric transducer individually. Euler beam theory and FEM simulations are carried out to illustrate the metamodes. Specifically, in the unusual vibration mode, resonance vibration is induced while the region with excitation applied has minimum displacement. That is, the vibration modes have the capability of "hit the enemy through another man in between". The unusual vibration modes can be applied to actuators or sensors where only the far end vibration is required. Moreover, this concept can be extended for mass-in-mass or Bragg scattering metamaterials. The present work not only opens the way to the creation of unusual vibration modes, but also to the creation and optimization of actuators or sensors without geometrical tailoring.

Chapter 5 Linear Stiffness Compensation for Enhanced Piezoelectric Energy Harvesting

5.1 Introduction

Due to the rapid advancement in portable and wireless devices, harvesting energy from ambient sources to prolong power supply to these devices has received significant attention (Paradiso and Starner, 2005; Roundy et al, 2005; Mitcheson et al, 2008). As vibration energy is virtually ubiquitous, utilizing piezoelectric transducers for energy harvesting, i.e., converting vibration energy into electrical energy, has emerged as one of the primary methods (Anton and Sodano, 2007; Priya, 2007; Khaligh et al, 2010). Piezoelectric transducers are compact, have high bandwidth, and maintain good linearity within functional range. Design and optimization of piezoelectric transducer-based energy harvesters have been addressed in several aspects (Liang and Liao, 2011): 1) absorbing mechanical energy from vibration source (Shenck and Paradiso, 2001; Shahruz, 2006; Ji et al, 2010); 2) converting mechanical energy into electrical energy (Baker et al, 2005; Xu et al, 2012); and 3) storing electrical energy (Guyomar et al, 2005). Amongst these aspects, the conversion of mechanical energy into electrical energy is generally characterized by the electro-mechanical coupling coefficient of the device, i.e., the ratio of the energy converted to that imposed (Tang and Wang, 2001; Roundy, 2005; Lefeuvre et al, 2006).

The effect of electro-mechanical coupling on energy harvesting has been analyzed in a number of studies. Roundy et al (2005) suggested that the power generated by a piezoelectric harvester was in general proportional to the electro-mechanical coupling. Lefeuvre et al (2006) indicated that the power output at resonance was proportional to the coupling in low coupling condition. Shu and Lien (2006) modeled and analyzed the power output of a piezoelectric energy harvesting system, and concluded that better performance could be achieved with larger coupling and quality factor. Meanwhile, Kim et al (2012) derived an optimal value for maximum power when the coupling coefficient was greater than a certain threshold value. While saturation of power output may exist (Renno et al, 2009), the maximum power output envelop could be increased with the increase of electro-mechanical coupling (Guyomar et

al, 2005; Shu and Lien, 2006). Tang and Yang (2011) further pointed out that a large coupling coefficient boosts power output of a system with standard circuit even more than that with synchronized charge extraction technique (SCE). The electro-mechanical coupling coefficient is directly related to the transducer material property, predominantly the piezoelectric coupling constant at the material-level. For example, one of the most commonly used piezoelectric transducers, PZT5H, has limited piezoelectric coupling constant of 0.44 in the 31 direction and 0.75 in the 33 direction, respectively (when attached to a beam, the 1 coordinate of the transducer is along the length direction, the 2 coordinate the width direction and the 3 coordinate the transversal direction) (IEEE Standard). Choosing transducers with larger piezoelectric coupling constant may certainly help. Rakbamrung et al (2010) compared the performance of two energy harvesters with the same configuration but two different transducers, PMN-PT and PZT. The one with PMN-PT showed higher power output, but this type of material is more expensive.

At the device-level, a number of studies have defined an electro-mechanical coupling coefficient of an energy harvester, and indicated that this coefficient is related to not only the material property of the transducer, but also the specific design features of the harvester. For example, the harvester in general stores a significant portion of energy through its mechanical stiffness throughout the energy harvesting process, which reduces the energy conversion efficiency (Roundy, 2005; Kenji and Takaaki, 2010; Liang and Liao, 2011). It is worth emphasizing that the mechanical stiffness of the energy harvester includes contributions from both the host beam and the piezoelectric transducer. A significant portion of the mechanical stiffness in the harvester comes from the piezoelectric bending stiffness, which cannot be easily reduced. In the unimorph case, a host beam is required, which shifts the beam-shaped transducer's neutral line so the charges generated by the top and bottom halves of the transducer during bending vibration will not offset. The host beam thus has to possess certain thickness, yielding considerable mechanical stiffness. Many investigations have been carried out to explore manipulating the mechanical behavior as well as the circuitry dynamics of the harvester in order to enhance the electro-mechanical coupling. Chen and Wang (2005) investigated the increase of the electro-mechanical coupling of a

piezoelectric cantilever by thickness ratio optimization, and identified a maximum coupling under a proper thickness ratio. Alberto and Paolo (2007) studied the optimal positioning of piezoelectric transducer. These investigations are in the category of mechanical tailoring, and therefore are subject to the limitation of the material-level coupling constant.

It is worth noting that there actually has been a stream of efforts to improve the electro-mechanical coupling coefficient and to tune the system dynamics in a device by resorting to external elements. For example, Tang and Wang (2001) indicated that adding an operational amplifier-based negative capacitance, which offsets the inherent capacitance of the piezoelectric transducer, could increase the electro-mechanical coupling. Since the negative capacitance element itself consumes power, such an approach is more suitable for control/damping applications. For another example, it was found that compressive axial forces could reduce the mechanical bending stiffness of the cantilever (Lesieutre and Davis, 1997; Leland and Wright, 2006; Masana and Daqaq, 2011; Niri and Salamone, 2012). This type of methods is generally effective when the vibration amplitudes are small. To introduce favorable dynamic effects to energy harvesters, conservative forces due to permanent magnets, because of the non-contact nature, recently emerged as an attractive option. Challa et al (2008) attached magnetic blocks on the top and bottom of the cantilever, and created attractive and repulsive forces to adjust the harvester's resonant frequency to match the frequency of the ambient vibration to improve the bandwidth of energy harvesting. As the force by the magnetic blocks exhibits nonlinearity, the system is essentially nonlinear. Cottone et al (2009) placed magnets on the cantilever tip and in the vicinity to generate nonlinearity which was then used to improve the bandwidth of energy harvesting. One challenge in these nonlinear methods is that the system behavior is usually amplitude-dependent, which may limit the effectiveness of the respective methods to a certain operating range.

One ideal solution would be to add a negative spring element to a harvester to reduce its bending stiffness while maintaining the linearity. As mentioned, reducing the mechanical stiffness can increase the electro-mechanical coupling at the system level, and maintaining linearity can ensure that the

performance enhancement can be realized within the entire operating range. Such a negative spring element should be non-contact with no additional damping. Inspired by the recent explorations in incorporating magnets into energy harvester design (Challa et al, 2008; Cottone et al, 2009), in this research we develop a design scheme that enables the compensation of the effective stiffness of the energy harvester by utilizing magnetic effects. In particular, a linear magnetic field effect is synthesized by placing properly configured magnetic elements in the vicinity of the piezoelectric cantilever. The magnetic field produced by these elements yields a linear force with respect to the cantilever displacement that is equivalent to the negative spring element effect, thereby reducing the portion of energy stored in transducer and host structure and improving the electro-mechanical coupling of the system. As the additional force induced is linear, the electro-mechanical coupling improvement is effective throughout the entire operating range of the harvester, and is not amplitude-dependent. Another potential advantage of this design scheme is that adding the aforementioned magnetic elements does not exclude the usage of other design optimization methods proposed previously (Shenck and Paradiso 2001; Baker et al, 2005; Guyomar et al, 2005; Shahruz, 2006; Challa et al, 2008; Cottone et al, 2009; Xu et al, 2012).

The rest of this section is organized as follows. In Section 5.2, the concept of the new design is outlined first, followed by the analysis of the magnetic field to demonstrate the benefits to electro-mechanical coupling improvement and energy harvesting performance. In Section 5.3, experimental studies are reported that validate the analytical predictions. Finally, concluding remarks are provided.

5.2 Design Concept and System Analysis

5.2.1 Schematic of design

Figure 5-1a illustrates the concept of stiffness compensation, where a fictitious negative spring element is included. Figure 5-1b shows the schematic diagram of the new piezoelectric energy harvester system proposed, which is a conventional piezoelectric cantilever incorporated with specially arranged

magnetic elements to improve the electro-mechanical coupling coefficient. The piezoelectric cantilever consists of a cantilevered steel beam bonded with a piezoelectric transducer near the fixed-end. The poling axis of the piezoelectric transducer is perpendicular to the beam. Both the transducer and the beam are geometrically uniform. A sphere-shaped iron mass is attached to the free end of the beam as a proof-mass. A thin, slender magnetic bar is bonded on the top of the beam near the free end. Two additional magnetic sheets are mounted above and underneath the proof-mass, respectively.

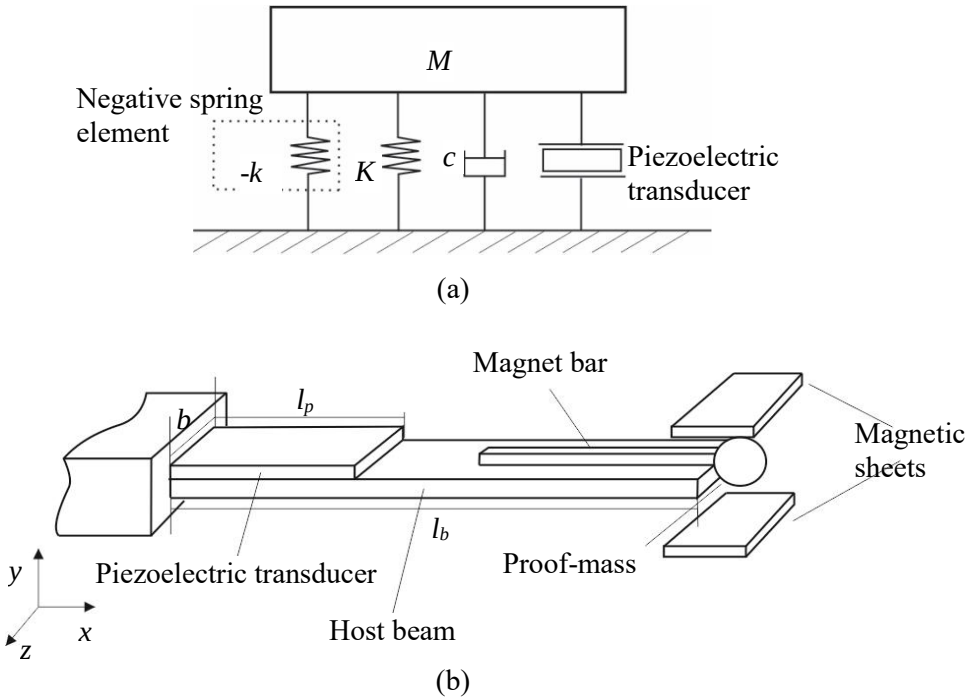

Figure 5-1. (a) Schematic of stiffness compensation; (b) Schematic diagram of the proposed new piezoelectric energy harvester.

Figure 5-2 shows more specifically the arrangement of the two magnetic sheets. These magnetic sheets are placed with the same poles facing each other, and are bonded to non-magnetic backsheets that are fixed in space. They are placed symmetrically with respect to the proof-mass. The relation between the magnetic field of a magnet and the distance is fourth-order in general (Moon, 1978). As stated, our goal here is to create a linear force applied to the beam as it vibrates, that is equivalent to the effect of a

negative spring element so the electro-mechanical coupling can be increased. The challenges and the rationale of the new design are presented as follows.

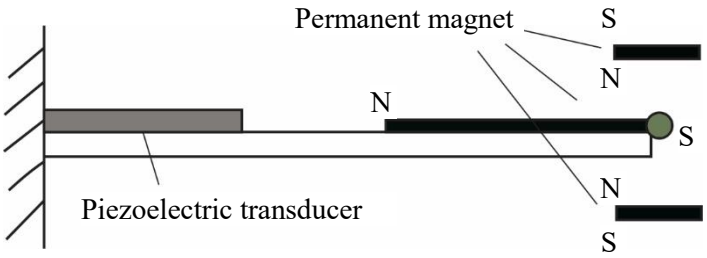

Figure 5-2. Arrangements of magnetic elements.

One challenge here is to identify an arrangement of the magnetic elements that can indeed yield a linear magnetic field. By using the two magnetic sheets shown in Figure 5-2, our hypothesis is that under certain design, the overall effect of the two opposing magnetic fields could lead to a linear field. For example, as the beam vibrates towards the top magnetic sheet, the effects of the two fields due to the top magnetic sheet (from its top and bottom surfaces) increase at a fourth-order relation with respect to beam displacement; meanwhile, the effects of the two fields due to the bottom magnetic sheet are in the opposite directions and also at a fourth-order relation. As the distances between the magnetic sheet surfaces and the beam are in a three-dimensional space, it is possible that, by properly choosing the dimensions of the magnetic sheets as well as the gap between the sheets and the beam, the nonlinearity in the field effects may offset. A similar idea has been explored in a recent study on vibration isolation (Wu et al, 2014).

Another challenge is to utilize the linear magnetic field to create a linear force. One cannot create a linear force by simply placing soft magnetic material or permanent magnet in a linear magnetic field. Indeed, the force applied onto the soft magnet material (such as iron) is proportional to the gradient of the magnetic field, which will not be linearly proportional to the displacement if the magnetic field is linear. If a permanent magnet is employed, as its poles are both subject to the linear magnetic field, the combinatory effect leads to a nonlinear force. In this research, we propose to synthesize a magnetic

monopole effect by using a thin, slender magnetic bar bonded on the top of the beam. One pole of this magnetic bar is placed inside the linear magnetic field, while the other pole is outside. As the other pole is outside of the aforementioned magnetic field, such a placement forms the basis of a magnetic monopole. Moreover, at the end of the slender magnetic bar a sphere-shaped proof-mass is attached, which will regulate the magnetic induction to induce the magnetic monopole effect. As will be shown later, with this configuration, the softening/hardening effect due to the nonlinear magnetic fields can be eliminated, leading to a linear force equivalent to a negative spring element.

5.2.2 Magnetic force analysis

In this section, we analyze the magnetic force generated under the design scheme described in Section 5.2.1. Let l_x, l_z and t_m represent the width, length and thickness of each magnetic sheet, and let h represent the distance between the two magnetic sheets, as shown in Figure 5.3. Let r represent the radius of the iron ball (i.e., the proof-mass). Furthermore, let B_1 and B_2 represent the magnetic flux density at the surfaces of the magnetic sheets and that of the sphere-shaped iron element, respectively. Since the sphere-shaped iron element is directly connected to the magnetic bar ($1\times1\times20$ mm), it is regarded as a permanent magnet as it maintains magnetization. The parameters of the prototype system analyzed in this research are tabulated in Table 1.

Table 1. Parameters of prototype energy harvester.

l_x = 25.8 mm	l_z = 9.9 mm	t_m = 1.5 mm
h = 11.9 mm	r = 2 mm	l_b = 94 mm
l_p = 27.8 mm	b = 11 mm	h_p = 0.25 mm
h_b = 0.45 mm	B_1 = 1876 Gauss	B_2 = 552 Gauss
ρ_p = 7500 kg/m^3	ρ_p = 7900 kg/m^3	E_b = 109 GPa
E_p = 62 GPa	d_{31} = −320 pC/N	$\beta_{33} = 2.92\times10^8$ Vm/C
$h_{31} = 5.9\times10^8$ N/C	m_{pm} = 0.32 g	

The analysis of magnetic force involves two parts, the magnetic field from magnetic sheets and the magnetic property of the proof-mass. We first consider the magnetic field from the two magnetic sheets. In general, the magnetic force between two arbitrary points is related to the magnetic flux density at each point and the distance between the two points (Moon, 1978). Without loss of generality, we can write the magnetic force between an arbitrary point on the surface of the magnetic sheet and the proof-mass as

$$F = q_{\text{ball}} H = \frac{q_{\text{ball}} \sigma_s}{4\pi\mu_0} \int \frac{1}{l^2} dS \tag{5-1}$$

where q_{ball} is the magnetic charge on the iron ball, H denotes the magnetic H-field, σ_s is the magnetic charge density on the surfaces of the magnetic sheets, μ_0 is the magnetic permeability in a classical vacuum, l is the distance between the iron ball and an arbitrary magnetic charge on the surface of the magnetic sheet, and dS represents an infinitesimal area on the surface of the magnetic sheet. Recall that the two magnetic sheets are symmetrically arranged with respect to the beam neutral plane. We specifically consider a line that connects the center points of the two sheets. The magnetic force at an arbitrary point on this line results from the magnetic forces from all four surfaces of the two magnetic sheets, and the *y*-direction component is

$$F_y = \frac{q_{\text{ball}}}{4\pi\mu_0} \sigma_s \int_S \left(\frac{1}{s_1^2} \cos\theta_1 - \frac{1}{s_2^2} \cos\theta_2 - \frac{1}{s_3^2} \cos\theta_3 + \frac{1}{s_4^2} \cos\theta_4 \right) dS \tag{5-2}$$

where S stands for the four surfaces mentioned above, s_1, s_2, s_3 and s_4 denote the distances from those surfaces to the proof-mass, and θ_1, θ_2, θ_3 and θ_4 denote the angles between the lines of s_1, s_2, s_3, s_4 and the *y*-axis, respectively,

$$s_1 = \sqrt{x^2 + z^2 + \left(\frac{1}{2} h - w(l_b, t) \right)^2}, \quad s_2 = \sqrt{x^2 + z^2 + \left(\frac{1}{2} h + t_m - w(l_b, t) \right)^2}$$

$$s_3 = \sqrt{x^2 + z^2 + \left(\frac{1}{2}h + w(l_b,t)\right)^2}, \qquad s_4 = \sqrt{x^2 + z^2 + \left(\frac{1}{2}h + t_m + w(l_b,t)\right)^2} \tag{5-3a-d}$$

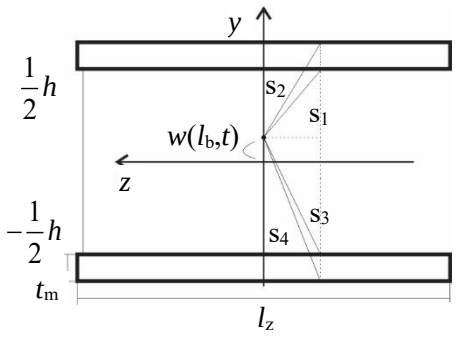

Figure 3. Schematic for magnetic flux density calculation.

As the beam vibrates during energy harvesting, we let $w(x,t)$ denote the displacement of the beam in the *y*-direction at location *x* and time *t* (to be further analyzed in the subsequent section). $w(l_b,t)$ in Equation (5-3) then denotes the displacement of the proof-mass, where l_b is the length of the host beam. It is worth noting that, owing to the symmetrical arrangements, the horizontal components of the magnetic forces offset. We can further derive

$$F_y = q_{\text{ball}} \frac{\sigma_s}{4\pi\mu_0} \int_{-\frac{l_z}{2}}^{\frac{l_z}{2}} \int_{-\frac{l_x}{2}}^{\frac{l_x}{2}} \left(\frac{1}{s_1^2} \frac{\frac{1}{2}h - w(l_b,t)}{s_1} - \frac{1}{s_2^2} \frac{\frac{1}{2}h + t_m - w(l_b,t)}{s_2} - \frac{1}{s_3^2} \frac{\frac{1}{2}h + w(l_b,t)}{s_3} + \frac{1}{s_4^2} \frac{\frac{1}{2}h + t_m + w(l_b,t)}{s_4} \right) dxdz \tag{5-4}$$

At this point we may evaluate the linearity of F_y with respect to the beam displacement/vibration. Since the magnetic charge on the iron ball keeps constant, the magnetic force depends upon the magnetic flux density from the two sheets. As shown in Equation (5-1), the force is the product of the magnetic charge and the flux density. We perform numerical analysis of the magnetic flux density by using the parameters given in Table 1, and the results are shown in Figure 4.

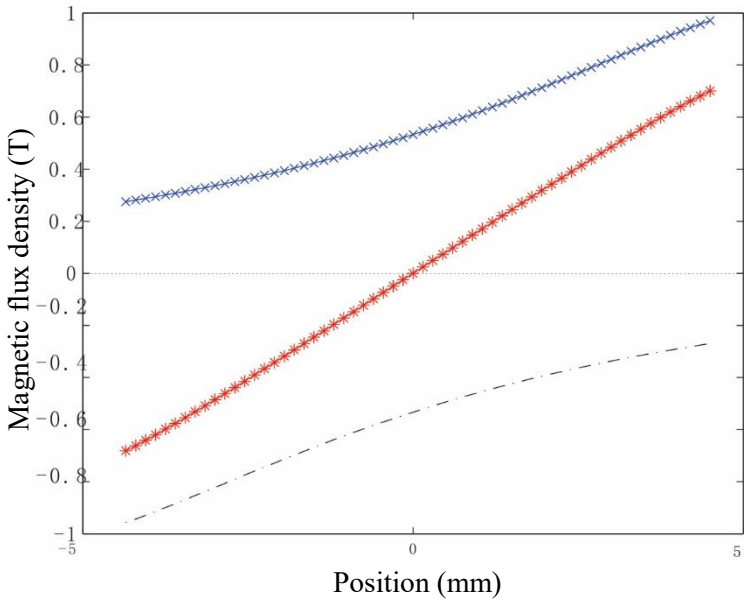

Figure 4. Magnetic flux densities calculated. -*-: combined magnetic flux density, -x-: magnetic flux density from top sheet, -. -: magnetic flux density from bottom sheet.

While the individual magnetic flux density of each sheet is obviously nonlinear, the combined flux density shows good linearity. The linearity of the combined one is due to that the high-order terms in the magnetic flux density of the two sheets offset. We derive the Taylor series expansion of F_y with respect to the beam displacement/vibration (within the range of 0.01 m), and obtain

$$F_y = 1.67\times10^{-2} w(l_b,t) + 1.37\times10^{-5} w(l_b,t)^2 + 2.14\times10^{-6} w(l_b,t)^3 + \mathrm{o}(w(l_b,t)^4) \tag{5-5}$$

The above equation shows a nearly linear relation. Moreover, the tangential stiffness due to the magnetic force is given as

$$k_y = 1.67\times10^{-2} + 2.74\times10^{-5} w(l_b,t) + 6.42\times10^{-6} w(l_b,t)^2 + \mathrm{o}(w(l_b,t)^3) \tag{5-6}$$

It should be noted that for the beam considered, the range within which the magnetic force shows good linearity, 0.01 m, is actually quite large. The high-order terms in the tangential stiffness expression are much smaller (i.e., three orders of magnitude smaller) than the constant term.

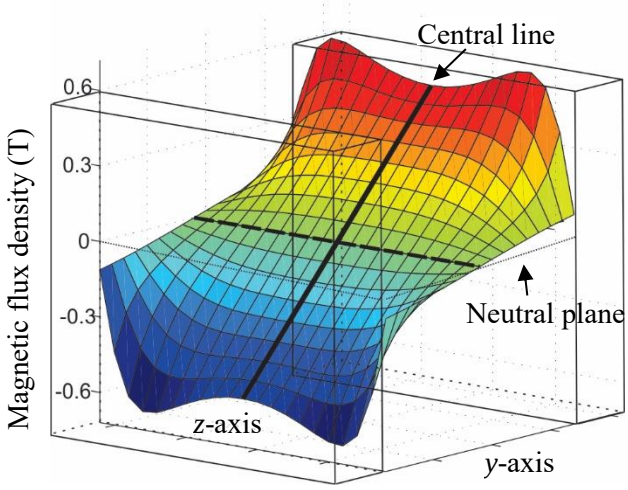

Figure 5-5. Magnetic flux density on neutral plane.
(Neutral plane refers to the *yz*-plane connecting the middle lines of two plates.
Central line refers to the middle line on the neutral plane.
The tip of the cantilever moves along the central line)

We analyze the magnetic flux density using the equations provided above. Indeed, the magnetic flux density between the two magnetic sheets is proportional to F_y shown in Equation (5-4). We calculate the magnetic flux density on the neutral *yz*-plane under given parameters, and the result is shown in Figure 5-5. Along the central line that passes through the proof mass, very good linearity can be observed. Figure 5-6 plots the difference of the magnetic flux density calculated and its linear approximation, which is very small as expected.

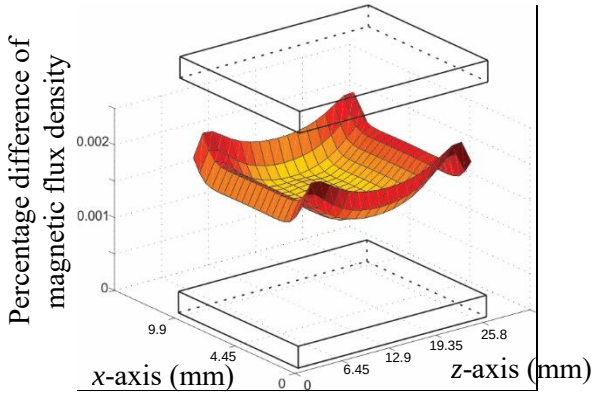

Figure 6. Percentage difference between magnetic flux density calculated and the linear approximation.

We carry out some further analyses to elucidate the parametric influence. The linearity of the magnetic field depends on a number of parameters, for instance, the distance between the two sheets, *h*, the length, l_x , and the width, l_z , of the sheets. Figures 5-7 and 5-8 illustrate the influences of *h* and width l_z under constant l_x .

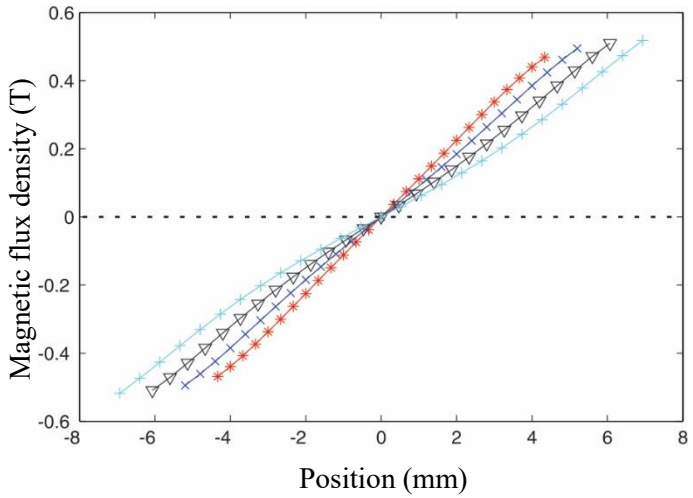

Figure 5-7. Influences of *h* under constant l_x and l_z . -*-: *h* = 10 mm, -x-: *h* = 12 mm, -Δ-: *h* = 14 mm, -+-: *h* = 16 mm.

From Figure 5-7, it can be seen that good linearity can be achieved with properly chosen *h*. Although decreasing *h* will increase the magnetic flux density, more significant nonlinearity may also arise. Similar conclusion can be drawn from Figure 5-8.

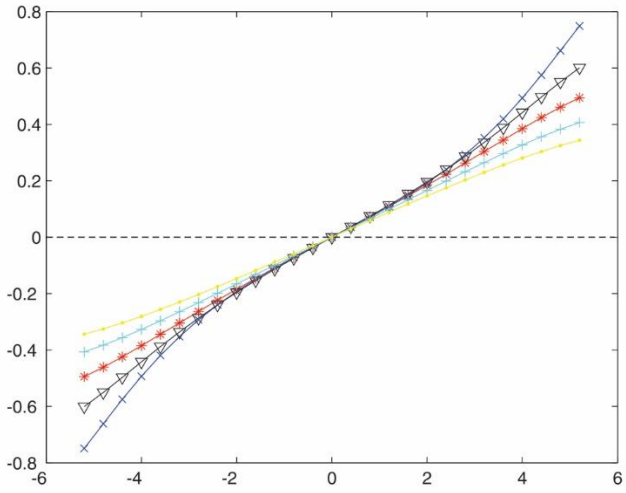

Figure 5-8. Influences of l_z under constant l_x and h. -x-: l_z = 6 mm, -Δ-: l_z = 8 mm, -*-: l_z = 9.9 mm, -+-: l_z = 12 mm, -.-: l_z = 14 mm.

We now consider the effect of the magnetic property of the proof-mass. As indicated in Section 5.2.1, ideally, one would like to have a mono-pole like proof-mass to make utilization of the magnetic field. Here we resort to 3-D finite element analysis using ANSYS, as shown in Figure 5-9.

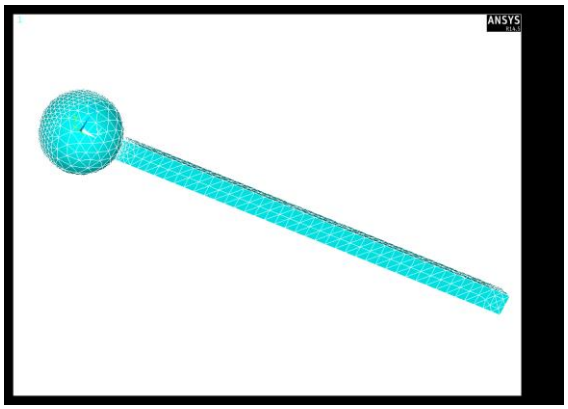

Figure 5-9. Meshed 3-D scheme of proof-mass and magnetic bar.

A sphere-shaped iron mass with radius 2 mm is attached at the end of the slender magnetic bar ($1\times1\times20$ mm). In ANSYS analysis, the domain is defined as air with permeability of 1, and Solid236 element is used to model the air and Solid111 element is used to model the infinite boundary condition. The static magnetic flux density obtained from ANSYS is shown in Figure 5-10a. It can be observed that

magnetic induction lines spread in a spherically symmetric manner from the proof-mass, which indeed yields the form of magnetic mono-pole. In other words, this particular proof-mass selected can be regarded as a point-like magnetic source with constant magnetic flux density. By this design, the linearity of the magnetic force derived above can be realized.

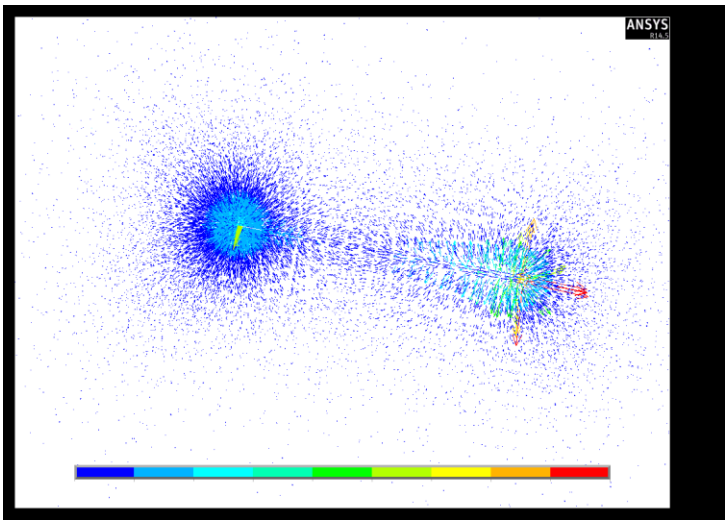

(a)

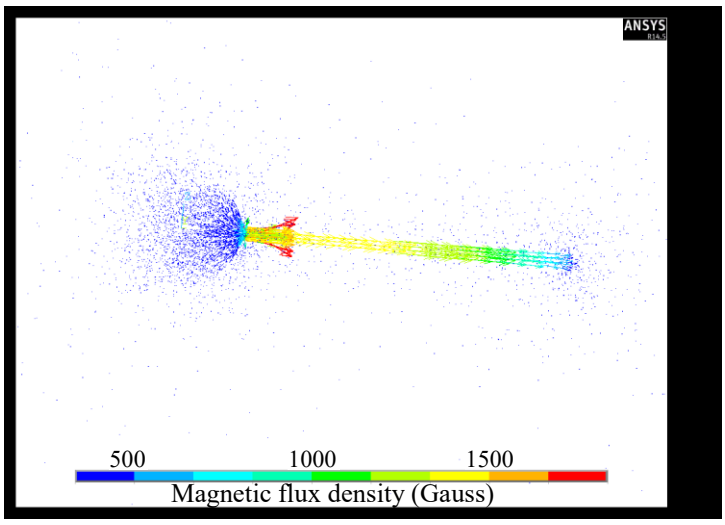

(b)

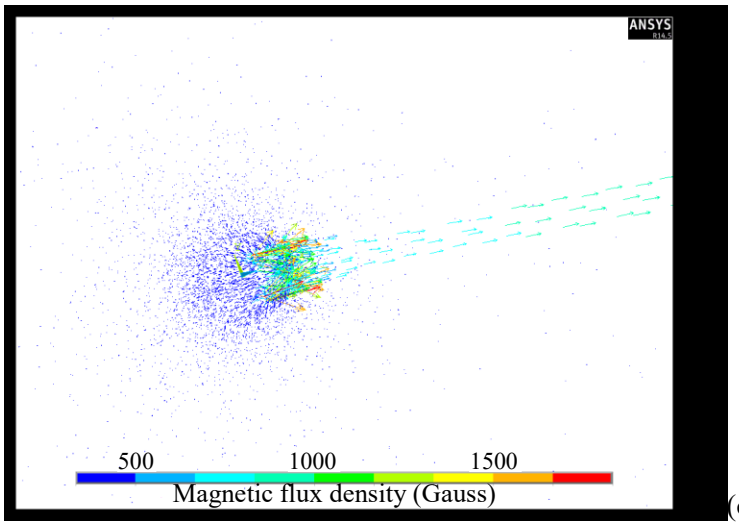

(c)

Figure 5-10. Static magnetic flux density computed: (a) r = 2 mm; (b) r = 4 mm; (c) r = 1 mm.

In comparison, we also analyze the influence of the size of the sphere-shaped proof-mass to the distribution of the magnetic flux density. Figures 5-10b and 5-10c plot the results corresponding to different radii. In Figure 5-10b, when the radius is 4 mm, one can observe an under-magnetization situation which is due to the ineffective magnetization of the proof-mass. In Figure 5-10c, when the radius is 1 mm, one can observe an over-magnetization situation. It should be mentioned that in general the magnetic bar should be sufficiently long in order to avoid the magnetic confinement fusion between its two ends.

In summary, the analysis in this sub-section shows that it is feasible to produce a linear negative force that can compensate the mechanical stiffness of the piezoelectric cantilever by properly configured magnetic fields. Hereafter, the equivalent negative stiffness is expressed as

$$k_{\text{mag}} = \left. \frac{dF_y}{dw(l_b,t)} \right|_{w(l_b,t)=0} \tag{5-7}$$

5.2.3 Modeling and analysis of the harvester

In this section, we investigate the characteristics of the piezoelectric cantilever incorporated with the

proposed stiffness compensation scheme. Assumptions are made as follows: (1) this prototype is considered as a composite Euler–Bernoulli beam; therefore, the effects of shear deformation and rotary inertia of the beams are neglected; (2) the piezoelectric layer is perfectly bonded to the beam; thus, there is no sheer strain between the layers; (3) only the damping of the harvester structure is considered; and (4) the system is excited by base-movement $u(t)$.

The equations of motion of the system can be derived by using the assumed mode method. Here we let the beam displacement be expressed as

$$w(x,t) = \phi(x)q(t) \tag{5-8}$$

where we use one-mode assumption and, without loss of generality, $\phi(x)$ is the first bending mode of the beam. q is the generalized displacement. Based on the extended Hamilton's principle. Let l_p, l_b, b, m_{pm}, t_p, t_b, ρ_p and ρ_b represent, respectively, the length of the piezoelectric transducer and that of the beam, the width of the piezoelectric composite beam, the proof mass, the thickness of the transducer and that of the beam, and the mass density of the transducer and that of the beam. The equations of motion of the system can be derived by using the extended Hamilton's principle,

$$\int_{t_1}^{t_2} \left(\delta T - \delta U + \delta W_c + \delta W_f \right) dt = 0 \tag{5-9}$$

where T is the kinetic energy, U is the potential energy, W_c is the virtual work of damping force, and W_f is the virtual work due to the magnetic effects. As mentioned, the beam displacement is discretized as shown in Equation (5-8), in which the assumed mode is chosen as the first bending mode of the cantilever beam (Ertuck and Inman, 2010),

$$\phi(x) = \cos\frac{\lambda}{l_b}x - \cosh\frac{\lambda}{l_b}x + \varsigma\left(\sin\frac{\lambda}{l_b}x - \sinh\frac{\lambda}{l_b}x \right) \tag{5-10}$$

where $\varsigma = \dfrac{\sin\lambda - \sinh\lambda}{\cos\lambda + \cosh\lambda}$, and the eigenvalue λ is the smallest one solved from $\cos(\lambda l_b)\cosh(\lambda l_b) = -1$.

Let $A_b = bt_b$ and $A_p = bt_p$ represent, respectively, the cross sectional area of the beam and that of the piezoelectric transducer.

The kinetic energy and its variation can be derived as

$$T = \frac{1}{2}\rho_b A_b \int_0^{l_b} \left(\frac{\partial w(x,t)}{\partial t} + \frac{\partial u(t)}{\partial t} \right)^2 dx + \frac{1}{2}\rho_p A_p \int_0^{l_p} \left(\frac{\partial w(x,t)}{\partial t} + \frac{\partial u(t)}{\partial t} \right)^2 dx + \frac{1}{2} m_{pm} \left(\frac{\partial w(l_b,t)}{\partial t} + \frac{\partial u(t)}{\partial t} \right)^2 \tag{5-11}$$

and

$$\begin{aligned} \delta T = & [\rho_b A_b \int_0^{l_b} \phi^2(x)\ddot{q}(t)dx + \rho_p A_p \int_0^{l_p} \phi^2(x)\ddot{q}(t)dx + m_{pm}\phi^2(l_b)\ddot{q}(t) + \rho_b A_b \int_0^{l_b} \phi(x)\ddot{u}(t)dx \\ & + \rho_p A_p \int_0^{l_p} \phi(x)\ddot{u}(t)dx + m_{pm}\phi(l_b)\ddot{u}(t)]\delta q + [\rho_b A_b \int_0^{l_b} \phi(x)\ddot{q}(t)dx + \rho_p A_p \int_0^{l_p} \phi(x)\ddot{q}(t)dx + m_{pm}\phi(l_b)\ddot{q}(t) \\ & + \rho_b A_b \int_0^{l_b} \ddot{u}(t)dx + \rho_p A_p \int_0^{l_p} \ddot{u}(t)dx + m_{pm}\ddot{u}(t)]\delta u \end{aligned} \tag{5-12}$$

The coefficient of the inertia term, i.e., the modal mass, is

$$M = \rho_b A_b \int_0^{l_b} \phi^2(x)dx + \rho_p A_p \int_0^{l_p} \phi^2(x)dx + m_{pm}\phi^2(l_b) \tag{5-13}$$

As the base movement/excitation effect is included in the kinetic energy, the modal force due to base movement/excitation can be written as

$$F_a = -\left[\rho_b A_b \int_0^{l_b} \phi(x)dx + \rho_p A_p \int_0^{l_p} \phi(x)dx + m_{pm}\phi(l_b) \right] \ddot{u}(t) \tag{5-14}$$

The linear constitutive relation of the piezoelectric transducer is (IEEE, 1987)

$$\begin{cases} \tau = E_p \varepsilon - h_{31} D \\ E = -h_{31}\varepsilon + \beta_{33} D \end{cases} \tag{5-15}$$

where τ, ε, D and E represent, respectively, the stress, stain, electrical displacement (charge/area) and electrical field (voltage/length) of the piezoelectric transducer, and E_p, h_{31} and β_{33} are the Young's modulus, piezoelectric constant and dielectric constant of the transducer. We let E_b be the Young's

modulus of the host beam, and let I_b and I_p represent the moments of inertia of the beam and the transducer, respectively. The elastic and electrical energy of the harvester comes from the host beam and the transducer. The variation of the elastic and electrical energy can be derived as (Tang and Wang, 2001)

$$\begin{aligned}
&\delta U = \delta U_b + \delta U_p = \int_{V_b} \tau \delta \varepsilon dV_b + \int_{V_p} \left(\tau \delta \varepsilon + E \delta D \right) dV_p \\
&= \int_{V_b} E_b \varepsilon \delta \varepsilon dV_b + \int_{V_p} E_p \varepsilon \delta \varepsilon dV_p - \int_{V_p} h_{31} D \delta \varepsilon dV_p - \int_{V_p} h_{31} \varepsilon \delta D dV_p + \int_{V_p} \beta_{33} D \delta D dV_p \\
&= \int_0^{l_b} EI_b \left(\phi''(x) \right)^2 q(t) \delta q(t) dx + \int_0^{l_p} EI_p \left(\phi''(x) \right)^2 q(t) \delta q(t) dx \\
&- \int_0^{l_p} h_{31} D \int_0^{t_p} y \phi''(x) \delta q(t) dy dx - \int_0^{l_p} h_{31} \int_0^{t_p} y \phi''(x) q(t) \delta D dy dx + \int_0^{l_p} \int_0^{t_p} \beta_{33} D \delta D dy dx \\
&= (k_b + k_p) q \delta q + k_{pq} D \delta q + k_{pq} q \delta D + k_{pp} D \delta D
\end{aligned} \tag{5-16}$$

where

$$K = k_b + k_p = \int_0^{l_b} EI_b \left(\phi'' \right)^2 dx + \int_0^{l_p} EI_p \left(\phi'' \right)^2 dx, \quad k_{pq} = \int_0^{l_p} F_p h_{31} \phi'' dx, \quad k_{pp} = \int_0^{l_p} A_p \beta_{33} dx \tag{5-17a-c}$$

F_p is the first moment of area of the transducer. K is the modal mass of the piezoelectric composite beam.

The virtual work terms due to the mechanical damping and the magnetic force can be written as

$$\delta W = \delta W_c + \delta W_F = -\int_0^{l_b} c \frac{\partial w(x,t)}{\partial t} \delta q dx + k_{\text{mag}} \phi^2 (l_b) q \delta q \tag{5-18}$$

In this research we assume that the charge Q is uniformly distributed, i.e.,

$$D = \frac{Q}{bl_p} \tag{5-19}$$

We further define

$$k_1 = \frac{k_{pq}}{bl_p}, \quad k_2 = \frac{k_{pp}}{(bl_p)^2} \tag{5-20a, b}$$

Finally, substitution of the above expressions into Equation (5-9) yields the equations of motion of

the entire system as shown in Equation (5-21).

$$\begin{cases} M\ddot{q} + c\dot{q} + \left(K - k_m\right)q + k_1 Q = F_a \\ R\dot{Q} + k_2 Q + k_1 q = 0 \end{cases} \tag{5-21}$$

where M, c, and K are respectively the modal mass, damping, and open-circuit stiffness of the piezoelectric cantilever, k_1 is the electro-mechanical coupling term, R is the resistance load in the system, and k_2 is the inverse of the capacitance of the piezoelectric transducer. F_a is the modal force due to the based excitation. Details of these terms can be found in Appendix. In Equation (5-21), the negative stiffness effect due to the magnetic effect is denoted as

$$k_m = k_{\text{mag}}\phi^2(l_b) \tag{5-22}$$

where k_{mag} is given by Equation (5-7). Essentially, k_m represents the stiffness reduction to the mode of interest.

We now analyze the frequency response characteristics of the harvester. Hereafter we use the tilde notation to indicate the magnitude of the related quantity. The frequency response of displacement amplitude $\tilde{q}$ with respect to base excitation amplitude $\tilde{F}_a$ is given as

$$\frac{\tilde{q}}{\tilde{F}_a} = \frac{Ri\omega + k_2}{\left(Ri\omega + k_2\right)\left(-\omega^2 M + ci\omega + K - k_m\right) - k_1^2} \tag{5-23}$$

We carry out non-dimensionalization, and define,

$$\omega_n = \sqrt{\frac{K - k_m}{M}}, \qquad \Omega = \frac{\omega}{\omega_n}, \qquad \varsigma = \frac{c}{\sqrt{(K - k_m)M}}, \qquad r = \frac{R}{k_2}\omega_n \tag{5-24a-d}$$

which represent, respectively, natural frequency of the harvester beam, non-dimensional excitation frequency, mechanical damping ratio, and resistance load. We further introduce the definition of the electro-mechanical coupling coefficient of the harvester (Guyomar et al, 2005; Shu and Lien, 2006),

$$k_e^2 = \frac{k_1^2}{(K - k_m)k_2} \tag{5-25}$$

As pointed out in previous studies (Tang and Wang, 2001; Guyomar et al, 2005; Shu and Lien, 2006), at the device level, this electro-mechanical coupling coefficient explicitly includes the mechanical stiffness into the analysis of energy conversion, i.e., the ratio of the energy converted to that imposed. Indeed, the mechanical stiffness of a system integrated with a piezoelectric transducer is dependent on many factors, e.g., the geometry of the transducer and the configuration of the host structure, etc. Using the same transducer material, the equivalent mechanical stiffness of the actual system may vary drastically, causing significant difference in system-level energy conversion capability. For the proposed harvester with magnetic effect, the relation between the electro-mechanical coupling coefficient and the negative stiffness due to the magnetic effects, k_m, is shown in Figure 5-11.

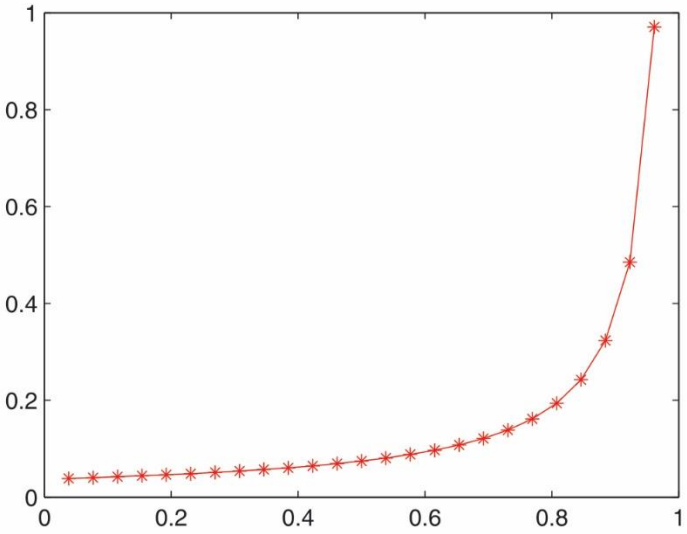

Figure 5-11. Electro-mechanical coupling coefficient versus compensating stiffness ratio.

As can be observed, as the stiffness compensation effect increases and less potential energy is stored in the system, the electro-mechanical coupling generally increases.

The normalized displacement of the beam can be obtained as

$$\bar{q} = \frac{\tilde{q}}{\tilde{F}_a / (K - k_m)} = \frac{ir\Omega + 1}{(ir\Omega + 1)(-\Omega^2 + i\varsigma\Omega + 1) - k_e^2} \tag{5-26}$$

Under open-circuit and short-circuit conditions, we have $r \to \infty$ and $r \to 0$, respectively, and the normalized frequency responses are

$$\bar{q}_{\text{open}} = \frac{\tilde{q}}{\tilde{F}_a / (K - k_m)} = \frac{1}{-\Omega^2 + i\varsigma\Omega + 1} \tag{5-27a}$$

$$\bar{q}_{\text{short}} = \frac{\tilde{q}}{\tilde{F}_a / (K - k_m)} = \frac{1}{-\Omega^2 + i\varsigma\Omega + 1 - k_e^2} \tag{5-27b}$$

Therefore, under open-circuit condition, the frequency response of displacement is not related to the electro-mechanical coupling coefficient k_e. It is worth noting that the open-circuit resonant frequency ω_o and the short-circuit resonant frequency ω_s are related by the aforementioned electro-mechanical coupling coefficient in the following manner (Tang and Wang, 2001),

$$\omega_s = \sqrt{1 - k_e^2}\,\omega_o \tag{5-28}$$

which can be used subsequently in the experimental analysis. Similarly, the normalized frequency response of voltage $\bar{V}$ output of the harvester can be derived as

$$\bar{V} = \frac{\tilde{V}}{\tilde{F}_a M k_2} = \frac{i\Omega k_e r}{(ir\Omega + 1)(-\Omega^2 + i\varsigma\Omega + 1) - k_e^2} \tag{5-29}$$

Under open-circuit condition, we have

$$\bar{V}_{\text{open}} = \frac{\tilde{V}}{\tilde{F}_a M k_2} = \frac{i\Omega k_e}{-\Omega^2 + i\varsigma\Omega + 1} \tag{5-30}$$

We can readily observe that the open-circuit voltage response is proportional to the electro-mechanical coupling coefficient. The frequency responses of open-circuit voltage under increased electro-mechanical coupling coefficients (due to stiffness compensation) are shown in Figure 5-12.

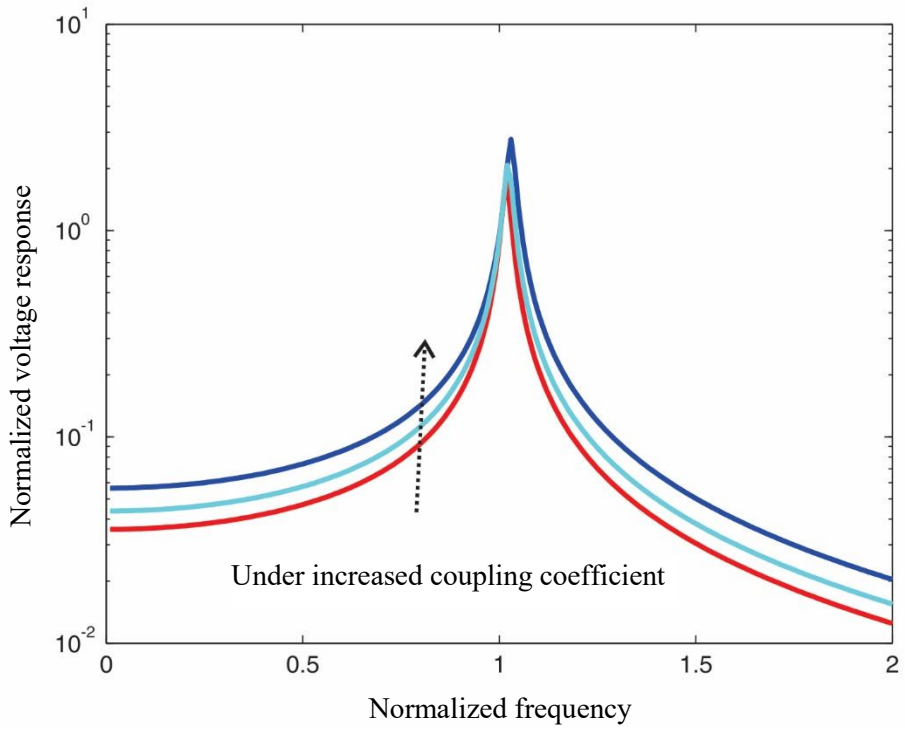

Figure 5-12. Normalized voltage frequency responses under increased coupling coefficient.

It can be seen that the normalized frequency response of voltage is increased in the entire frequency range with the increase of the electro-mechanical coupling coefficient.

5.3 Experimental Validation and Discussion

Experiments are carried out to verify the proposed stiffness compensating scheme as well as the new harvester performance. The parameters involved are given in Table 1, which are consistent with those used in the preceding analysis. The experimental setup is shown in Figure 5-13. The transducer, PZT-5H, was purchased from Piezo Systems Inc. The magnetic sheets were purchased from K&J Magnet Inc. The PZT transducer was bonded to the steel beam by using epoxy glue (DP100) and underwent curing for 24 hours at room temperature. The two magnetic sheets were bonded to non-magnetic backsheets, and the magnetic bar and iron ball were bonded to the cantilever beam in the same way.

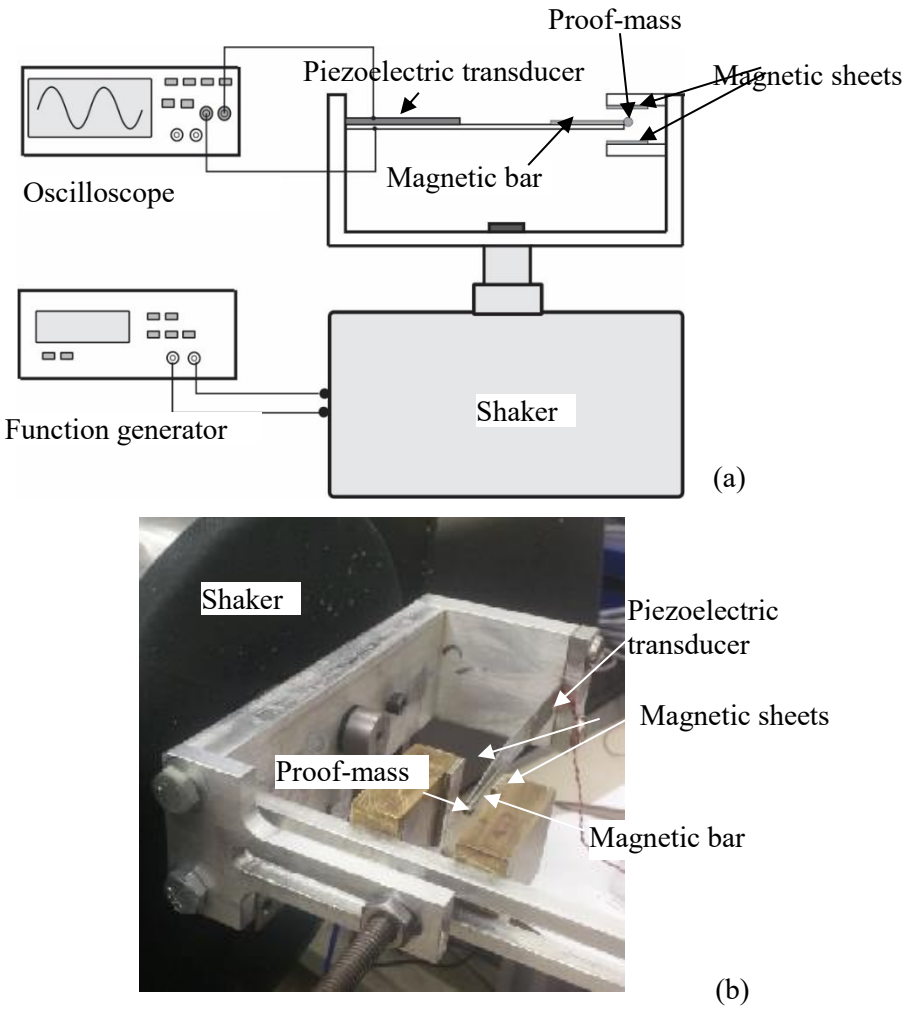

Figure 5-13. Experimental setup. a) schematic of the experiment, b) photograph of the prototype.

Figure 5-14 shows the experimental data of magnetic flux density along the central line that passes through the proof-mass measured by a Hall sensor. As can be observed, very good linearity of the magnetic flux density is achieved, and the numerical and experimental results match very well.

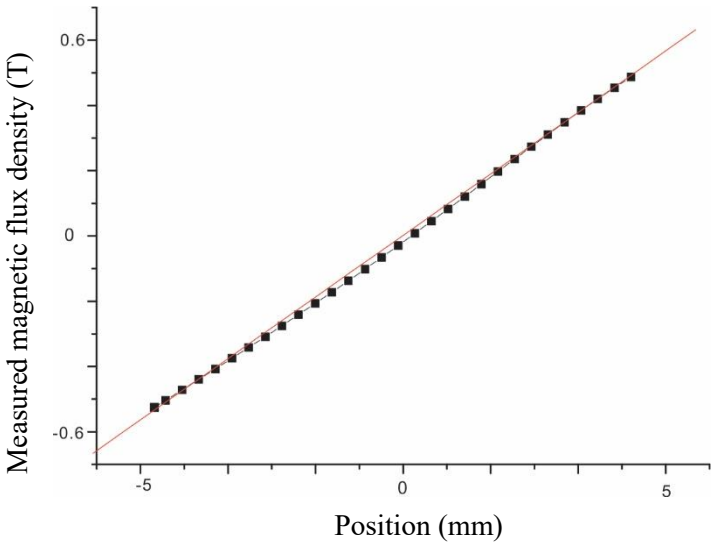

Figure 5-14. Measured magnetic flux density and linear fit.

measured data; linear fit.

Recall the relation between the electro-mechanical coupling coefficient and the resonant frequencies shown in Equation (5-28). The coupling coefficient k_e^2 can be calculated through measured open-circuit and short-circuit resonant frequencies. Here we record the frequency responses of displacements at the middle of cantilever under sinusoidal base movement with constant amplitude acceleration of 0.1 g measured by an eddy current displacement sensor (3300XL/8mm).

Figures 5-15a and 5-15b show the frequency responses comparison. For the piezoelectric cantilever without stiffness compensation, the open-circuit and short-circuit resonant frequencies are, 48.29 Hz and 47.44 Hz, respectively. The coupling coefficient is 0.0349. For the piezoelectric cantilever with stiffness compensation, the open-circuit and short-circuit resonant frequencies are, 36.1 Hz and 35.04 Hz, respectively. Thus, the stiffness of the piezoelectric cantilever is reduced by 44.1%, and the coupling coefficient is increased to 0.0576. The coupling coefficient is increased by 65%. It is worth commenting that under open-circuit condition, the peak responses are actually smaller, possibly caused by the additional energy dissipation due to leakage resistance of the piezoelectric transducer.

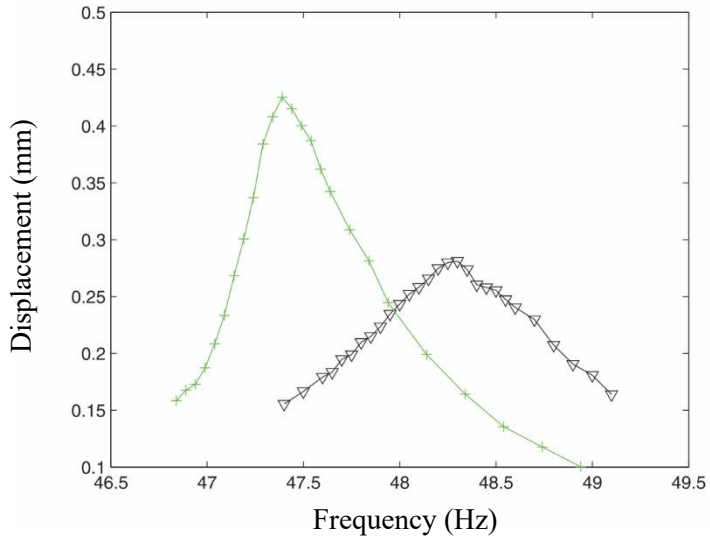

(a)

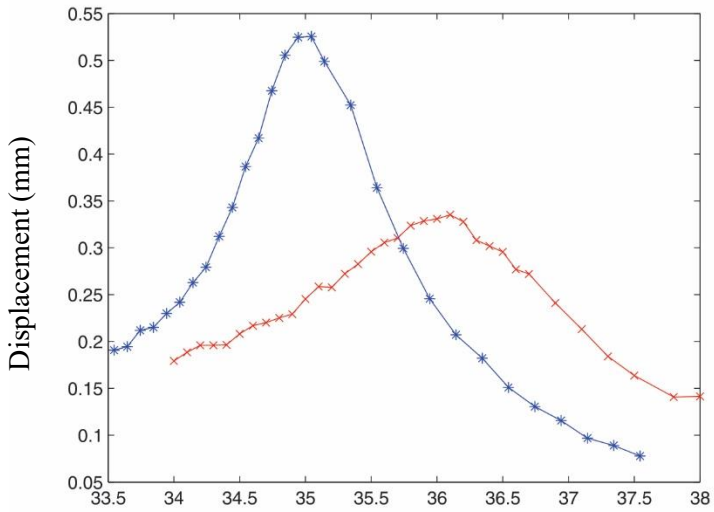

(b)

Figure 5-15. Measured displacement frequency responses (a) without stiffness compensation, -+- : short-circuit, -Δ-: open-circuit; (b) with stiffness compensation, -*-: short-circuit, -x-: open-circuit.

Figure 5-16 shows the experimental data of open-circuit voltage frequency response of the piezoelectric cantilever without and with the magnetic effects under 0.2 g base excitation. To validate the performance improvement, Figure 16 also includes the numerical prediction results obtained based on the model presented in the preceding section. As can be observed, the numerical and experimental results

match very well. The peak voltage output of the piezoelectric cantilever measured without the magnetic effects is 8.6 V at 48.29 Hz. With the magnetic effects, the resonant frequency is reduced to 36.1 Hz and the peak voltage output is increased to 10.9 V. In other words, the peak voltage output is increased by 27%. It is worth commenting that, while the proposed scheme of stiffness compensation reduces the resonant frequency in a way similar to adding a larger proof-mass, it has a unique benefit that the open-circuit voltage is increased in the entire frequency range since the electro-mechanical coupling coefficient of the harvester is increased. This method can be combined with other techniques to optimize the harvester performance.

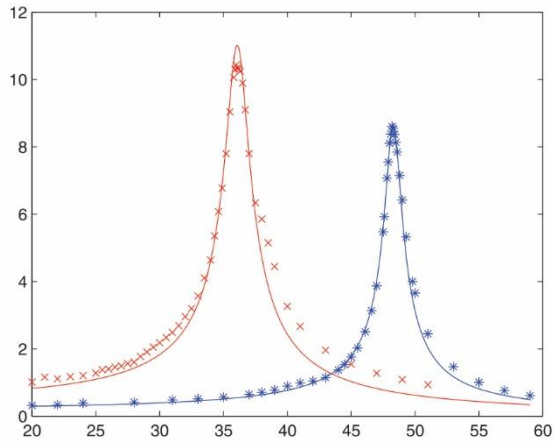

Figure 16. Measured and computed frequency responses of voltage output. -x-: response with stiffness compensation, -*-: response without stiffness compensation.

We also analyze the frequency responses of voltage output for the system with stiffness compensation under different excitation levels, and the measurement results are plotted in Figure 5-17. The peak voltage output is measured as 6.2 V, 10.9 V, 15.8 V and 19.2 V at resonance under excitation levels of 0.1 g, 0.2 g, 0.3 g, and 0.4 g, respectively. The relation between excitation level and peak voltage output is plotted in Figure 18, where we can observe that the voltage output maintains proportionality with respect to the excitation levels, which indicates the amplitude-independent feature of this scheme. In other words, the effectiveness of the enhanced harvester is not limited to a certain operating range. It should be noted that, the peak-to-peak displacement of the tip of the cantilever under 0.4 g excitation is 5.6 mm,

which is within the space limitation between the two magnetic sheets. Therefore, the effective operating range of the proposed scheme is quite large.

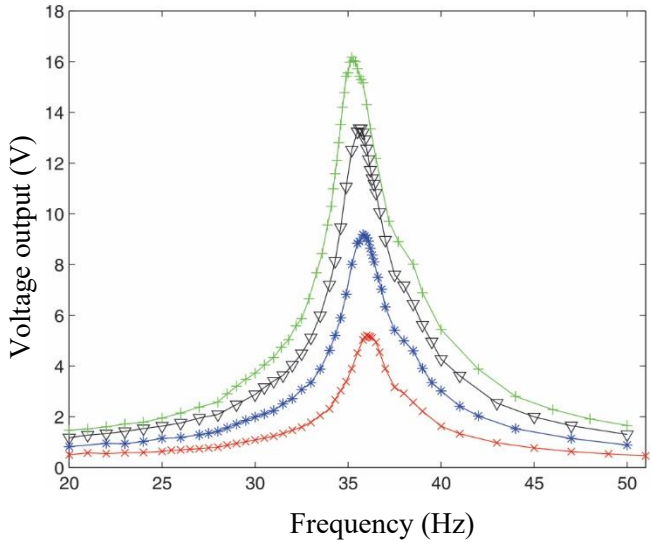

Figure 5-17. Measured frequency responses of voltage output under different excitation amplitudes with stiffness compensation. -x-: amplitude of 0.1 g, -*-: amplitude of 0.2 g, -Δ-: amplitude of 0.3 g, -+-: amplitude of 0.4 g.

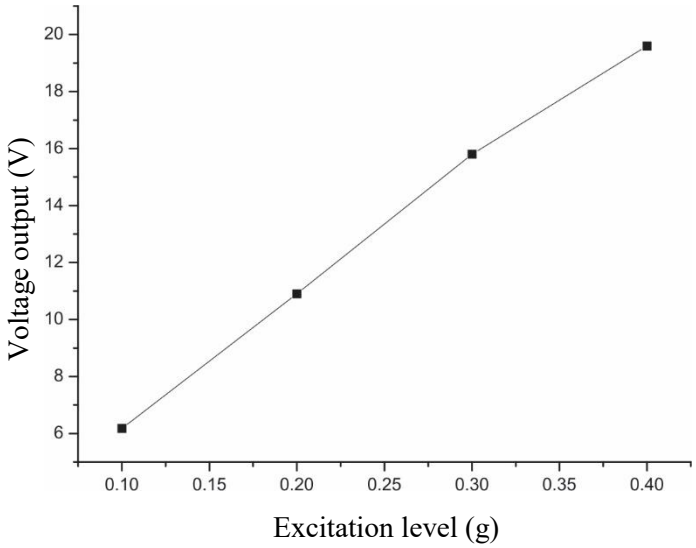

Figure 5-18. Relation between excitation level and peak-to-peak voltage output.

Finally we examine the power output performance. For easy comparison, we simply apply the optimal resistance load (Shu and Lien, 2006; Ji et al, 2010)

$$R_{\text{opt}} \approx \frac{\pi}{2\omega C_p} \tag{5-31}$$

where $C_p = 1/k_2$ is the piezoelectric capacitance, and ω is the excitation frequency. For the system without and with stiffness compensation, the optimal resistance loads measured under 0.015 g base acceleration for maximum power output are plotted in Figure 5-19.

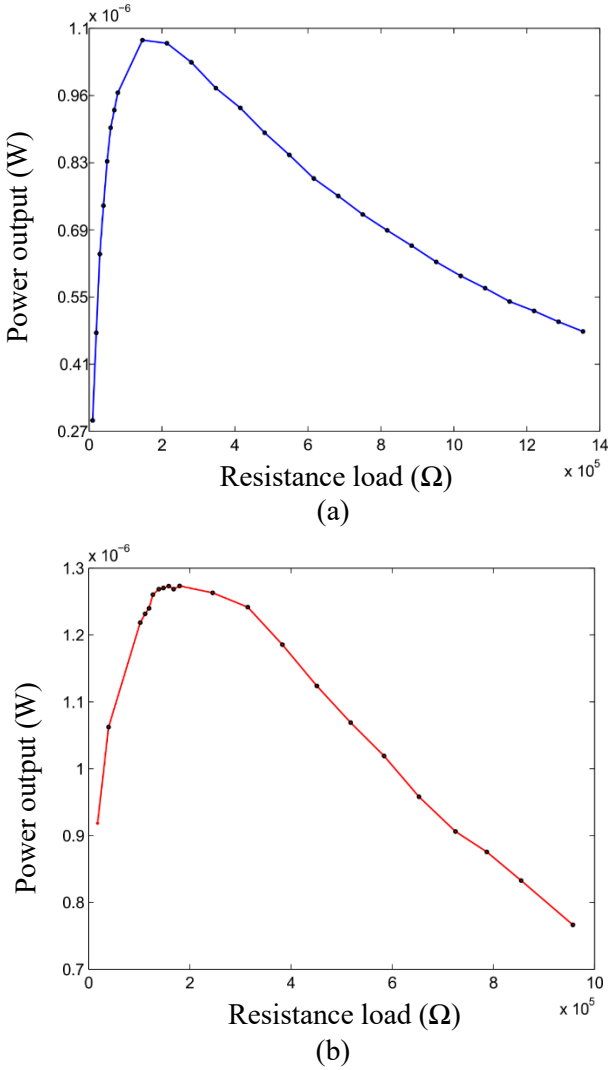

Figure 5-19. Optimal resistance load for maximum power output. (a) without stiffness compensation; (b) with stiffness compensation.

The best matching loads are chosen as 158 kΩ and 189 kΩ for the system without and with stiffness compensation, respectively. Since the best matching load is a function of the resonant frequency, for the

respective system the best matching loads are different although the piezoelectric transducers have the same size. The resulting peak-to-peak voltage across the load resistance was measured by an oscilloscope. The output power was calculated as (Lefeuvre et al, 2006; Challa et al, 2008)

$$P = \frac{V_{p-p}^2}{8R_{\text{opt}}} \tag{5-32}$$

Figure 5-20 shows the power outputs of the original system without stiffness compensation and the proposed system with stiffness compensation.

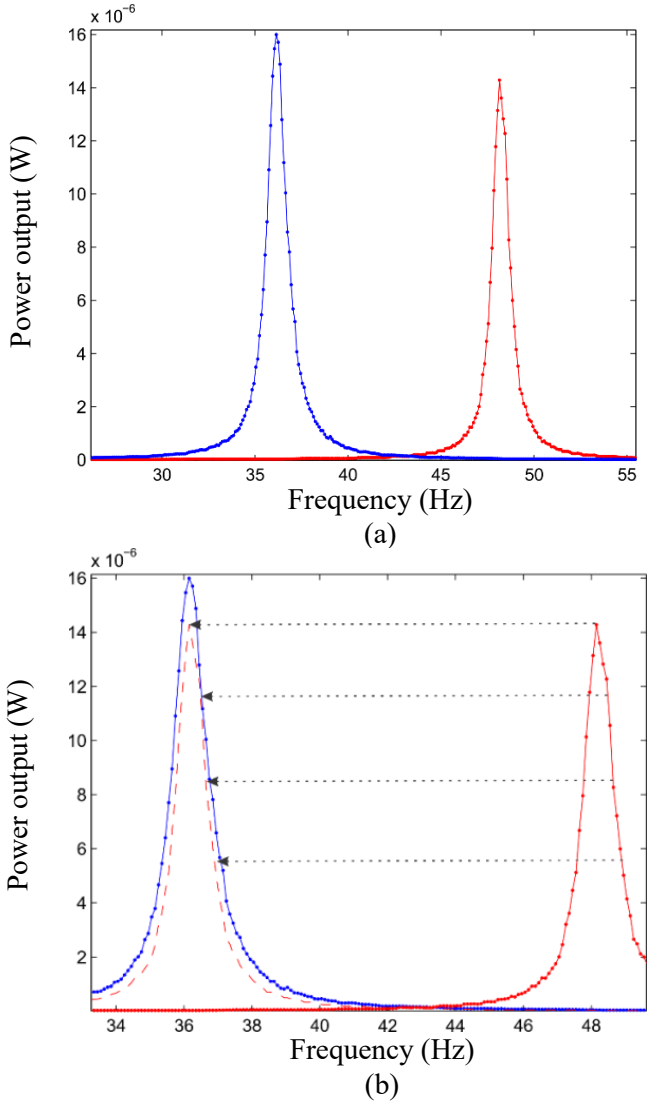

Figure 5-20. Power output with optimal resistant load. (a) power output; (b) direct comparison. with stiffness compensation; without stiffness compensation.

The base excitation level is 0.2 g. Without stiffness compensation, the maximum power output is 14.2 μW. With the stiffness compensation scheme proposed in this research, the maximum power output is increased to 16.05 μW. Figure 5-20b highlights the off-resonance performance comparison. It can be observed that the stiffness compensation scheme can also increase the power output at off-resonance frequencies. This is due to that the stiffness compensation can increase the electro-mechanical coupling coefficient at the device level.

5.4 Concluding Remarks

In this research, a scheme to improve the energy conversion capability of vibration-based piezoelectric energy harvester is developed. It is shown theoretically and experimentally that properly configured and positioned magnet elements can induce a linear magnetic field that yields negative stiffness. This scheme can effectively compensate the mechanical stiffness of the harvester and increase the electro-mechanical coupling at the device-level. Theoretical modeling, FEM simulation and experimental analysis are carried out to analyze the system. It's validated theoretically and experimentally that linear negative stiffness can be created to compensate the stiffness of the piezoelectric cantilever system. In this regard, the mechanical energy stored in the cantilever as well as the piezoelectric transducer can be reduced. This can improve the energy harvesting efficiency at both resonance and off-resonance situations. Experimental studies on a prototype show that electro-mechanical coupling factor can be increased by 65% with 44.1% stiffness compensated. Both the open-circuit voltage and the power output are enhanced.

Chapter 6 Piezoelectric Cantilever-Pendulum System for Multi-Directional Energy Harvesting

6.1 Introduction

In recent years, prolonging the power supply of portable and wireless apparatuses by harvesting ambient energy has received significant attention (Paradiso and Starner, 2005; Roundy et al, 2005; Mitcheson et al, 2008). Since vibration energy is virtually ubiquitous, utilizing piezoelectric devices to convert the vibration energy into electrical energy has emerged as one of the primary methods (Anton and Sodano, 2007; Priya, 2007; Khaligh et al, 2010). Piezoelectric transducers, possessing two-way electro-mechanical coupling, feature advantages of being compact, having high bandwidth and maintaining good linearity within its functional range. A typical piezoelectric energy harvester consists of a cantilever beam with a piezoelectric transducer bonded near its root and a proof-mass attached to its tip (Anton and Sodano, 2007; Priya, 2007; Khaligh et al, 2010; Ji et al, 2010; Xu et al, 2012). The proof-mass is adopted to tune the natural frequency of the beam and to enhance the vibration energy absorbing. This second-order dynamic system behaves optimally when its natural frequency matches the frequency of the excitation and the response direction is aligned with that of the excitation. In reality, however, ambient excitations have components in multiple directions, and may feature broad frequency bandwidth. For example, a device carried by a pedestrian is subject to accelerations in all three directions exhibiting aperiodic dynamics (Xu and Tang, 2015a). The power output of the traditional harvesters decreases significantly, if the excitation comes from directions other than the response direction or is off-resonance (Cottone et al, 2009; Shahruz, 2006; Ando et al, 2013; Su and Zu, 2013; Xu and Tang, 2015a).

There has been a stream of efforts to address the bandwidth limitation of simple harvesters. Typically, multi-resonances by a single harvester and nonlinearity induced by permanent magnet or internal resonance are adopted (Cottone et al, 2009; Shahruz, 2006; Wu et al, 2006; Tadesse et al, 2009; Erturk et al, 2009a; Erturk et al, 2009b; Vinod et al, 2008; Stanton et al, 2009; Jung and Yun, 2010; Zhou et al, 2013; Chen and Jiang, 2015). On the other hand, there are much less investigations that cope with

multi-directional excitations. Bartsch et al (2009) connected a disk shape mass to concentric circular springs, where the device can harvest vibration energy through electromagnetic conversion by utilizing the multi-dimensional motion of the mass. Yang et al (2013) studied a 2-dimensional vibration energy harvester based on the magnetostrictive transactions in a circular cross-section rod which can bend in different directions to generate power. For piezoelectric energy harvesting, existing studies are oftentimes based on multiple cantilevers. Ando et al (2013) reported a 2-dimensional piezoelectric energy harvester, in which two separate piezoelectric cantilevers are placed in different directions and coupled with magnetic interaction. Su and Zu (2013) further explored a tri-directional energy harvesting scheme. A discrete spring-mass oscillator is added and couples the two beams under the magnetic effect. In a more recent study (Chen et al, 2015), a dandelion-like generator was designed with many cantilevers assembled in different directions, where the cantilevers are sensitive in many directions and therefore this device can achieve multi-directional energy harvesting. Yang et al (2015) proposed a frame configured energy harvester which has vertical and horizontal vibration modes around one frequency point and is feasible for two-dimensional vibration energy harvesting.

Ideally, a multi-directional energy harvester with a single piezoelectric cantilever may have advantages of being compact and low-cost. The challenges for achieving such a design are presented as follows. One challenge is to induce beam bending motion based on excitations from all three directions. The most commonly used mode of the cantilever, the first bending mode, is sensitive to excitation along the bending direction only. Note that a single mass can have motion in 3-dimensional space and act as a dynamic amplifier (Aldraihem and Baz, 2011; Zhou et al, 2012; Tang and Yang, 2012). In this paper, we propose to replace the proof-mass used in simple cantilever by a pendulum. Our intention is to take advantage of the nonlinear coupling between the pendulum motion in multiple directions and the beam bending vibration (Xu and Tang, 2015b). Another challenge is to induce a primary resonance of beam bending motion under multi-directional excitations. As the device is designed for vibration energy harvesting, primary resonance of beam bending motion is needed to boost the efficiency. The power

output is limited when the harvester is working off-resonance or at sub-resonance. Our hypothesis here is that, by choosing proper parametric combination in the aforementioned piezoelectric cantilever-pendulum, we can induce internal resonance. Such internal resonance facilitates energy interchange between the primary resonance of beam vibration and the pendulum motion. In other words, the system is capable of transferring the input mechanical energy in different directions to the beam bending motion with high efficiency.

The rest of this section is organized as follows. In Section 6.2, the concept of the new design is outlined first. In Section 6.3, governing equations are derived based on Lagrange's equations and the key consideration for the 1:2 internal resonance is analyzed. Section 6.4 provides correlated experimental and numerical investigations for validation and insights. Concluding remarks are presented in Section 6.5.

6.2 Design Concept

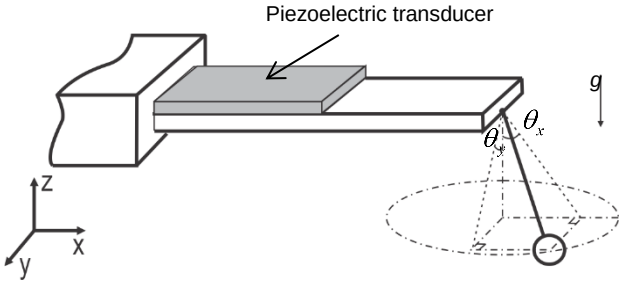

Figure 6-1. Schematics of the piezoelectric cantilever-pendulum system.

The configuration of the device is shown in Figure 6-1. The cantilever pendulum system is based on a single piezoelectric cantilever with a pendulum connected to its tip. The piezoelectric cantilever beam has a piezoelectric transducer bonded near the root. The pendulum is formed by a sphere-shaped mass and a wire which is considered massless and tensioned. The x-direction and the y-direction are along the beam length- and width- (horizontal) directions, respectively. The pendulum is hung in the *z*- (vertical) direction which is also the direction of gravity. Without loss of generality, we focus on the first bending

mode of the piezoelectric cantilever.

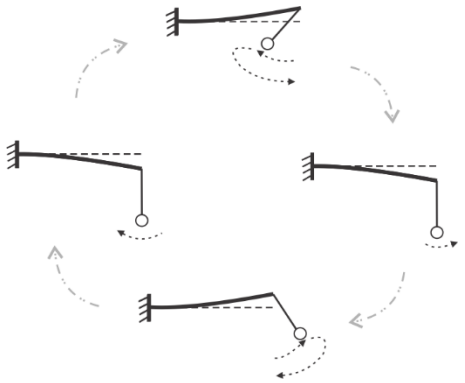

Figure 2. Conceptual illustration of the operational principle.

In a usual energy harvesting process, the excitation and beam bending motion are aligned in the same direction. The vibration energy of beam bending motion is converted into useful electrical energy through the electro-mechanical coupling of the piezoelectric transducer. Figure 6-2 illustrates the underlying physics of energy interchange between the beam bending motion and pendulum motion of the new device. In one cycle of the pendulum resonant motion where the pendulum moves forward and backward, the projection of the acceleration (e.g., acceleration due to centripetal effect) to the z-axis due to pendulum motion periodically varies two cycles. In other words, the frequency of the centripetal acceleration projection to z-axis is twice of that of the pendulum motion. Note that the beam bending motion is sensitive towards the z-direction acceleration. A primary resonance of beam vibration is induced, when the natural frequency of beam vibration is twice of that of the pendulum motion. In such a situation, the vibration energy in the horizontal direction can be effectively harvested by the beam vibration. It's worth noting that Figure 2 shows one possible pendulum motion that yields resonance of beam vibration. In practice, the pendulum may have motions in the *xz*-, *yz*- and *xy*-planes. These pendulum motions yield the capability of multi-directional energy harvesting.

6.3 Modeling of Piezoelectric Cantilever-Pendulum and fundamental Dynamic Characteristics

6.3.1 Mathematical model

In this section, a mathematical model is presented in order to analyze the piezoelectric cantilever pendulum system. Assumptions are made as follows: (1) the piezoelectric cantilever is considered as a composite Euler–Bernoulli beam; (2) the beam works at the first bending mode; (3) the wire of the pendulum is considered massless and tensioned during vibration; and (4) the system is excited by base-movements in all three directions.

We start from the Lagrange's equations,

$$\frac{d}{dt}\frac{\partial L}{\partial \dot{q}_i} - \frac{\partial L}{\partial q_i} = Q_i \tag{6-1}$$

where $L = T - U$, T is the kinetic energy, U is the potential energy of the system, q_i is the generalized displacement and Q_i denote the external force. Let the transversal deflection of the harvester beam at location x and time t be denoted as $w(x,t)$. The assumed-mode approach is adopted for analytical modeling, and we use only the first beam bending mode $\phi_1(x)$ to characterize the beam motion along the bending direction, i.e., $w(x,t) = \phi_1(x)q(t)$. As such, the generalized displacements include q, the projection of the angular displacement of the pendulum to the *xz*-plane, θ_x, and the projection of the angular displacement to the *yz*-plane, θ_y. The excitations from base-movements are included in the mechanical energy term, and the respective external force in Equation (6-1) thus is due to damping only.

The assumed mode used $\phi_1(x)$ is given by (Erturk et al, 2009b),

$$\phi_1(x) = C_1\left[\cos\frac{\lambda_1}{l_b}x - \cosh\frac{\lambda_1}{l_b}x + \varsigma_1\left(\sin\frac{\lambda_1}{l_b}x - \sinh\frac{\lambda_1}{l_b}x\right)\right] \tag{6-2}$$

where $\varsigma_1 = \dfrac{\sin\lambda_1 - \sinh\lambda_1}{\cos\lambda_1 + \cosh\lambda_1}$, and the eigenvalues λ_1 is solved from $\cos(\lambda_1 l_b)\cosh(\lambda_1 l_b) = -1$. In this research, harmonic base excitations with angular frequency Ω are considered. The base movements have components in all three directions with amplitudes, A_x, A_y and A_z, respectively,

$$u_x = A_x \cos\Omega t\,,\ u_y = A_y \cos\Omega t\,,\ u_z = A_z \cos\Omega t \tag{6-3a-c}$$

Let l_p, l_b, b, t_p, t_b, ρ_b and ρ_p represent, respectively, the length of the piezoelectric transducer, the length of the beam, the width of the composite cantilever, the thickness of the transducer, the thickness of the beam, the mass density of the beam, and the mass density of the transducer. The kinetic energy of the system can be derived as

$$\begin{aligned} T = {} & \frac{1}{2}\rho_b A_b \int_0^{l_b} \left(\dot{w}(x,t) + \dot{u}_z\right)^2 dx + \frac{1}{2}\rho_p A_p \int_0^{l_p} \left(\dot{w}(x,t) + \dot{u}_z\right)^2 dx + \frac{1}{2}\rho_b A_b \int_0^{l_b} \dot{u}_x{}^2 dx + \frac{1}{2}\rho_p A_p \int_0^{l_p} \dot{u}_x{}^2 dx + \frac{1}{2}\rho_b A_b \int_0^{l_b} \dot{u}_y{}^2 dx \\ & + \frac{1}{2}\rho_p A_p \int_0^{l_p} \dot{u}_y{}^2 dx + \frac{1}{2} m(\dot{w}(x,l_b) + \dot{u}_z + \dot{\theta} l \sin\theta)^2 + \frac{1}{2} m(\dot{\theta}_x l_x \cos\theta_x + \dot{u}_x)^2 + \frac{1}{2} m(\dot{\theta}_y l_y \cos\theta_y + \dot{u}_y)^2 \end{aligned} \tag{6-4}$$

where θ, l_x and l_y denote the angular displacement of the pendulum with respect to the *z*-axis, and the lengths of the pendulum projection to the *xz*-plane and *yz*-plane, respectively. Let *m* be the mass of the pendulum and *M* the modal mass of the cantilever. Let $A_b = bt_b$ and $A_p = bt_p$ represent, respectively, the cross sectional area of the beam and that of the piezoelectric transducer. The relations of θ, θ_x, θ_y, l_x and l_y can be obtained as

$$\theta = \arcsin\sqrt{\frac{\cos^2\theta_y \sin^2\theta_x + \cos^2\theta_x \sin^2\theta_y}{\cos^2\theta_x \cos^2\theta_y + \cos^2\theta_y \sin^2\theta_x + \cos^2\theta_x \sin^2\theta_y}}$$

$$l_x = \frac{l\cos\theta_y}{\sqrt{\cos^2\theta_x \cos^2\theta_y + \cos^2\theta_y \sin^2\theta_x + \cos^2\theta_x \sin^2\theta_y}} \tag{6-5a-c}$$

$$l_y = \frac{l\cos\theta_x}{\sqrt{\cos^2\theta_x \cos^2\theta_y + \cos^2\theta_y \sin^2\theta_x + \cos^2\theta_x \sin^2\theta_y}}$$

Meanwhile, the linear constitutive relation of piezoelectric transducer is (IEEE standard, 1987)

$$\begin{cases} \tau = E_p \varepsilon - h_{31} D \\ E = -h_{31}\varepsilon + \beta_{33} D \end{cases} \tag{6-6a, b}$$

where τ, ε, D and E represent, respectively, the stress, stain, electrical displacement (charge/area) and

electrical field (voltage/length) of the piezoelectric transducer, and E_p, h_{31} and β_{33} are the Young's modulus, piezoelectric constant and dielectric constant of the transducer. The potential energy of the entire system can be derived as

$$\begin{aligned} U &= U_b + U_p + Mgu_z + mg(w(x,l)+u_z) + mgl(1-\cos\theta) \\ &= \int_{V_b} \tau\varepsilon dV_b + \int_{V_p} (\tau\varepsilon + ED) dV_p + Mgu_z + mg(w(x,l)+u_z) + mgl(1-\cos\theta) \end{aligned} \tag{6-7}$$

After simple derivations, we can obtain the lumped coefficients of the system, such as mass of the piezoelectric cantilever, mechanical stiffness of the piezoelectric cantilever, capacitance and coupling term, respectively,

$$M = \rho_b A_b \int_0^{l_b} \phi_1^2 dx + \rho_p A_p \int_0^{l_p} \phi_1^2 dx$$

$$K = K_b + K_p = \int_0^{l_b} EI_b \left(\phi_1''\right)^2 dx + \int_0^{l_p} EI_p \left(\phi_1''\right)^2 dx \tag{6-8a-g}$$

$$C_p = \frac{(bl_p)^2}{\int_0^{l_p} A_p \beta_{33} dx}, \quad \chi = \int_0^{l_p} \frac{F_p h_{31} \phi_1''}{A_p \beta_{33}} dx .$$

where E_b is the Young's modulus of the beam, I_b and I_p represent the moments of inertia of the beam and the transducer, and F_p is the first moment of area of the transducer, respectively. Here the mode shape normalization condition $\phi_1(l_b) = 1$ is used to simplify the derivation. The piezoelectric transducer is simplified as a voltage source (Roundy et al, 2003). The governing equations of the systems are, with third- and higher-order terms omitted,

$$\begin{gathered} (M+m)\ddot{q} + c_1\dot{q} + Kq + ml(\dot{\theta}_x^2 + \theta_x\ddot{\theta}_x + \dot{\theta}_y^2 + \theta_y\ddot{\theta}_y - 6\theta_x\theta_y\dot{\theta}_x\dot{\theta}_y) + \chi V = -(M+m)a_z\cos(\Omega t) \\ l^2 m\ddot{\theta}_x + c_2\dot{\theta}_x + lm(g+\ddot{q})\theta_x + l^2 m\theta_x(\dot{\theta}_y^2 + \ddot{\theta}_y\theta_y) = -lm(a_x + \theta_x a_z)\cos(\Omega t) \\ l^2 m\ddot{\theta}_y + c_2\dot{\theta}_y + lm(g+\ddot{q})\theta_y + l^2 m\theta_y(\dot{\theta}_x^2 + \ddot{\theta}_x\theta_x) = -lm(a_y + \theta_y a_z)\cos(\Omega t) \\ C_p\dot{V} + V/R + \chi\dot{q} = 0 \end{gathered} \tag{6-9a-d}$$

where we define $a_x = -A_x\Omega^2$, $a_y = -A_y\Omega^2$, $a_z = -A_z\Omega^2$. In Equation (6-9), c_1 and c_2 are the mechanical damping terms of the beam bending motion and pendulum motion, respectively, C_p is the capacitance of

the piezoelectric transducer, R is the resistance load, χ is the electro-mechanical coupling of the transducer, and V is the voltage output. As shown, there is nonlinear coupling effect between the pendulum motion and the beam vibration. The nonlinear coupling exists even under low-amplitude vibration condition. It is worth mentioning that, in the past, dynamic stability, nonlinear normal modes (NNMs) and bifurcations have been investigated for 2-dimensional mass-spring-pendulum systems (Banerjee et al, 1995; Lee and Hsu, 1994; Wang et al, 2005; Haddow and Barr, 1984; Nayfeh and Zavodney, 1988; Nayfeh et al, 1989; Hatwal et al, 1986; Sheheitli and Rand, 2012). The internal resonance in such kind of systems facilitates the energy interchange among the involved modes. In this paper, our goal is to induce the resonance of beam bending motion based on multi-directional pendulum motions through the internal resonance.

6.3.2 Key Consideration for the 1:2 internal resonance

The system dynamics described by Equation (6-9) is complicated. It is reasonable to investigate only under specific load case (Cotton et al, 2009; Neiss et al, 2014). In the following analysis, the open circuit condition is considered. In general, the power output is proportional to the square of the voltage output when other parameters of the system are kept constant (Ferrari et al, 2010; Soliman et al, 2008; Erturk et al, 2009a). Under open circuit condition, the voltage output is proportional to the beam vibration response,

$$V_{\text{open}} = -\frac{\chi}{C_p} q \tag{6-10}$$

The governing equations of motion can be simplified as

$$\begin{aligned}
&\ddot{q} + \varepsilon\hat{\zeta}_1\omega_2\dot{q} + \omega_2^2 q + r_m l(\dot{\theta}_x^2 + \theta_x\ddot{\theta}_x + \dot{\theta}_y^2 + \theta_y\ddot{\theta}_y - 6\theta_x\theta_y\dot{\theta}_x\dot{\theta}_y) = -\varepsilon^2\hat{a}_z\cos\Omega t \\
&l\ddot{\theta}_x + \varepsilon\hat{\zeta}_2 l\dot{\theta}_x + (l\omega_1^2 + \ddot{q})\theta_x + l\theta_x(\dot{\theta}_y^2 + \ddot{\theta}_y\theta_y) = -\varepsilon^2(\hat{a}_x + \theta_x a_z)\cos\Omega t \\
&l\ddot{\theta}_y + \varepsilon\hat{\zeta}_2 l\dot{\theta}_y + (l\omega_1^2 + \ddot{q})\theta_y + l\theta_y(\dot{\theta}_x^2 + \ddot{\theta}_x\theta_x) = -\varepsilon^2(\hat{a}_y + \theta_y a_z)\cos\Omega t
\end{aligned} \tag{6-11a-c}$$

where $\omega_1^2 = \frac{g}{l}$, $\omega_2^2 = \frac{K}{M+m}$, $r_m = \frac{m}{M+m}$, $\varepsilon\hat{\zeta}_1 = \frac{c_1}{(M+m)\omega_0}$, $\varepsilon\hat{\zeta}_2 = \frac{c_2}{l^2 m}$, $\varepsilon^2\hat{a}_x = a_x$, $\varepsilon^2\hat{a}_y = a_y$ and $\varepsilon^2\hat{a}_z = a_z$.

They represent the natural frequency of pendulum motion, the natural frequency of the beam bending motion with pendulum mass, the mass ratio, the damping coefficients and the excitations, respectively. As shown in Equation (6-11a), the beam vibration is coupled with the pendulum motion through a coefficient $r_m l$. In other words, the coupling can be enhanced by increasing the mass ratio. The multiple-scale method is applied and ε is the small expansion parameter ($0 < \varepsilon \ll 1$). Since the system has strong nonlinearity, here we investigate small-scale displacements of the beam bending motion and pendulum motion,

$$q(t,\varepsilon) \simeq \varepsilon q_0(T_0,T_1) + \varepsilon^2 q_1(T_0,T_1)$$

$$\theta_x(t,\varepsilon) \simeq \varepsilon\theta_{x0}(T_0,T_1) + \varepsilon^2\theta_{x1}(T_0,T_1) \qquad \text{(6-12a-c)}$$

$$\theta_y(t,\varepsilon) \simeq \varepsilon\theta_{y0}(T_0,T_1) + \varepsilon^2\theta_{y1}(T_0,T_1)$$

where $\hat{q}_0$, $\hat{\theta}_{x0}$ and $\hat{\theta}_{y0}$ represent the primary beam vibration and pendulum motion, respectively, and $\hat{q}_1$, $\hat{\theta}_{x1}$ and $\hat{\theta}_{y1}$ denote the small-scale system dynamics. Define the new time scale as $T_r = \varepsilon^r t^r$. The time-derivatives are then expressed as

$$\frac{d}{dt} = D_0 + \varepsilon D_1, \quad \frac{d^2}{dt^2} = D_0^2 + 2\varepsilon D_0 D_1 \qquad \text{(6-13a, b)}$$

$$D_0 \equiv \partial/\partial T_0, \quad D_1 \equiv \partial/\partial T_1 \qquad \text{(6-14a, b)}$$

Substituting Equations (6-12-14) into Equation (6-11) and equating the terms in the same scales, we obtain the ε terms and ε^2 terms as, respectively

$$\begin{aligned} D_0^2 q_0 + \omega_2^2 q_0 &= 0 \\ D_0^2\theta_{x0} + \omega_1^2\theta_{x0} &= 0 \\ D_0^2\theta_{y0} + \omega_1^2\theta_{y0} &= 0 \end{aligned} \qquad \text{(6-15a-c)}$$

and

$$
\begin{aligned}
D_0^2 q_1 + \omega_2^2 q_1 &= -\left(2D_0 D_1 q_0 + l r_m \left((D_0 \theta_{x0})^2 + (D_0 \theta_{y0})^2 + \theta_{x0} D_0^2 \theta_{x0} + \theta_{y0} D_0^2 \theta_{y0}\right) + \hat{\varsigma}_1 \omega_2 D_0 q_0 + \hat{a}_z \cos \Omega t\right) \\
D_0^2 \theta_{x1} + \omega_1^2 \theta_{x1} &= -(2D_0 D_1 \theta_{x0} + \hat{\varsigma}_2 D_0 \theta_{x0} + 1/l\, \partial_{x0} D_0^2 q_0 + 1/l\, a_x \cos \Omega t) \\
D_0^2 \theta_{y1} + \omega_1^2 \theta_{y1} &= -(2D_0 D_1 \theta_{y0} + \hat{\varsigma}_2 D_0 \theta_{y0} + 1/l\, \partial_{y0} D_0^2 \hat{q}_0 + 1/l\, \hat{a}_y \cos \Omega t)
\end{aligned}
\qquad \text{(6-16a-c)}
$$

The solution to Equation (6-15) can be expressed as

$$
\begin{aligned}
\hat{q}_0 &= q_0(T_1) e^{i\omega_2 T_0} + \bar{q}_0(T_1) e^{-i\omega_2 T_0} \\
\hat{\theta}_{x0} &= \theta_{x0}(T_1) e^{i\omega_1 T_0} + \bar{\theta}_{x0}(T_1) e^{-i\omega_1 T_0} \\
\hat{\theta}_{y0} &= \theta_{y0}(T_1) e^{i\omega_1 T_0} + \bar{\theta}_{y0}(T_1) e^{-i\omega_1 T_0}
\end{aligned}
\qquad \text{(6-17a-c)}
$$

where $\bar{q}_0(T_1)$, $\bar{\theta}_{x0}(T_1)$ and $\bar{\theta}_{y0}(T_1)$ denote the complex conjugates of the respective terms, respectively. $q_0(T_1)$, $\theta_{x0}(T_1)$ and $\theta_{y0}(T_1)$ are complex functions of T_1, and will be determined at the next level of approximation. Substituting Equation (6-17) into Equation (6-16) yields

$$
\begin{aligned}
D_0^2 q_1 + \omega_2^2 q_1 &= -\left(i2e^{i\omega_2 T_0} \omega_2 D_1 q_0 - 2l r_m \omega_1^2 \left(\theta_{x0}^2 + \theta_{y0}^2\right) e^{2i\omega_1 T_0} + i\hat{\varsigma}_1 \omega_2^2 q_0 e^{i\omega_2 T_0} + \frac{\hat{a}_z}{2} e^{i\Omega T_0} + \text{cc}\right) \\
D_0^2 \theta_{x1} + \omega_1^2 \theta_{x1} &= -\frac{1}{l}(i2l\omega_1 D_1 \theta_{x0} e^{i\omega_1 T_0} + i\hat{\varsigma}_2 l\omega_1 \theta_{x0} e^{i\omega_1 T_0} - e^{i(\omega_2+\omega_1)T_0} \omega_2^2 \theta_{x0} q_0 - e^{i(\omega_2-\omega_1)T_0} \omega_2^2 \bar{\theta}_{x0} q_0 + \frac{\hat{a}_x}{2} e^{i\Omega T_0} + \text{cc}) \quad \text{(6-} \\
D_0^2 \hat{\theta}_{y1} + \omega_1^2 \hat{\theta}_{y1} &= -\frac{1}{l}(i2l\omega_1 D_1 \theta_{y0} e^{i\omega_1 T_0} + i\hat{\varsigma}_2 l\omega_1 \theta_{y0} e^{i\omega_1 T_0} - e^{i(\omega_2+\omega_1)T_0} \omega_2^2 \theta_{y0} q_0 - e^{i(\omega_2-\omega_1)T_0} \omega_2^2 \bar{\theta}_{y0} q_0 + \frac{\hat{a}_y}{2} e^{i\Omega T_0} + \text{cc})
\end{aligned}
$$

18a-c)

where, for simplicity, we use "cc" to represent the complex conjugate of the terms preceding it.

Equation (6-18) indeed illustrates possible resonance and internal resonance. To eliminate the secular terms, the coefficients of terms of $e^{i\omega_1 T_0}$ or $e^{i\omega_2 T_0}$ should be zero (Nayfeh and Zavodney, 1988; Wang et al, 2005). As shown in Equation (18a), when Ω is in the vicinity of ω_2, the summation of all coefficients of $e^{i\omega_2 T_0}$ must be zero, which yields that the beam motion q_0 is linearly related to the excitation $\hat{a}_z$. This indicates that a primary resonance of beam bending motion can be excited under the z-direction excitation $\hat{a}_z$ at ω_2. This resonant condition is the same as that for a traditional cantilever. Similarly, as shown in Equation (6-18b) and Equation (6-18c), there are resonances of the pendulum motion when the

excitations $\hat{a}_x$ and $\hat{a}_y$ are applied around ω_1.

Observing Equation (6-18), one can further identify that, when $\omega_2 \approx 2\omega_1$, there exists strong coupling between the beam vibration and the pendulum motion. On the other hand, the terms of q_0, θ_{x0} and θ_{y0} tend to be independent when ω_2 is far away from $2\omega_1$. The pendulum motion may induce sub-resonance of beam vibration only. Therefore, in order to enhance energy harvesting capability under the *x*- and *y*-direction excitations, a key design consideration is that $\omega_2 \approx 2\omega_1$, which is the condition of 1:2 internal resonance. It is also worth noting that, with the 1:2 internal resonance, the pendulum motion θ_{x0} and θ_{y0} and the beam vibration q_0 are on the same order, i.e., the energy interchange would be quite efficient.

In the following analysis, we assume that the system meets the key condition of internal resonance. The resonant conditions are

$$2\omega_1 = \omega_2 + \varepsilon\sigma_1, \ \Omega = \omega_r + \varepsilon\sigma_2 \tag{6-19a, b}$$

where σ_1 is the internal detuning parameter, σ_2 is the external detuning parameter (frequency of excitation) and r = 1 or 2.

6.3.3 Solution of response under the x-direction excitation

Here we first investigate the response/solution under the *x*-direction excitation. The excitations in the *y*- and *z*-direction are not taken into account. At first, the resonant conditions under the x-direction excitation are

$$\Omega = \omega_1 + \varepsilon\sigma_2, \ 2\omega_1 = \omega_2 + \varepsilon\sigma_1 \tag{6-20a, b}$$

Substituting Equation (6-20) into (6-18), the solvability condition, i.e., eliminating the secular terms in Equation (6-18), yields the following equations

$$
\begin{aligned}
&i2\omega_2 D_1 q_0 - 2lr_m\omega_1^2\left(\theta_{x0}^2+\theta_{y0}^2\right)e^{i\varepsilon\sigma_1 T_0} + i\hat{\varsigma}_1\omega_2^2 q_0 = 0\\
&i2l\omega_1 D_1\theta_{x0} + i\hat{\varsigma}_2 l\omega_1\theta_{x0} - e^{-i\varepsilon\sigma_2 T_0}\omega_2^2\overline{\theta}_{x0}q_0 + \frac{\hat{a}_x}{2}e^{i\varepsilon\sigma_2 T_0} = 0\\
&i2l\omega_1 D_1\theta_{y0} + i\hat{\varsigma}_2 l\omega_1\theta_{y0} - e^{-i\varepsilon\sigma_2 T_0}\omega_2^2\overline{\theta}_{y0}q_0 = 0
\end{aligned}
\tag{6-21a-c}
$$

To simplify notations, we introduce the polar forms,

$$
q_0 = \frac{a(T_1)}{2}e^{i\varphi_1(T_1)},\ \theta_{x0} = \frac{b(T_1)}{2}e^{i\varphi_2(T_1)},\ \theta_{y0} = \frac{c(T_1)}{2}e^{i\varphi_3(T_1)} \tag{6-22a-c}
$$

where a, b, c, φ_1, φ_2, and φ_3 are real functions of time T_1. We then obtain, after separating the real and imaginary parts,

$$
\begin{aligned}
D_1 a &= -\frac{lr_m\omega_1^2\left(b^2\sin\beta_1 + c^2\sin\beta_2\right) + \hat{\varsigma}_1\omega_2^2 a}{2\omega_2}\\
D_1 b &= -\frac{2\hat{\varsigma}_2\omega_1 lb - \omega_2^2 ab\sin\beta_1 + 2\hat{a}_x\sin\beta_3}{4\omega_1 l}\\
D_1 c &= -\frac{2\hat{\varsigma}_2\omega_1 lc - \omega_2^2 ac\sin\beta_2}{4\omega_1 l}\\
D_1\varphi_1 &= -\frac{lr_m\omega_1^2\left(b^2\cos\beta_1 + c^2\cos\beta_2\right)}{2\omega_2 a}\\
D_1\varphi_2 &= -\frac{\omega_2^2 ab\cos\beta_1 - 2\hat{a}_x\cos\beta_3}{4\omega_1 lb}\\
D_1\varphi_3 &= -\frac{\omega_2^2 a\cos\beta_2}{4\omega_1 l}
\end{aligned}
\tag{6-23a-f}
$$

where $\beta_1 = \varphi_1 - 2\varphi_2 - \sigma_1 T_1$, $\beta_2 = \varphi_1 - 2\varphi_3 - \sigma_1 T_1$, $\beta_3 = \sigma_2 T_1 - \varphi_2$. Of special interest is the steady-state response. We then have the derivatives of the amplitudes and phases $D_1 a = 0$, $D_1 b = 0$, $D_1 c = 0$, $D_1\beta_1 = 0$, $D_1\beta_2 = 0$ and $D_1\beta_3 = 0$. For the derivatives of the phases we have

$$
D_1\varphi_1 = 2\sigma_2 + \sigma_1,\ D_1\varphi_2 = \sigma_2,\ D_1\varphi_3 = \sigma_2 \tag{6-24a-c}
$$

Substituting Equation (6-24) back into Equation (6-23), we can simplify the solvability condition as

$$
\begin{gathered}
lr_m\omega_1^2\left(b^2\sin\beta_1+c^2\sin\beta_2\right)+\hat{\varsigma}_1\omega_2^2 a=0\\
2\hat{\varsigma}_2\omega_1 lb-\omega_2^2 ab\sin\beta_1+2\hat{a}_x\sin\beta_3=0\\
2\hat{\varsigma}_2\omega_1 lc-\omega_2^2 ac\sin\beta_2=0\\
2\omega_2 a\left(2\sigma_2+\sigma_1\right)+lr_m\omega_1^2\left(b^2\cos\beta_1+c^2\cos\beta_2\right)=0\\
4\omega_1 lb\sigma_2+\omega_2^2 ab\cos\beta_1-2\hat{a}_x\cos\beta_3=0\\
4\omega_1 l\sigma_2+\omega_2^2 a\cos\beta_2=0
\end{gathered}
\qquad \text{(6-25a-f)}
$$

Here we are interested in the response of beam bending motion through which the piezoelectric transducer converts the mechanical energy into electrical power. The beam bending motion is given as

$$
\left(\hat{\varsigma}_2\omega_1 lb+\frac{\hat{\varsigma}_1\omega_2^4 a^2+2\varsigma_2 r_m l^2\omega_1^3 c^2}{2lr_m\omega_1^2 b}\right)^2+\left(2\omega_1 lb\sigma_2-\frac{\omega_2^3 a^2\left(2\sigma_2+\sigma_1\right)}{lr_m\omega_1^2 b}+\frac{2\omega_1 l\sigma_2 c^2}{b}\right)^2=\hat{a}_x^2 \qquad \text{(6-26)}
$$

The possible solutions include 1) $b\neq 0$, $a=c=0$; 2) $b\neq 0$, $a\neq 0$, $c=0$; 3) $b\neq 0$, $c\neq 0$, $a=0$; and 4) $b\neq 0$, $a\neq 0$, $c\neq 0$. The solutions with $a\neq 0$ indicates that the x-direction excitation indeed induces the beam vibration that generates power. It is worth noting that for this system, the solutions with beam vibration $a\neq 0$ exist under extremely low amplitude excitations. This point will be further discussed later. The response under *y*-direction excitation follows the same characteristics.

6.3.4 Solution of response under the z-direction excitation

We then investigate the response/solution under the *z*-direction excitation. The excitations in the x- and y-directions are not taken into account. The resonant conditions are

$$
\Omega=\omega_2+\varepsilon\sigma_2,\ 2\omega_1=\omega_2+\varepsilon\sigma_1 \qquad \text{(6-27a, b)}
$$

Substituting Equation (6-27) into Equation (6-18), we can derive the solvability condition as

$$
\begin{gathered}
\hat{a}_z e^{i\varepsilon\sigma_2 T_0}+i4\omega_2 D_1 q_0-4lr_m\omega_1^2\left(\theta_{x0}^2+\theta_{y0}^2\right)e^{i\varepsilon\sigma_1 T_0}+i2\hat{\varsigma}_1\omega_2^2 q_0=0\\
i2l\omega_1 D_1\theta_{x0}+i\hat{\varsigma}_2 l\omega_1\theta_{x0}-e^{-i\varepsilon\sigma_1 T_0}\omega_2^2\bar{\theta}_{x0}q_0=0\\
i2l\omega_1 D_1\theta_{y0}+i\hat{\varsigma}_2 l\omega_1\theta_{y0}-e^{-i\varepsilon\sigma_1 T_0}\omega_2^2\bar{\theta}_{y0}q_0=0
\end{gathered}
\qquad \text{(6-28a-c)}
$$

We again introduce the polar forms,

$$q_0 = \frac{a(T_1)}{2} e^{i\varphi_1(T_1)},\ \theta_{x0} = \frac{b(T_1)}{2} e^{i\varphi_2(T_1)},\ \theta_{y0} = \frac{c(T_1)}{2} e^{i\varphi_3(T_1)} \tag{6-29a-c}$$

which yield

$$\begin{aligned}
D_1 a &= -\frac{l r_m \omega_1^2 \left(b^2 \sin\beta_1' + c^2 \sin\beta_2'\right) + \hat{\varsigma}_1 \omega_2^2 a + \hat{a}_z \sin\beta_3'}{2\omega_2} \\
D_1 b &= \frac{\omega_2^2 ab \sin\beta_1' - 2\hat{\varsigma}_2 \omega_1 lb}{4\omega_1 l} \\
D_1 c &= \frac{\omega_2^2 ac \sin\beta_2' - 2\hat{\varsigma}_2 \omega_1 lc}{4\omega_1 l} \\
D_1 \varphi_1 &= \frac{\hat{a}_z \cos\beta_3' - l r_m \omega_1^2 \left(b^2 \cos\beta_1' + c^2 \cos\beta_2'\right)}{2\omega_2 a} \\
D_1 \varphi_2 &= -\frac{\omega_2^2 a \cos\beta_1'}{4\omega_1 l} \\
D_1 \varphi_3 &= -\frac{\omega_2^2 a \cos\beta_2'}{4\omega_1 l}
\end{aligned} \tag{6-30a-f}$$

where $\beta_1' = \varphi_1 - 2\varphi_2 - \sigma_1 T_1, \beta_2' = \varphi_1 - 2\varphi_3 - \sigma_1 T_1, \beta_3' = \sigma_1 T_1 - \varphi_1$. Consider steady-state response. We have the derivatives of the amplitudes and phases as $D_1 a = 0$, $D_1 b = 0$, $D_1 c = 0$, $D_1 \beta_1' = 0$, $D_1 \beta_2' = 0$ and $D_1 \beta_3' = 0$. For the derivatives of the phases, we have

$$D_1 \varphi_1 = \sigma_1,\ D_1 \varphi_2 = \frac{\sigma_2 - \sigma_1}{2},\ D_1 \varphi_3 = \frac{\sigma_2 - \sigma_1}{2} \tag{6-31a-c}$$

Substituting Equation (6-31) into Equation (6-30), we can simplify the solvability condition,

$$\begin{aligned}
l r_m \omega_1^2 \left(b^2 \sin\beta_1' + c^2 \sin\beta_2'\right) + \hat{\varsigma}_1 \omega_2^2 a + \hat{a}_z \sin\beta_3' &= 0 \\
\omega_2^2 ab \sin\beta_1' - 2\hat{\varsigma}_2 \omega_1 lb &= 0 \\
\omega_2^2 ac \sin\beta_2' - 2\hat{\varsigma}_2 \omega_1 lc &= 0 \\
2\omega_2 a\sigma_2 + l r_m \omega_1^2 \left(b^2 \cos\beta_1' + c^2 \cos\beta_2'\right) - \hat{a}_z \cos\beta_3' &= 0 \\
-2\omega_1 l(\sigma_1 - \sigma_2) + \omega_2^2 a \cos\beta_1' &= 0 \\
-2\omega_1 l(\sigma_1 - \sigma_2) + \omega_2^2 a \cos\beta_2' &= 0
\end{aligned} \tag{6-33a-f}$$

The response of the beam bending motion is given as

$$\left(\frac{2\hat{\varsigma}_2 r_m l^2 \omega_1^3}{\omega_2^2 a}\left(b^2 + c^2\right) + \hat{\varsigma}_1 \omega_2^2 a\right)^2 + \left(2\omega_2 a\sigma_2 + \frac{2 r_m l^2 \omega_1^3 (\sigma_1 - \sigma_2)}{\omega_2^2 a}\left(b^2 + c^2\right)\right)^2 = \hat{a}_z^2 \tag{6-34}$$

Here, the direction of the excitation is aligned with the direction of beam vibration. The possible solution types include 1) $a \neq 0$, $b = c = 0$; 2) $a \neq 0$, $b \neq 0$, $c = 0$; 3) $a \neq 0$, $c \neq 0$, $b = 0$; and 4) $a \neq 0$, $b \neq 0$, $c \neq 0$. For all these solutions, the beam bending motion is excited which enables power generation. It is worth pointing out that the frequency response of the beam vibration is given when $a \neq 0$ and $b = c = 0$,

$$\left(\hat{\varsigma}_1 \omega_2^2 a\right)^2 + \left(2\omega_2 a \sigma_2\right)^2 = \hat{a}_z^2 \tag{35}$$

In such a situation the response of the beam vibration yields that of a second order system. Due to the nonlinear coupling between the beam vibration and pendulum motion, we may also have other solutions such as those shown above as Type 2, Type 3, and Type 4. These solutions indicate that the *z*-direction excitation may also induce pendulum motions. In other words, the mechanical energy of beam bending motion may flow to the pendulum motion.

6.4 Validation and Discussion

6.4.1 Simulation and experimental set-up

Simulation and experiment are carried out to validate the concept. The parameters of the system are provided in Table 1. They are chosen such that the cantilever-pendulum system exhibits the 1:2 internal resonance. Specifically, the pendulum has a resonant frequency of 4.56 Hz that is half of the beam natural frequency 9.13 Hz. In this prototype we have a relatively large pendulum mass ($r_m = 0.93$) for enhanced coupling between the beam vibration and the pendulum motion. The simulations are carried out based on the algebraic solutions presented in the preceding section. Since the beam deflection results in an angular displacement at the tip and the pendulum is attached by using glue, there is minor difference between the *xz*- and *yz*-plane pendulum motions. An internal detuning parameter on the order of ε^2 is added to the resonant frequency of Equation (6-11b) in the simulation. Moreover, small random numbers are added as perturbations in the simulation for beam vibration, pendulum motion in *x*- and *y*-directions,

respectively.

Table 1. Parameters used in simulation and experiment

Parameters	Value
Host beam size (mm^3)	115.25 × 5.28 × 0.45
PZT sheet size (mm^3)	24.71 × 5.28 × 0.25
Radius of pendulum ball (mm)	5.53
Length of the copper wire (mm)	7.91
Density of the host beam ρ_p (kg/m^3)	7500
Density of the piezoelectric transducer ρ_p (kg/m^3)	7900
Young's Modulus of the host beam E_b (GPa)	109
Young's Modulus of the piezoelectric transducer E_p (GPa)	106
Piezoelectric coefficient d_{31} (pC/N)	-320
Piezoelectric strain coefficient h_{31} (N/C)	5.9×10^8
β_{33} (Vm/C)	2.92×10^8

The experimental set-up is shown in Figure 6-3. A piezoelectric transducer PZT-5H (Piezo Systems Inc.) is attached to the root of the cantilever by using epoxy glue (DP100). The pendulum, made of an iron sphere, is tied to the tip of the beam with a thin copper wire. The piezoelectric cantilever-pendulum is clamped onto a base attached to a 250 lb shaker driven through a 2000 W power amplifier. The base can be mounted to the shaker in all three *x*-, *y*-, and *z*-directions to receive excitations. The resulting peak-to-peak voltage output of the piezoelectric transducer is measured by an oscilloscope probe with an input impedance of 10 MΩ through dSPACE (DS1103) with sampling rate 20 kHz. The base movements, beam vibration and pendulum displacements are measured by proximity sensors (3300XL, Bently Nevada). While forward and reverse frequency sweep responses were acquired under sinusoidal

base excitations in different directions as specified (0.00107 Hz/s), all the simulation and experiment were performed with constant accelerations.

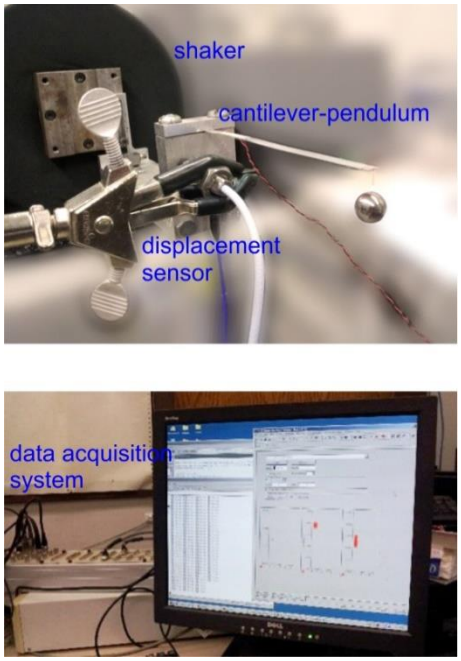

Figure 6-3. Experimental setup.

6.4.2 Energy interchange due to internal resonance

The key of the new multi-directional energy harvester design is the internal resonance created. One representative example is presented here to illustrate the energy interchange occurring between beam bending motion and pendulum motion, as shown in Figure 6-4 (simulation) and Figure 6-5 (experiment). The data is obtained in the vicinities of ω_1 and ω_2 with excitations applied in the *x*-direction and *z*-direction, respectively. A specific situation is selected that the pendulum motion is in *xz*-plane for the convenience of measurement. It can be observed in both figures that the beam vibration and the pendulum motion dominate the response alternately. This indicates a strong coupling between the beam vibration and the pendulum motion with significant energy interchange. Consequently, the mechanical energy from horizontal and vertical excitations can be effectively applied to the beam bending motion that generates power. The measured response agrees with the simulation well.

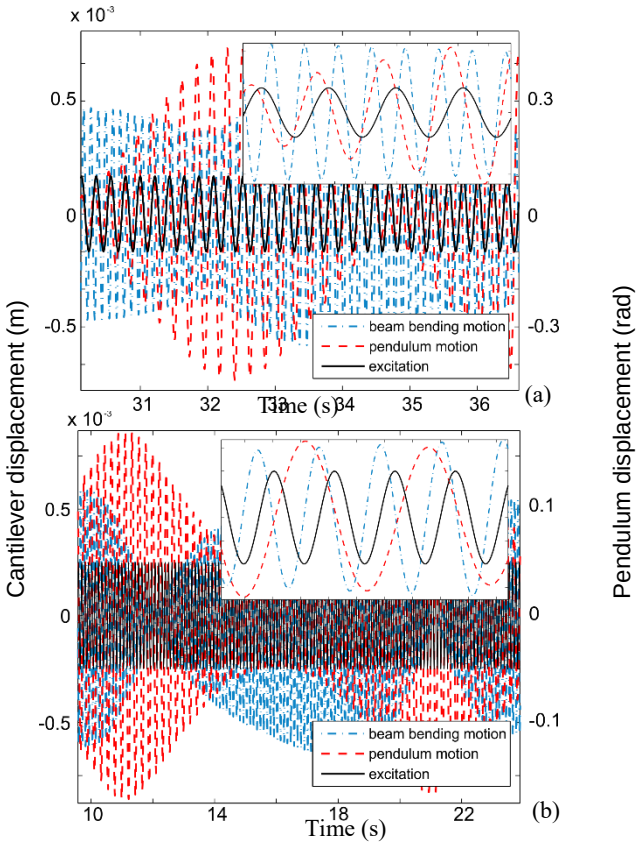

Figure 6-4. The 1:2 internal resonance with energy interchange (Simulation). a) Response at ω_1 subjected to *x*-direction excitation; b) Response at ω_2 subjected to *z*-direction excitation.

In this example, we have the energy interchange with amplitude-modulated motions. The pattern of the motion is dependent on the stability of the system dynamics. More specifically, the patterns may include steady-state, amplitude-modulated or chaotic motions. Moreover, it can be observed that the internal resonance couples the resonance of beam vibration and pendulum motion. Therefore, the frequency of the beam vibration is approximately twice of that of the pendulum motion. In other words, the voltage output is in the vicinity of a single frequency point ω_2 under excitations around both the dominant resonant frequencies ω_1 and ω_2. This phenomenon benefits the power output since the piezoelectric transducer impedance is frequency dependent.

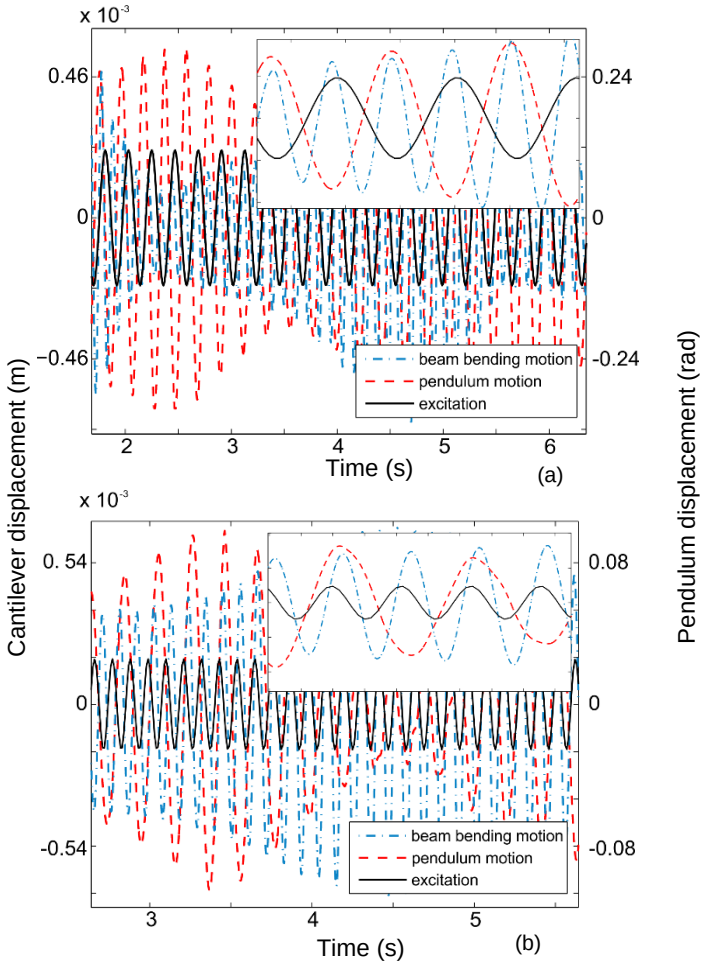

Figure 6-5. The 1:2 internal resonance with energy interchange (experiment). a) Response at ω_1 subjected to *x*-direction excitation; b) Response at ω_2 subjected to *z*-direction excitation.

6.4.3 Response characteristics under the x-direction excitation

In this sub-section, frequency responses are examined under the *x*-direction excitation in the vicinity of ω_1.

In this case, the direction of excitation is aligned with the direction of the *xz*-plane pendulum motion (θ_x) and perpendicular to that of the beam vibration. Figure 6-6 shows the simulation result of the forward frequency sweep responses of the open-circuit voltage output (peak-peak) and the pendulum motions. It can be observed from Figure 6-6b that the *xz*-plane pendulum motion is induced with multiple peaks.

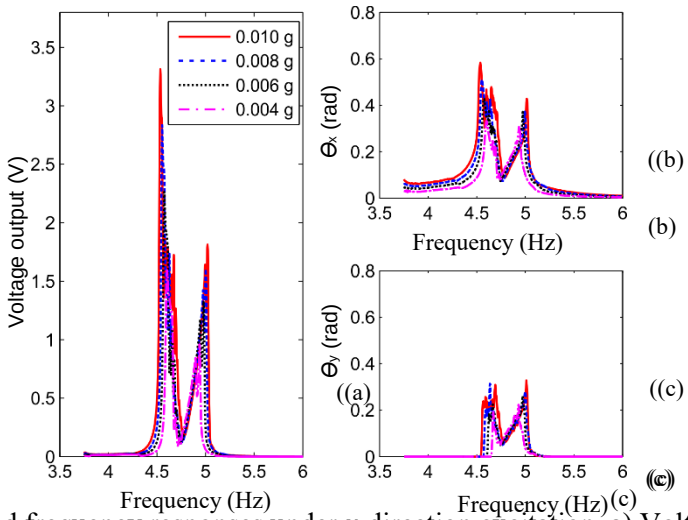

Figure 6-6. Simulated frequency responses under *x*-direction excitation. a) Voltage output versus excitation frequency; b) *xz*-plane pendulum motion; c) *yz*-plane pendulum motion.

The corresponding pendulum modes at the peaks can be obtained from the pendulum motion projected to the *xy*-plane, as shown in Figure 6-7.

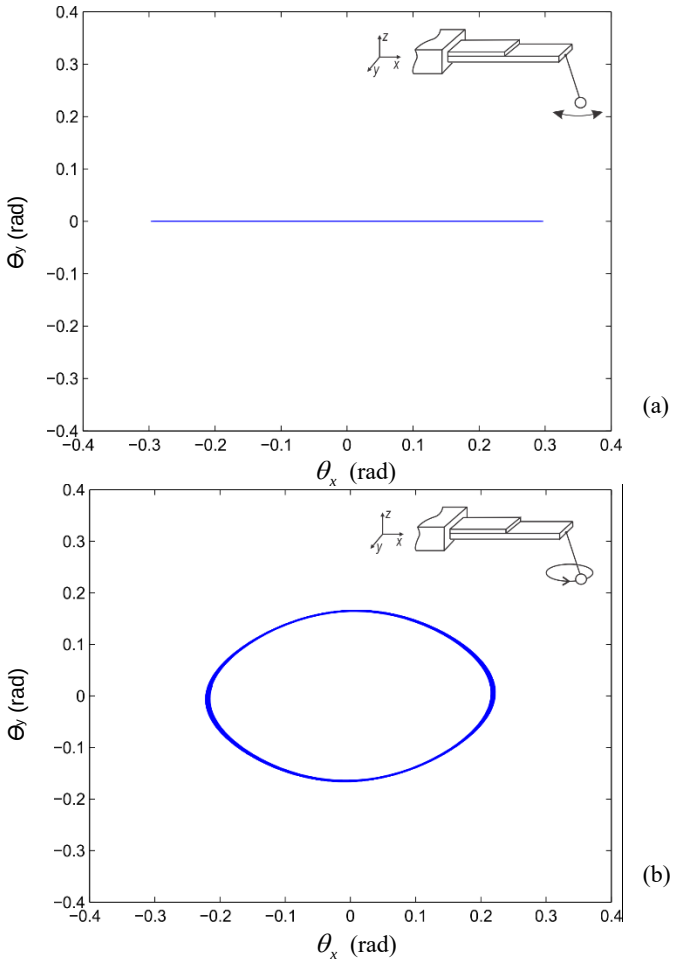

(b)

Figure 6-7. Pendulum motion projected to *xy*-plane under *x*-direction excitation (simulation). a) Pendulum motion around 4.5 Hz; b) Pendulum motion around 4.9 Hz.

For example, the pendulum motion is associated with the *xz*-plane pendulum mode (Figure 6-7a) in the vicinity of 4.5 Hz. It is worth mentioning that the *xz*-plane pendulum mode contains small-amplitude motion in the θ_y direction (Figure 6-7a) since perturbations are introduced into the simulation. Meanwhile, as a unique feature of this design (compared with the 2-dimensional mass-spring-pendulum system (Banerjee et al, 1995; Lee and Hsu, 1994; Wang et al, 2005)), a *yz*-plane pendulum motion θ_y is excited under the *x*-direction excitation around 4.9 Hz. It is also worth noting that the combination of *xz*- and *yz*-plane pendulum motion resembles a *xy*-plane pendulum mode (Figure 6-7b). The resonant frequencies of the *xz*- and *xy*-plane pendulum modes can be estimated as

$$\omega_{p1} \approx \sqrt{\frac{g}{l}}(1-\frac{1}{16}\theta_A^2) \tag{6-36}$$

$$\omega_{p2} \approx \sqrt{\frac{g}{l}}(1+\frac{1}{4}\theta_A^2) \tag{6-37}$$

which are θ_A (amplitude)-dependent. Here θ_A denotes the angular displacement amplitude of the pendulum with respect to the z-axis. In general, ω_{p1} is lower than ω_{p2}. As excitation and response amplitude increase, ω_{p1} decreases while ω_{p2} increases, which can be observed in Figure 6-6b and Figure 6cc. For example, for the responses under 0.006 g excitation we have $\omega_{p1} = 4.57$ Hz and $\omega_{p2} = 4.95$ Hz, respectively. When the excitation level is increased to 0.010 g, the two frequencies are changed into 4.54 Hz and 5.01 Hz, respectively.

The response of beam bending motion results from the combined effect of the 1:2 internal resonance and the pendulum motion characteristics. The beam bending resonance is induced due to the pendulum resonant motion at ω_{p1} and ω_{p2}. Note that the open circuit voltage output of the piezoelectric transducer is proportional to the beam vibration responses as indicated by Equation (6-10). Multiple peaks of voltage output can be observed in the vicinity of 4.5 Hz and 4.9 Hz (Figure 6-6a). At these peaks the

mechanical energy from the original pendulum motion flows to the beam vibration that generates power. For example, the voltage output has peaks of 3.42 V and 1.79 V under excitation of 0.010 g.

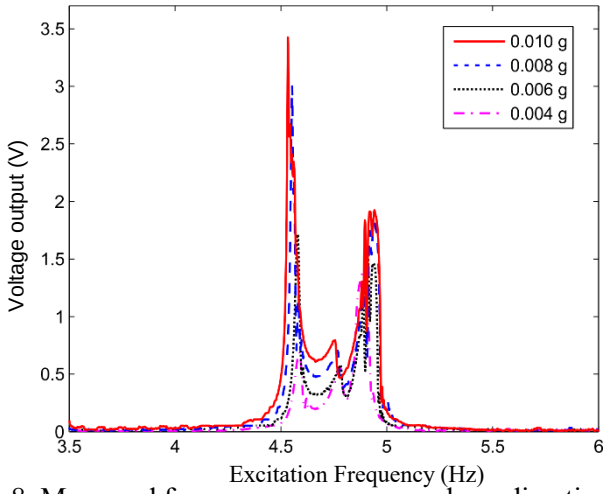

Figure 6-8. Measured frequency responses under *x*-direction excitation.

The experimental results validate the response simulation. As shown in Figure 6-8, the two corresponding peaks of voltage output in the vicinity of 4.5 Hz and 4.9 Hz can be observed. For example, the frequency response has two peaks of 3.37 V and 1.88 V under excitation of 0.010 g. This indicates that the prototype has significant power output when subjected to horizontal excitations. Due to limitation of the sensor, large pendulum motion in 3-dimensional space is not recorded. Nevertheless, experimental observations have confirmed the involved pendulum modes at the peaks. Overall, the simulation and the experiment match well.

As the frequency sweep direction is another key influencing factor towards the responses, in Figure 6-9 we compare the forward and reverse sweep frequency responses under the x-direction excitation of 0.008 g. It can be observed that the response of reverse frequency sweep has minor difference with respect to that under forward frequency sweep. Both the simulation and the experimental result under the reverse frequency sweep exhibits additional peaks due to bifurcations.

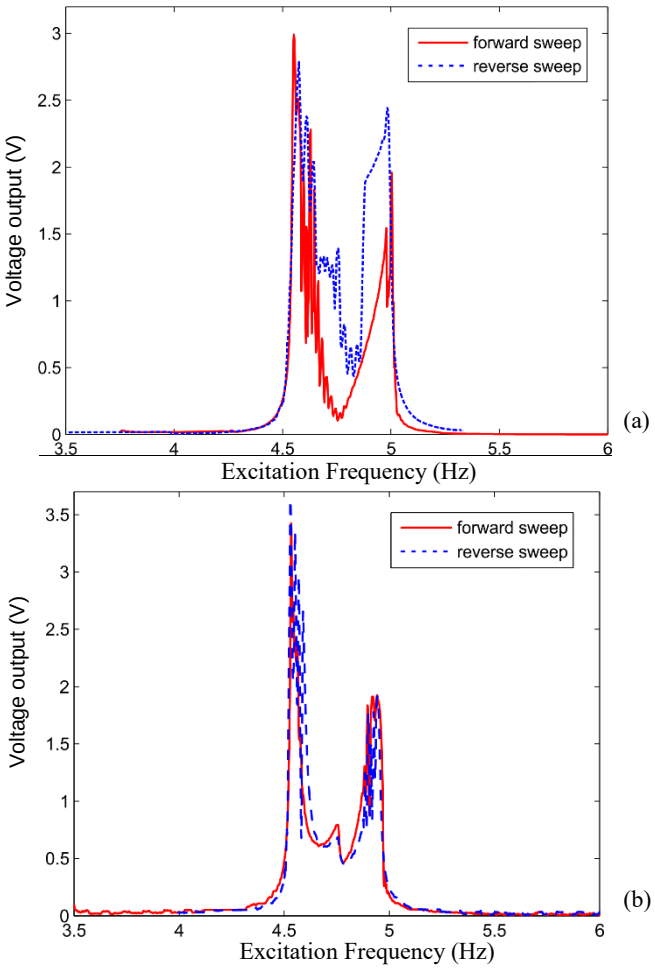

Figure 6-9. Frequency responses under *x*-direction excitation. a) Simulation; b) Measured response.

Of special interest is the peak of voltage output. Here we plot the voltage output versus frequency and excitation level in Figure 6-10. Figure 6-10a shows the simulation result of 3-dimensional plot of the voltage output under forward frequency sweep. Figure 6-10b shows the comparison of simulated and measured voltage outputs at the peaks versus excitations. It can readily be observed that the voltage output around 4.5 Hz is effectively excited in the entire range of excitation accelerations. Meanwhile, the peak around 4.9 Hz occurs due to bifurcation when excitation acceleration increases beyond 0.0025 g. It should be noted that these horizontal excitations applied are quite small (i.e., lower than 0.010 g). Although we may have response solutions without beam bending motion under the *x*-direction excitation, the beam vibration is effectively excited due to the energy interchange even under horizontal excitations with low levels. This indicates that that portion of mechanical energy can be efficiently harvested. This

phenomenon is not unusual. As reported in an L-shape cantilever system with 1:2 internal resonance, the mechanical energy interchange occurs under extremely low level excitations around the natural frequency of the first mode (Nayfeh et al, 1989). Furthermore, it can also be observed that the voltage outputs at the peaks are increased with the increase of excitation level in the entire range. The responses under *y*-direction excitations follow the similar characteristics, and therefore are not plotted.

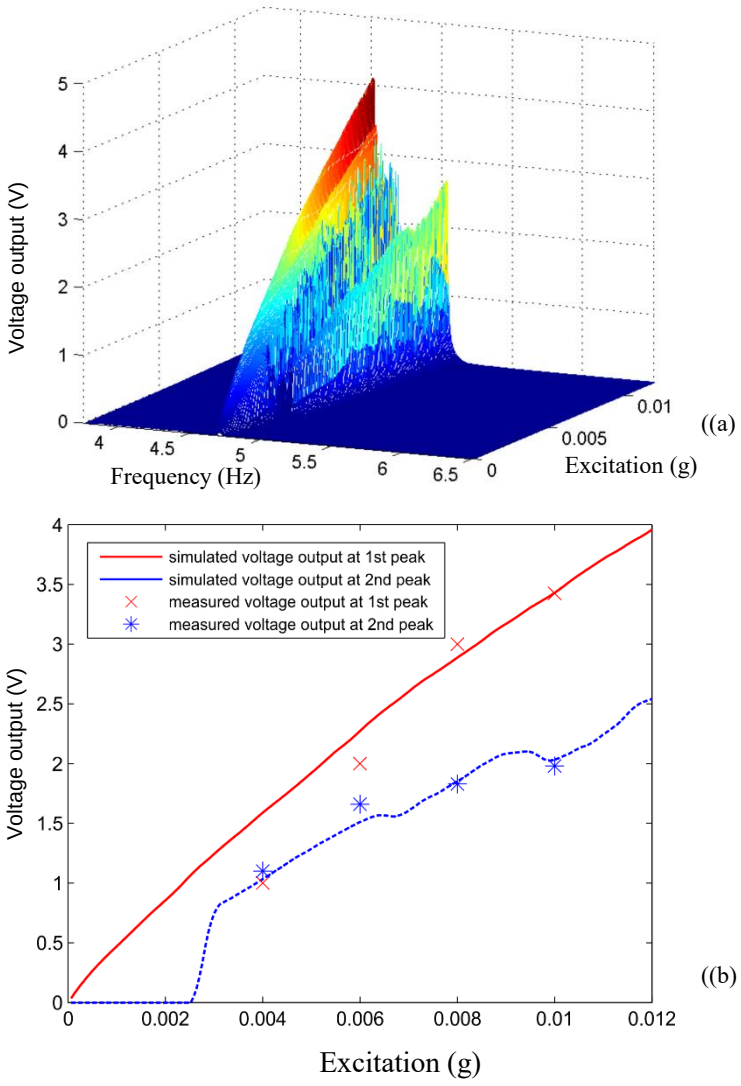

Figure 6-10. Voltage output. a) 3-dimensional plot of voltage output under *x*-direction excitation; b) Simulated and measured voltage output at the peaks against excitation accelerations.

6.4.4 Response characteristics under the z-direction excitation

The frequency responses under the *z*-direction excitation are examined in the vicinity of ω_2. In this case, the direction of the excitation is aligned with the sensitive direction of the energy harvester, i.e., the beam bending motion direction. The beam vibration is directly induced by the *z*-direction excitation for power generation. Figure 6-11a and Figure 6-12 show the forward frequency sweep responses of the open circuit voltage output under simulation and experiment, respectively.

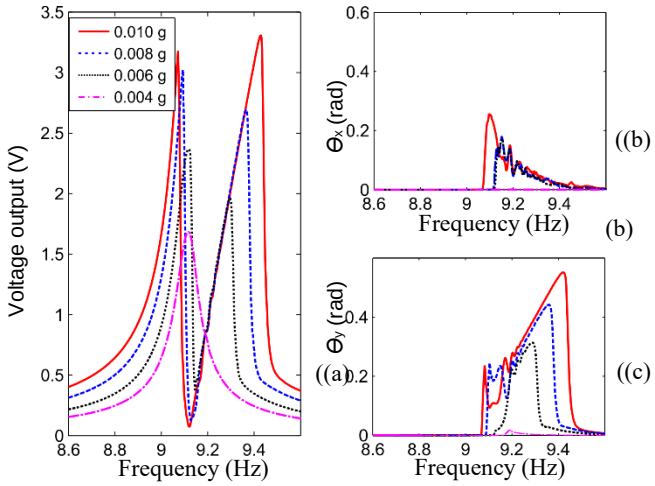

Figure 6-11. Simulated frequency responses under *z*-direction excitation. a) Voltage output versus excitation frequency; b) *xz*-plane pendulum motion; c) *yz*-plane pendulum motion.

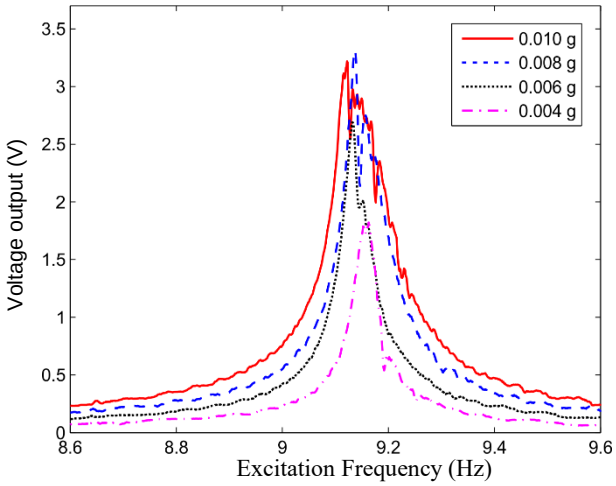

Figure 6-12. Measured frequency responses under *z*-direction excitation.

It can be observed that under low amplitude excitation, i.e., 0.004 g, the response exhibits a single peak. It is worth noticing that, under excitation of 0.004 g, the system dynamics contains only the beam

bending motion. Therefore, the responses yield that of a linear, second order system as indicated by Equation (6-35). In such a situation, the harvester performs the same as a traditional piezoelectric cantilever. On the other hand, multiple peaks can be observed due to the nonlinear coupling when the excitation accelerations increase. The peaks are induced since that the beam bending motion bifurcates into combinations of beam vibration and pendulum motions. For example, as shown in Figure 6-13, the peak around 9 Hz corresponds to the *xz*-plane pendulum mode while the one around 9.5 Hz is associated with *yz*-plane pendulum mode with hardening effect. Nevertheless, efficient power output can be obtained at these peaks. For instance, the output voltages at the peaks are 3.17 V and 3.3 V under excitation of 0.010 g, respectively. Moreover, cliff can be observed near 9.15 Hz. It is induced by bifurcation, where the pendulum mode shifts from θ_x to θ_y.

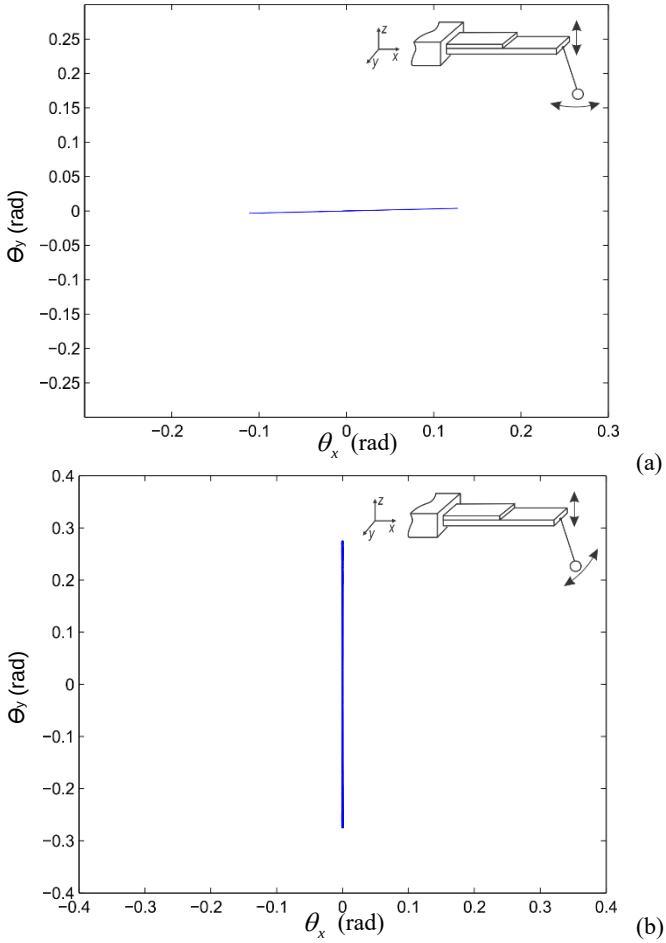

Figure 6-13. Pendulum motion projection to *xy*-plane under *z*-direction excitation (simulation). a) Pendulum motion around 9 Hz; b) Pendulum motion around 9.5 Hz.

Experimental results under z-direction excitation are shown in Figure 6-12. The response under excitation of 0.004 g resembles that of a second-order system. This phenomenon agrees well with that in the simulation. The voltage output exhibits multiple peaks when the excitation level increases. For example, the two corresponding peaks are 3.14 V and 2.35 V under excitation of 0.010 g. There are minor differences between the simulated responses and the measured ones due to non-perfect prototyping. Specifically, the pendulum is hinged onto the beam in the theoretical model while in experiment it is glued onto the beam. Therefore, the bifurcations are slightly different in experiments, and the second peak under z-direction excitation can be observed but not as clear as that in the simulation.

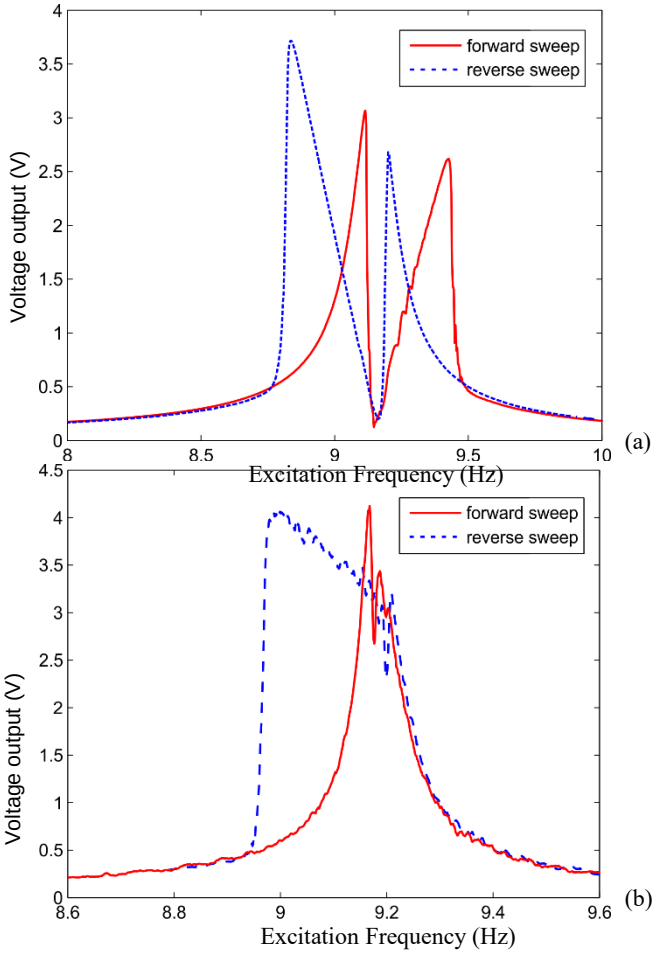

Figure 6-14. Frequency responses under z-direction excitation. a) Simulation; b) Measured response.

Figure 6-14 shows the forward and reverse frequency sweep responses under the *z*-direction excitation. Here the excitation level of 0.008 g is selected to ensure the presence of the key nonlinear phenomena, including the multi-peaks and saturation phenomenon. It can be observed that the peak with hardening effect turns into a peak with softening effect in the reverse frequency sweep. Besides, the peak with softening effect in the reverse frequency sweep has a higher voltage output than that in the forward frequency sweep. The peak with softening effect corresponds to the *yz*-plane pendulum motion. The experimental result exhibiting a softening behavior can be clearly observed in the reverse sweep under *z*-direction excitation, which agrees with that of the simulation.

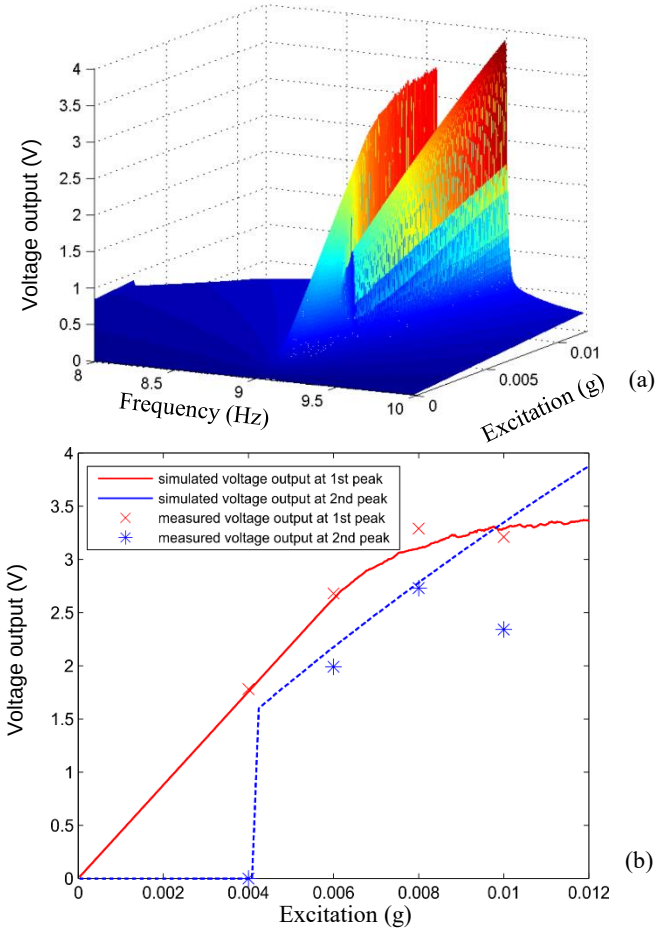

Figure 6-15. Voltage output. a) 3D plot of voltage output under *z*-direction excitation; b) Simulated and measured voltage output at the peaks against excitation accelerations.

Figure 6-15 plots the voltage output versus frequency and excitation level under the *z*-direction excitation. Figure 6-15a shows the simulation result of 3-dimensional plot of the voltage output under forward frequency sweep. Figure 6-15b shows the comparison of the simulated and measured voltage output at the peaks. Unlike the responses under horizontal excitations, saturation dynamics can be observed around 9 Hz when the *z*-direction excitation increases above a threshold value at around 0.008 g. As can be seen, the voltage output around 9 Hz has the same value when the system is saturated. In such a situation, the vibratory energy of the beam is spilled over to pendulum motion. In general, the threshold value for saturation dynamics is determined by the system configuration and parameters, e.g., found to be proportional to the stiffness of the auxiliary beam in an L-shaped cantilever system with 1:2 internal resonance (Haddow and Barr, 1984). Moreover, as another unique feature of this 3-dimensional system, a peak of voltage output due to bifurcation is induced around at 9.5 Hz when the excitation increases beyond 0.0042 g. It is worth noticing that the peak is associated with the yz-plane pendulum motion and does not have a saturation phenomenon. The voltage output at this peak increases as the excitation level increases.

6.4.5 Performance Comparison

In order to validate the performance improvement over a traditional harvester, a piezoelectric cantilever with the same parameters but a fixed proof-mass was fabricated for comparison. To ensure the presences of multiple peaks and saturation phenomena, excitations with amplitude of 0.008 g were applied in *x*-, *y*- and *z*-directions, respectively. The open circuit voltage outputs versus excitation frequency are plot in Figure 6-16. As can be observed, while the traditional harvester performs optimally under *z*-direction excitation, the cantilever-pendulum harvester yields efficient voltage output under excitations in all the three directions. The voltage output of the cantilever-pendulum under horizontal excitation is lower than that under *z*-direction excitation. Under this specific acceleration level, the maximum voltage output of the proposed design is not as high as that of the traditional one due to the

saturation phenomena. However, it is worth emphasizing that the proposed energy harvester features the unique advantage of harvesting energy from the *x*- and *y*-direction excitations essentially as efficient as from the *z*-direction.

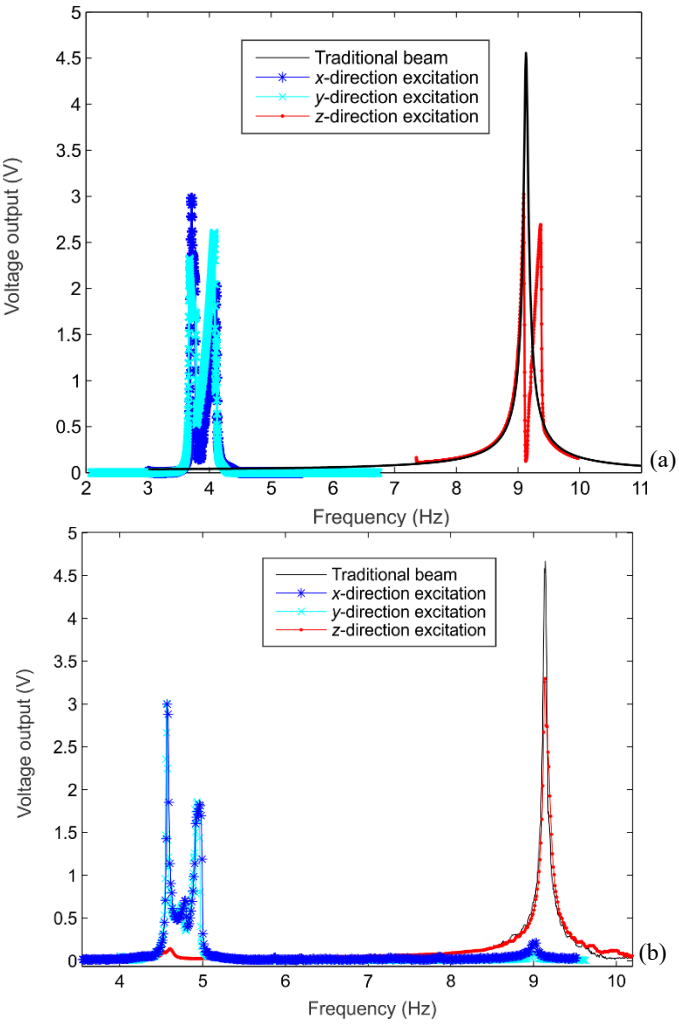

Figure 6-16. Voltage output comparison. a) Simulated responses; b) Measured response.

6.5 Concluding Remarks

In this research, a piezoelectric cantilever-pendulum system for multi-directional energy harvesting is modeled and analyzed. Multiple scale method, numerical simulation and experiments are carried to analyze the system. It is shown analytically and experimentally that, with proper parametric combination, 1:2 internal resonance is induced with the capability of multi-directional energy harvesting. When the

excitation is along the *z*-direction, it causes beam bending motion directly. When the excitation is in the *xy*-plane, the resulting pendulum motion can induce beam vibration resonance as well. Simulations and experiments confirm that the proposed design can harvest energy from the *x*- and *y*-direction excitations essentially as efficient as that from the *z*-direction. It's also illustrated numerically and experimentally that, bifurcation can be induced under various excitation frequencies and excitation amplitudes. Nonlinear modes are associating with these bifurcations. Further analysis and design optimization will be performed in future to examine the influences of system parameters and pendulum configurations.

Chapter 7 Conclusion and Future Work

Due to the two-way electro-mechanical coupling, piezoelectric transducers are widely utilized in actuator, sensor and energy harvester. Periodic and single piezoelectric structures have shown promising characteristics in aspect of wave attenuation and energy harvesting. In this dissertation research, theoretical modeling and applications of piezoelectric metamaterials/structures are developed and performed for wave guiding and energy harvesting. Five research tasks are presented and the preliminary analyses have shown promising results.

The first contribution is to develop the mathematical model of the piezoelectric metamaterial. In section 2, we study piezoelectric metamaterial based on piezoelectric transducers and inductive loads. A lumped-parameter, semi-analytical model of piezoelectric metamaterial is formulated based on continuum mechanics characterization. The equivalent unit-cell mass, stiffness, and electro-mechanical coupling parameter are derived and identified as wavenumber-dependent. Dispersion curves corresponding to piezoelectric circuitry with bimorph transducers under parallel-connection and serial-connection are obtained. The role of the system-level electro-mechanical coupling is identified and analyzed in detail. While the frequency range of the bandgap is determined by the LC circuit resonant frequency, the bandwidth of the bandgap is primarily determined by the electro-mechanical coupling. The parametric analyses are validated by finite element simulations. The adaptiveness of this piezoelectric metamaterial, which can be realized through online tuning of the inductance, is also discussed. The formulation and results obtained can be used to guide the circuitry synthesis and design optimization of the piezoelectric metamaterial.

The second contribution is to apply the piezoelectric metamaterial into wave guiding. In section 3, we firstly find that the proposed metamaterial-based prism offers the capability of steering the acoustic wave due to the local resonance from the LC shunt circuit. We analyze and demonstrate the tunable acoustic beam steering by choosing the at a single frequency point of 19.46 kHz. The angle of the wave can be tuned between 30 to 60 degrees by adjusting the inductance. The resonant frequency of the shunt

circuit can be modified by changing the inductance. Moreover, the full integration of the adaptive piezoelectric metamaterial, tunable inductors, computing resources, and power systems can form a hybrid metamaterial system where acoustic wave guiding can be remotely controlled. The concept proposed here can be applied to the adaptive GRIN lens for a variety of applications. Secondly, we find that the proposed metamaterial-based GRIN lens offers the capability of focusing the acoustic wave due to the local resonance from the LC shunt circuit. We analyze and demonstrate the acoustic beam focusing by choosing the at a single frequency point of 19.6 kHz. The incident acoustic wave can be clearly focused at a point in the vicinity of the GRIN lens. The resonant frequency of the shunt circuit can be modified by changing the inductance. Moreover, the full integration of the adaptive piezoelectric metamaterial, tunable inductors, computing resources, and power systems can form a hybrid metamaterial system where acoustic wave guiding can be remotely controlled.

The third contribution apply the piezoelectric metamaterial into the application of vibration mode tailoring. In section 4, we present a method for creation and adjustment of meta vibration mode in finite acoustic phononic crystal. It's proposed that distinct vibration modes can be created by combing the resonance and bandgap characteristics of finite photonic crystal. This concept is applied to a finite piezoelectric metamaterial beam. In the piezoelectric unitcell, inductance load is connected to the piezoelectric transducer individually. Euler beam theory and FEM simulations are carried out to illustrate the metamodes. Specifically, in the unusual vibration mode, resonance vibration is induced while the region with excitation applied has minimum displacement. That is, the vibration modes have the capability of "hit the enemy through another man in between". The unusual vibration modes can be applied to actuators or sensors where only the far end vibration is required. Moreover, this concept can be extended for mass-in-mass or Bragg scattering metamaterials. The present work not only opens the way to the creation of unusual vibration modes, but also to the creation and optimization of actuators or sensors without geometrical tailoring.

The four contribution is the application of a single piezoelectric structure in the field of energy

harvesting. In section 5, a scheme to improve the energy conversion capability of vibration-based piezoelectric energy harvester is developed. It is shown theoretically and experimentally that properly configured and positioned magnet elements can induce a linear magnetic field that yields negative stiffness. This scheme can effectively compensate the mechanical stiffness of the harvester and increase the electro-mechanical coupling at the device-level. Theoretical modeling, FEM simulation and experimental analysis are carried out to analyze the system. It's validated theoretically and experimentally that linear negative stiffness can be created to compensate the stiffness of the piezoelectric cantilever system. In this regard, the mechanical energy stored in the cantilever as well as the piezoelectric transducer can be reduced. This can improve the energy harvesting efficiency at both resonance and off-resonance situations. Experimental studies on a prototype show that electro-mechanical coupling factor can be increased by 65% with 44.1% stiffness compensated. Both the open-circuit voltage and the power output are enhanced.

The fifth contribution is the application of a single piezoelectric structure in the field of multiple directional energy harvesting. In section 7, a piezoelectric cantilever-pendulum system for multi-directional energy harvesting is modeled and analyzed. Multiple scale method, numerical simulation and experiments are carried to analyze the system. It is shown analytically and experimentally that, with proper parametric combination, 1:2 internal resonance is induced with the capability of multi-directional energy harvesting. When the excitation is along the *z*-direction, it causes beam bending motion directly. When the excitation is in the *xy*-plane, the resulting pendulum motion can induce beam vibration resonance as well. Simulations and experiments confirm that the proposed design can harvest energy from the *x*- and *y*-direction excitations essentially as efficient as that from the *z*-direction. It's also illustrated numerically and experimentally that, bifurcation can be induced under various excitation frequencies and excitation amplitudes. Nonlinear modes are associating with these bifurcations.

However, there are still remaining works to accomplish systematically. In an earlier study, a tunable inductor is integrated into the piezoelectric metamaterial system for wave steering, focusing and vibration

modes creation. It has been demonstrated that, with proper adjustment of the inductance load. The acoustic wave in the plate or beam can be continuous steered or focused. Moreover, unique vibration modes can be created with notable capability. However, the performance of the piezoelectric metamaterials is fundamentally hinged upon the electro-mechanical coupling coefficient of the unit-cell, as discussed in section 2. In other words, the piezoelectric metamaterial would have little wave guiding capability when the electro-mechanical coupling coefficient is very low. This is because very little mechanical energy is transferred into electrical energy, which is interfacing with the shunt circuit with local resonance, when the coupling coefficient of the unitcell is very small. The strategies of improving the coupling coefficient should be investigated.

In the applications of single piezoelectric structures, cantilever pendulum is proposed for multiple directional energy harvesting. On the other hand, the nonlinearity adopted here is greatly hinged upon the gravity. In portable devices, the direction of gravity might be changing over times, i.e., the direction of gravity may not be in *z*-direction of the device. In this regard, the applications of such a system might be limited when it is integrated into portable device. Further analysis and design optimization will be performed in future to examine the influences of system parameters and pendulum configurations.

Bibliography

Achaoui, Y., Khelif, A., Benchabane, S., Robert, L., and Laude, V., 2011, "Experimental observation of locally-resonant and Bragg band gaps for surface guided waves in a phononic crystal of pillars," Physics Review B, 83(10), pp. 104201.

Airoldi, L., and Ruzzene, M., 2011, "Internally resonating lattices for bandgap generation and low-frequency vibration control," Journal of Intelligent Material Systems and Structures, 22(14), pp. 1567-1579.

Alberto, B., and Paolo, E., 2007, "Optimum placement of piezoelectric ceramic modules for vibration suppression of highly constrained structures", Smart Materials and Structures, V16, 1662–1671.

Anton, S. R., and Sodano, H. A., 2007, "A review of power harvesting using piezoelectric materials (2003–2006)," Smart Materials and Structures, V16, R1.

Ando, B., Baglio, S., Maiorca, F. and Trigona, C., 2013, "Analysis of two dimensional, wide-band, bistable vibration energy harvester", Sensors and Actuators A, V202, 176-182.

Baker, J., Roundy, S., and Wright, P., 2005, "Alternatives geometries for increasing power density in vibration energy scavenging for wireless sensor networks," Proceedings of the 3rd International Energy Conversion Engineering Conference (San Francisco, CA, August 15–18, August), 959–70.

Baravelli, E., and Ruzzene, M., 2013, "Internally resonating lattices for bandgap generation and low-frequency vibration control," Journal of Sound and Vibration, 332(25), pp. 6562-6579.

Baravelli, E., Senesi, M. and Ruzzene, M., 2013, "Fabrication and Characterization of a Wavenumber-Spiral Frequency-Steerable Acoustic Transducer for Source Localization in Plate Structures," IEEE Transactions on Instrumentation and Measurement, V62, 2197 - 2204.

Bartsch, U., Gaspar, J. and Paul, O., 2009, "A 2D electret-based resonant micro energy harvester," IEEE 22nd International Conference on Micro Electro Mechanical Systems, 1043-1046.

Banerjee, B., Bajaj, A. K. and Davies, P., 1995, "Resonant dynamics of an autoparametric system: A study using higher-order averaging," International Journal of Non-Linear Mechanics, V31, 21-39.

Bigoni, D., Guenneau, S., Movchan, A. B., and Brun, M., 2013, "Elastic metamaterials with inertial locally resonant structures: Application to lensing and localization," Physical Review B, 87(17), pp. 174303.

Casadei, F., Beck, B., Cunefare, K., and Ruzzene, M., 2012, "Vibration control of plates through hybrid configurations of periodic piezoelectric shunts," Journal of Intelligent Material Systems and Structures, V23, 1169-1177.

Casadei, F., Ruzzene, M., Dozio, L., and Gunefare, K. A., 2010, “Broadband vibration control through periodic arrays of resonant shunts: experimental investigation on plates,” Smart Materials and Structures, 19(1), pp. 015002.

Challa, V. R., Prasad, M. G., Shi, Y., and Fisher, F. T., 2008, “A vibration energy harvesting device with bi-directional resonance frequency tunability,” Smart Materials and Structures, V17, 015035.

Che, K., Yuan, C., Wu, J., Qi, H., and Meaud, J., 2017, “Three-dimensional-printed multistable mechanical metamaterials with a deterministic deformation sequence,” ASME Journal of Applied Mechanics, 84(1), pp. 011004.

Chen, Y., Huang, G., and Sun, C. T., 2014, “Band gap control in an active elastic metamaterial with negative capacitance piezoelectric shunting,” ASME Journal of Vibration and Acoustic, 136(6), pp. 061008.

Chen, S., Wen, J., Wang, G., Yu, D., and Wen, X., 2012, “Improved modeling of rods with periodic arrays of shunted piezoelectric patches,” Journal of Intelligent Material Systems and Structures, V23, 1613-1621.

Chen, L. and Jiang, W., 2015, “Internal resonance energy harvesting,” Journal of Applied Mechanics, V28, 031004.

Chen, Q., and Wang, Q., 2005, “The effective electromechanical coupling coefficient of piezoelectric thin-film resonators”, Applied Physics Letter, V86, 022904.

Chen, R., Ren, L., Xia, H., Yuan, X. and Liu, X., 2015, “Energy harvesting performance of a dandelion-like multi-directional piezoelectric vibration energy harvester,” Sensors and Actuators A, V230, 1-8.

Climente, A., Torrent, D., and Sanchez-Dehesa, J., 2010, “Sound focusing by gradient index sonic lenses,” Applied Physics Letters, V97, 104103.

Collet, M., Ouisse, M., and Ichchou, M. N., 2012, “Structural energy flow optimization through adaptive shunted piezoelectric metacomposite,” Journal of Intelligent Material Systems and Structures, 23(15), pp. 1661-1677.

Cottone, F., Vocca, H., and Gammaitoni, L., 2009, “Nonlinear energy harvesting,” Physical Review Letters, V102, 080601.

Deymier, A. P., 2013, “Acoustic metamaterials and phononic crystals,” Springer US.

Di Lullo, G. A., Sweeney, S. M., Körkkö, J., Ala-Kokko, L., and San Antonio, J. D., 2002, Mapping the ligand-binding sites and disease-associated mutations on the most abundant protein in the human, type I collagen. Journal of Biological Chemistry, 277(6), 4223-4231.

Erturk, A., Renno, J. M. and Inman, D. J., 2009, “Modeling of piezoelectric energy harvesting from an L-shaped beam-mass structure with an application to UAVs,” Journal of Intelligent Material Systems

and Structures, V20, 529-544. (a)

Erturk, A., Hoffmann, J. and Inman, D. J., 2009, “A piezomagnetoelastic structure for broadband vibration energy harvesting,” Applied Physics Letters, V94, 254102. (b)

Fang, N., Lee, H., Sun, C., and Zhang, X., 2005, “Sub-diffraction-limited optical imaging with a silver superlens,” Science, 308(5721), pp. 534-537.

Ferrari, M., Ferrari, V., Guizzetti, M. and Marioli, D., 2010, “A single-magnet nonlinear piezoelectric converter for enhanced energy harvesting from random vibrations,” Proc. Eurosensors XXIV.

Guyomar, D., Badel, A., Lefeuvre, E., and Richard, C., Daniel, G., Adrien, B., Lefeuvre, E, and Richard, C., 2005, “Toward energy harvesting using active materials and conversion improvement by nonlinear processing,” IEEE Transactions on Ultrasonics, Ferroelectrics, and Frequency Control, V52, 584 - 595.

Haddow, A. G. and Barr, A. D. S., 1984, “Theoretical and experimental study of modal interaction in a two-degree-of-freedom structure,” Journal of Sound and Vibration, V97, 451-473.

Hatwal, H., Mallik, A. K. and Ghosh, A., 1986, “Forced nonlinear oscillations of an autoparametric system- part 1: periodic Responses,” Journal of Applied Mechanics, V50, 657-662.

Henck, N. S., and Paradiso, J. A., 2001, “Energy scavenging with shoe-mounted piezoelectrics,” IEEE Micro Magazine, V21, 30–42.

Hu, G., Tang, L., Banerjee, A., and Das, R., 2016, “Meta-structure with piezoelectric element for simultaneous vibration suppression and energy harvesting,” ASME Journal of Vibration and Acoustics, 139(1), pp. 011012.

Huang, G., and Sun, C. T., 2010, “Band gaps in a multiresonator acoustic metamaterial,” ASME Journal of Vibration and Acoustic, 132(3), pp. 031003.

Huang, H. H., Lin, C. K., and Tan, K. T., 2016, “Attenuation of transverse waves by using a metamaterial beam with lateral local resonators,” Smart Materials and Structures, 25(8), pp. 085027.

IEEE Standard on Piezoelectricity, ANSI/IEEE Std, 176-1987.

Ji, J., Kong, F., He, Guan, Q., and Feng, Z., 2010, “Piezoelectric wind-energy-harvesting device with reed and resonant cavity,” Japanese Journal of Applied Physics, V49, 050204.

Jung, S. and Yun, K., 2010, “Energy-harvesting device with mechanical frequency-up conversion mechanism for increased power efficiency and wideband operation,” Applied Physics Letters, V96, 111906.

Kenji, U., and Takaaki, I., 2010, “Energy Flow Analysis in Piezoelectric Energy Harvesting Systems,” Ferroelectrics, V400, 305-320.

Khaligh, A., Zeng, P., and Zheng, C., 2010, “Kinetic energy harvesting using piezoelectric and electromagnetic technologies—state of the art,” IEEE Transactions on Industrial Electronics, V57, 850–

860.

Kim, D., Hewa-Kasakarage, N. N., Yoon, S., and Hall, N. A., 2012, “On the minimum coupling required for maximum theoretical power capture from vibration energy harvesters,” Applied Physics Letters, V101, 103904.

Lallart, M., Yan, L., Richard, C., and Guyomar, D., 2015, “Damping of periodic bending structures featuring nonlinearly interfaced piezoelectric elements,” Journal of Vibration and Control, 22(18), pp. 3930-3941.

Landy, N. I., Sajuyigbe, S., Mock, J. J., Smith, D. R., and Padilla, W. J., 2008, “Perfect metamaterial absorber,” Physical Review Letters, 100(20), pp. 207402.

Lefeuvre, E., Badel, A., Richard, C., Petit, L., and Guyomar, D., 2006, “A comparison between several vibration-powered piezoelectric generators for standalone systems,” Sensors and Actuators A: Physical, V126, 405-416.

Lee, W. K. and Hsu, C. S., 1994, “A global analysis of a harmonically excited spring-pendulum system with internal resonance,” Journal of Sound and Vibration. V171, 335-359.

Lesieutre, G. A., and Davis, C. L., 1997, “Can a Coupling Coefficient of a Piezoelectric Device be Higher Than Those of Its Active Material?”, Journal of Intelligent Material Systems and Structures, V8, 859-867.

Leland, E. S., and Wright, P. K., 2006, “Resonance tuning of piezoelectric vibration energy scavenging generators using compressive axial preload,” Smart Materials and Structures, V15, 051413.

Liang, J. R., and Liao, W. H., 2011, “Energy flow in piezoelectric energy harvesting systems,” Smart Materials and Structures, V20, 015005.

Li, J., and Chan, C. T., 2004, “Double-negative acoustic metamaterial,” Physical Review E, 70(5), pp. 055602.

Liu, L., and Hussein, M. I., 2012, “Wave motion in periodic flexural beams and characterization of the transition between Bragg scattering and local resonance,” ASME Journal of Applied Mechanics, 79(1), pp. 011003.

Liu, Z., Zhang, X., Mao, Y., Zhu, Y. Y., Yang, Z., Chan, C. T., and Sheng, P., 2000, “Locally resonant sonic materials,” Science, 289(5485), pp. 1734-1736.

Mei, J., Ma, G. C., Yang, M., Yang, Z., Wen, W.J., and Sheng, P., 2012, “Dark acoustic metamaterials as super absorbers for low-frequency sound,” Nature Communication, 3, 756.

Mitcheson, P. D., Yeatman, E. M., Kondala, R. G., Holmes, A. S., and Green, T. C., 2008, “Energy harvesting from human and machine motion for wireless electronic devices,” Proceedings of the IEEE, V96(9), 1457 - 1486.

Moon, F. C., 1978, “Problems in magneto-solid mechanics”, Mechanics Today, V4, Edited by

Nemat-Nasser, S. (New York: Pergamon).

Monsoriu, J. A., Depine, R. A., MartÝnez-Ricci, M. L., and Silvestre, E., 2006, "Interaction between non-Bragg band gaps in 1D metamaterial photonic crystals," Optics Express, 14(26), pp. 12958-12967.

Narisetti, R. K., Leamy, M. J., and Ruzzene, M, 2010, "A perturbation approach for predicting wave propagation in one-dimensional nonlinear periodic structures," ASME Journal of Vibration and Acoustics, 132(3), pp. 031001.

Nayfeh, A. H. and Zavodney, L. D., 1988, "Experimental observation of amplitude- and phase-modulated responses of two internally coupled oscillators to a harmonic excitation," Transactions of the ASME, V55, 706-710.

Nayfeh, A. H., balachandran, B., Colbert, M. A. and Nayfeh, M. A., 1989, "An experimental investigation of complicated responses of a two-degree-of-freedom structure," Transactions of the ASME, V56, 960-967.

Neiss, S., Goldschmidtboeing, F., Kroener, M. and Woias, P., 2014, "Analytical model for nonlinear piezoelectric energy harvesting device," Smart Materials and Structures, V23, 105031.

Niri, E. D., and Salamone, S., 2012, "A passively tunable mechanism for a dual bimorph energy harvester with variable tip stiffness and axial load," Smart Materials and Structures, V21, 125025.

Pai, P. F., Peng, H., and Jiang, S., 2014, "Acoustic metamaterial beams based on multi-frequency vibration absorbers," International Journal of Mechanical Sciences, 79, pp. 195-205.

Paradiso, J. A., and Starner, T., 2005, "Energy scavenging for mobile and wireless electronics," IEEE Pervasive Computing Magazine, V4, 18–27.

Priya, S., 2007, "Advances in energy harvesting using low profile piezoelectric transducers," Journal of Electroceramics, V19, 165–182.

Pendry, J. B., and Li, J., 2008, "An acoustic metafluid: realizing a broadband acoustic cloak," New Journal of Physics, 10, pp. 115032.

Rakbamrung, P., Lallart, M., Guyomar, D., Muensit, N., Thanachayanont, C., Lucat, C., Guiffard, B., Petit, L., and Sukwisut, P., Prissana, R., Mickaël, L., Daniel, G., Nantakan, M., Chanchana, T., Claude, L., Benoît, G., Lionel, P., and Pisan, S., 2010, "Performance comparison of PZT and PMN–PT piezoceramics for vibration energy harvesting using standard or nonlinear approach," Sensors and Actuators A: Physical, V163, 493–500.

Roundy, S., 2005, "On the effectiveness of vibration-based energy harvesting," Journal of Intelligent Material Systems and Structures, V16, 809-823.

Roundy, S., Leland, E. S., Baker, J., Carleton, E., Reilly, E. K., Lai, E., Otis, B. P., Rabaey, J. M. M., Wright, P. K., and Sundararajan, V., 2005, "Improving power output for vibration-based energy scavengers," IEEE Pervasive Computing Magazine, IEEE, V4, 28–36.

Renno, J. M., Daqaq, M. F., and Inman, D. J., 2009, “On the optimal energy harvesting from a vibration source,” Journal of Sound and Vibration, V320, 386-405.

Stanton, S. C., McGehee, C. C. and Mann, B. P., 2009, “Reversible hysteresis for broadband magnetopiezoelastic energy harvesting,” Applied Physics Letters, V95, 174103.

Shahruz, S. M., 2006. “Design of mechanical band-pass filters for energy scavenging,” Journal of Sound and Vibration, V292, 987-998.

Safari, A., and Akdogan, E. K., 2008, Piezoelectric and acoustic materials for transducer applications. Springer Science & Business Media.

Shenck, N. S., and Paradiso, J. A., 2001, “Energy scavenging with shoe-mounted piezoelectrics”, IEEE Micro., V21, 30–42.

Sheheitli, H. and Rand, R. H., 2012, “Dynamics of a mass–spring–pendulum system with vastly different frequencies,” Nonlinear Dynamics, V70, 25-41.

Su, W. and Zu, J., 2013, “An innovative tri-directional broadband piezoelectric energy harvester,” Applied Physics Letters, V103, 203901.

Soliman, M. S. M., Abdel-Rahman, E., EI-Saadany E. and Mansour, R. R., 2008, “A wideband vibration-based energy harvester,” Journal of Micromechanics and Microengineering, V18, 115021.

Shu, Y. C., and Lien, I. C., 2006, “Efficiency of energy conversion for a piezoelectric power harvesting system,” Journal of Micromechanics and Micro-engineering, V16, 2429–2438.

Senesi, M., Xu, B., and Ruzzene, M., 2010, “Experimental characterization of periodic frequency-steerable arrays for structural health monitoring,” Smart Materials and Structures, V19, 055026.

Tan, K. T., Huang, H. H., and Sun, C. T., 2014, “Blast-wave impact mitigation using negative effective mass density concept of elastic metamaterials,” International Journal of Impact Engineering, 64, pp. 20-29.

Tadesse, Y., Zhang, S. and Priya, S., 2009, ‘‘Multimodal energy harvesting system: piezoelectric and electromagnetic,’’ Journal of Intelligent Material Systems and Structures, V20, 625-632.

Tang, J., and Wang, K. W., 2001, “Active-passive hybrid piezoelectric networks for vibration control: comparisons and improvement,” Smart Materials and Structures, 10(4), pp. 794-806.

Tang, J., and Wang, K. W., 2003, “Vibration delocalization of nearly periodic structures using coupled piezoelectric networks,” ASME Journal of Vibration and Acoustics, 125(1), pp. 95-108.

Thorp, O., Ruzzene, M., and Baz, A., 2005, “Attenuation of wave propagation in fluid-loaded shells with periodic shunted piezoelectric rings”, Smart Materials and Structures, 14(4), pp. 594-604.

Thorp, O., Ruzzene, M., and Baz, A., 2001, “Attenuation and localization of wave propagation in rods with periodic shunted piezoelectric patches,” Smart Materials and Structures, V10, 5.

Vedaraj, I. R., Parijaat, S., and Rao, B. V. A., 2012, Material analysis for artificial muscle and touch sensing of cooperative biomimetic manipulators. The International Journal of Advanced Manufacturing Technology, 60(5-8), 683-692.

Vinod, R. C., Prasad, M. G., Yong, S. and Frank, T. F., 2008, "A vibration energy harvesting device with bidirectional resonance frequency tenability," Smart Materials and Structures, V17, 015035.

Wang, K. W., and Tang, J., 2008, Adaptive Structural Systems with Piezoelectric Transducer Circuitry, Springer, New York, US.

Wang, G., Wen, X., Wen, J., and Liu, Y., 2006, "Quasi-one-dimensional periodic structure with locally resonant band gap," Journal of Applied Mechanics, V73, 167-170.

Wang, G., Chen, S., and Wen, J., 2010, "Low-frequency locally resonant band gaps induced by arrays of resonant shunts with Antoniou's circuit: experimental investigation on beams," Smart Materials and Structures, 20(1), pp. 015026.

Wang, G., and Chen, S., 2016, "Large low-frequency vibration attenuation induced by arrays of piezoelectric patches shunted with amplifier-resonator feedback circuit," Smart Materials and Structures, 25(1), pp. 015004.

Wang, F., Bajaj, A. K. and Kamiya, K., 2005, "Nonlinear normal modes and their bifurcations for an inertially coupled nonlinear conservative system," Nonlinear Dynamics, V42, 233-265.

Wu, W., Chen, X., and Shan, Y., 2014, "Analysis and experiment of a vibration isolator using a novel magnetic spring with negative stiffness," Journal of Sound and Vibration, V333, 2958-2970.

Xu, J., and Tang, J., 2015, "Linear stiffness compensation using magnetic effect to improve electro-mechanical coupling for piezoelectric energy harvesting," Sensors and Actuators A: Physical, 235(1), pp. 80-94.

Xu, J. and Tang, J., 2015, "Piezoelectric cantilever-pendulum for multi-directional energy harvesting with internal resonance," Proceeding of SPIE, 9431, 94310M.

Xu, J., Li, L., and Tang, J., 2016, "Parametric analysis of piezoelectric metamaterial with LC shunt circuit," Proceedings of the ASME 2016 Conference on Smart Materials, Adaptive Structure and Intelligent System.

Xu, J., Liu, Y., Shao, W., and Feng, Z., 2012, "Optimization of a right-angle piezoelectric cantilever using auxiliary beams with different stiffness levels for vibration energy harvesting," Smart Materials and Structures, V21, 065017.

Yang, J., Yue, X., Wen, Y., Li, P., Yu, Q. and Bai, X., 2013, "Design and analysis of a 2D broadband vibration energy harvester for wireless sensors," Sensors and Actuators A, V205, 47-52.

Yan, X., Zhu, R., Huang, G., and Yuan, F., 2013, "Focusing guided waves using surface bonded elastic metamaterials," Applied Physics Letters, V103, 121901.

Yoo, Y. J., Zheng, H. Y., Kim, Y. J., Rhee, J. Y., Kang, J. H., Kim, K. W,, Cheong, H., Kim, Y. H., and Lee, Y. P., 2014, "Flexible and elastic metamaterial absorber for low frequency, based on small-size unit cell," Applied Physics Letters, 105, pp. 041902.

Yang, J., Huang, M., Yang, C., Peng, J., and Chang, J., 2010, "An external acoustic cloak with N-sided regular polygonal cross section based on complementary medium," Computational Materials Science, 49(1), pp. 9-14.

Yang, Z., Mei, J., Yang, M., Chan, N. H., and Sheng, P., 2008, "Membrane-type acoustic metamaterial with negative dynamic mass," Physical Review Letters, 101(20), pp. 204301.

Zhao, J., Wang, X., and Tang, J., 2011, "Damping reduction in structures using piezoelectric circuitry with negative resistance," ASME Journal of Vibration and Acoustics, 133(4), pp. 041009.

Zhao, L., Conlon, S. C., and Semperlotti, F., 2014, "Broadband energy harvesting using acoustic black hole structural tailoring," Smart Materials and Structures, 23(6), pp. 065021

Zhu, R., Chen, Y., Barnhart, M., Hu, G., Sun, C. T., and Huang, G., 2016, "Experimental study of an adaptive elastic metamaterial controlled by electric circuits," Applied Physics Letters, 108, pp. 011905.

Zhu, H., and Semperlotti, F., 2014, "A passively tunable acoustic metamaterial lens for selective ultrasonic excitation," Journal of Applied Physics, V116, 094901.

Zhu, D., Roberts, S., Tudor, M. J., and Beeby, S. P., 2010, "Design and experimental characterization of a tunable vibration-based electromagnetic micro-generator," Sensor and Actuators A: Physical, V158, 284-293.

Zhou, W., Wu, Y., and Zuo, L., 2015, "Vibration and wave propagation attenuation for metamaterials by periodic piezoelectric arrays with high-order resonant circuit shunts," Smart Materials and Structures, 24(6), pp. 065021.

Zhou, S., Cao, J., Erturk, A. and Lin, J., 2013, "Enhanced broadband piezoelectric energy harvesting using rotatable magnets," Applied Physics Letters, V102, 173901.